



# LUND UNIVERSITY

## Neutron Irradiation Techniques

Scherzinger, Julius

2016

[Link to publication](#)

*Citation for published version (APA):*

Scherzinger, J. (2016). *Neutron Irradiation Techniques*. Lund University, Faculty of Science, Department of Physics.

*Total number of authors:*

1

### General rights

Unless other specific re-use rights are stated the following general rights apply:

Copyright and moral rights for the publications made accessible in the public portal are retained by the authors and/or other copyright owners and it is a condition of accessing publications that users recognise and abide by the legal requirements associated with these rights.

- Users may download and print one copy of any publication from the public portal for the purpose of private study or research.
- You may not further distribute the material or use it for any profit-making activity or commercial gain
- You may freely distribute the URL identifying the publication in the public portal

Read more about Creative commons licenses: <https://creativecommons.org/licenses/>

### Take down policy

If you believe that this document breaches copyright please contact us providing details, and we will remove access to the work immediately and investigate your claim.

LUND UNIVERSITY

PO Box 117  
221 00 Lund  
+46 46-222 00 00

# NEUTRON IRRADIATION TECHNIQUES

by JULIUS SCHERZINGER



**LUND**  
UNIVERSITY

THESIS FOR THE DEGREE OF DOCTOR OF PHILOSOPHY  
THESIS ADVISORS: DR. KEVIN FISSIUM AND  
DR. RICHARD HALL-WILTON  
FACULTY OPPONENT: DR. ROBERT PYWELL

TO BE PRESENTED, WITH THE PERMISSION OF THE FACULTY OF SCIENCE OF LUND UNIVERSITY, TO THE  
PUBLIC IN THE RYDBERG LECTURE HALL AT THE DEPARTMENT OF PHYSICS, SÖLVEGATAN 14, ON  
FRIDAY, THE 16TH OF DECEMBER 2016 AT 13:15.

Organization <b>LUND UNIVERSITY</b> DEPARTMENT OF PHYSICS Box 118 SE – 221 00 LUND SWEDEN		Document name <b>DOCTORAL DISSERTATION</b>	
Author(s) <b>JULIUS SCHERZINGER</b>		Date of disputation <b>2016-12-16</b>	
Sponsoring organization			
Title and subtitle <b>NEUTRON IRRADIATION TECHNIQUES</b>			
Abstract The $^3\text{He}$ “crisis” has become a fact in the last decade and large scale neutron detectors based on $^3\text{He}$ technologies have become unaffordable. This new $^3\text{He}$ reality has resulted in a major effort worldwide to develop replacement neutron-detector technologies. Many of these technologies are in their infancy and need to be thoroughly tested before becoming mainstream, while others are approaching commercialization and need to be certified. Still others which are commercially available today need to be tested before being installed in, for example, the instruments at the European Spallation Source ERIC. Detector technologies in all three stages of development need neutrons for controlled irradiations. Sources of neutrons for controlled irradiations include accelerators, nuclear reactors and radioactive sources. Neutrons produced in nuclear reactors and at accelerators have a very high cost of entry and a very high cost per neutron. In contrast, radioactive sources produce neutrons with a significantly lower cost of entry and lower cost per neutron. A drawback associated with radioactive sources is the associated isotropic mixed neutron/gamma-ray field. The Source Testing Facility has been established at the Division of Nuclear Physics at Lund University to provide a source-based neutron irradiation facility to local academic users and industry. This work presents the development of a cost-efficient test bed for the production of 2-6 MeV neutrons, an integral part of the Source Testing Facility. The test bed is based on actinide/ $^9\text{Be}$ sources and lowers the barrier for local groups for precision neutron testing of detector technologies and shielding studies. Well-understood nuclear physics coincidence and time-of-flight measurement techniques are applied to unfold the mixed neutron/gamma-ray field and unambiguously identify the energies of the neutrons on an event-by-event basis. The Source Testing Facility thus developed is then used in conjunction with Arktis Radiation Detectors of Zurich, Switzerland for benchmarking the response of next generation $^4\text{He}$ based neutron detectors against standard NE-213 liquid scintillator detectors. The response of these standard NE-213 liquid scintillator detectors is then carefully unfolded and various models of the response of the scintillator itself are tested. The outputs of different actinide/ $^9\text{Be}$ sources are then precisely compared in an effort to identify preferred actinides. And lastly, a complementary facility for the tagging of neutrons from the spontaneous-fission source $^{252}\text{Cf}$ is developed as a first step towards providing users the capability to measure the absolute, fast-neutron detection efficiency of their devices.			
Key words actinide/Be, fast-neutrons, NE-213 liquid scintillator, $^4\text{He}$ scintillators, pulse-shape discrimination, $^{252}\text{Cf}$ , absolute detection efficiency, neutron irradiation			
Classification system and/or index terms (if any)			
Supplementary bibliographical information		Language <b>English</b>	
ISSN and key title		ISBN 978-91-7623-924-7 (print) 978-91-7623-925-4 (pdf)	
Recipient's notes		Number of pages <b>157</b>	Price
		Security classification	

I, the undersigned, being the copyright owner of the abstract of the above-mentioned dissertation, hereby grant to all reference sources the permission to publish and disseminate the abstract of the above-mentioned dissertation.

Signature \_\_\_\_\_

Date 2016-12-16

# NEUTRON IRRADIATION TECHNIQUES

by JULIUS SCHERZINGER



**LUND**  
UNIVERSITY

**Cover illustration front:** The front cover shows the inner chamber of the Aquarium. The picture was kindly provided by Nicholai Mauritzson.

**Funding information:** The thesis work was financially supported by the European Spallation Source ERIC.

© JULIUS SCHERZINGER 2016

FACULTY OF SCIENCE  
DEPARTMENT OF PHYSICS  
Box 118  
SE – 221 00 LUND  
SWEDEN

ISBN: 978-91-7623-924-7 (print)

ISBN: 978-91-7623-925-4 (pdf)

Printed in Sweden by Media-Tryck, Lund University, Lund 2016



*Odi et amo. Quare id faciam fortasse requiris.*

*Nescio. Sed fieri sentio et excrucior.*

– Catullus 85 –



# List of Abbreviations

ADC	Analog-to-Digital Converter
Am/Be	Americium-Beryllium
CAD	Computer-Aided Design
CAMAC	Computer Automated Measurement And Control
CBD	CAMAC Branch Driver
CeBr <sub>3</sub>	Cerium Bromide
DAQ	Data Acquisition
ESS	European Spallation Source
FOM	Figure-of-Merit
FWHM	Full-Width at Half-Maximum
GEANT 4	GEometry ANd Tracking 4
L	Light Yield
LG	Long Gate
NDT	Neutron Diagnostic Tool
NIM	Nuclear Instrumentation Module
PMMA	Poly-Methyl-Methacrylate
PMT	Photomultiplier Tube
PH	Pulse Height
PHD	Pulse-Height Discrimination
PS	Pulse Shape
PSD	Pulse-Shape Discrimination
PTFE	Polytetrafluoroethylene
Pu/Be	Plutonium-Beryllium
QDC	Charge-to-Digital Converter
STF	Source Testing Facility
SG	Short Gate
TDC	Time-to-Digital Converter
TOF	Time-of-Flight
VME	Versa Module Europa
YAP	Yrtium Aluminum Pervokite



# List of Publications

## I Tagging fast neutrons from an $^{241}\text{Am}/^9\text{Be}$ source

J. Scherzinger, J.R.M. Annand, G. Davatz, K.G. Fissum, U. Gendotti, R. Hall-Wilton, E. Håkansson, R. Jebali, K. Kanaki, M. Lundin, B. Nilsson, A. Rosborg and H. Svensson  
Applied Radiations and Isotopes 98 (2015) 74 – 79.  
<http://dx.doi.org/10.1016/j.apradiso.2015.01.003>.

## II A first comparison of the responses of a $^4\text{He}$ -based fast-neutron detector and a NE-213 liquid-scintillator reference detector

R. Jebali, J. Scherzinger, J.R.M. Annand, R. Chandra, G. Davatz, K.G. Fissum, H. Friedrich, U. Gendotti, R. Hall-Wilton, E. Håkansson, K. Kanaki, M. Lundin, D. Murer, B. Nilsson, A. Rosborg, and H. Svensson  
Nuclear Instruments and Methods in Physics Research Section A 794 (2015) 102 – 108.  
<http://dx.doi.org/10.1016/j.nima.2015.04.058>.

## III The light-yield response of a NE-213 liquid-scintillator detector measured using 2 – 6 MeV tagged neutrons

J. Scherzinger, R. Al Jebali, J.R.M. Annand, K.G. Fissum, R. Hall-Wilton, K. Kanaki, M. Lundin, B. Nilsson, H. Perrey, A. Rosborg, H. Svensson  
Nuclear Instruments and Methods in Physics Research Section A 840 (2016) 121 – 127.  
<http://dx.doi.org/10.1016/j.nima.2016.10.011>.

IV **A comparison of untagged gamma-ray and tagged-neutron yields from  $^{241}\text{AmBe}$  and  $^{238}\text{PuBe}$  sources**

**J. Scherzinger**, R. Al Jebali, J.R.M. Annand, K.G. Fissum, R. Hall-Wilton, S. Koufigar, N. Mauritzson, F. Messi, H. Perrey, E. Rofors  
Manuscript submitted to Applied Radiations and Isotopes.  
Preprint available <https://arxiv.org/abs/1611.00213>.

V **Tagging fast neutrons from a  $^{252}\text{Cf}$  fission fragment source**

**J. Scherzinger**, R. Al Jebali, J.R.M. Annand, K.G. Fissum, R. Hall-Wilton, N. Mauritzson, F. Messi, H. Perrey, E. Rofors  
Manuscript submitted to Applied Radiations and Isotopes.  
Preprint available <https://arxiv.org/abs/1611.02940>.

PAPER I and PAPER II are reproduced under open access publishing, using the Creative Commons license CC BY 4.0.

PAPER III is reproduced under open access publishing, using the Creative Commons license CC BY-NC-ND 4.0.

# Other Publications to Date not Included in this Thesis

## I Detectors for the European Spallation Source

R. Hall-Wilton, C. Höglund, M. Imam, K. Kanaki, A. Khaplanov, O. Kirstein, T. Kittelmann, B. Nilsson, **J. Scherzinger**  
IEEE Nuclear Science Symposium and Medical Imaging Conference (2012) 4283 – 4289.

## II ESS Technical Design Report

S. Peggs *et al.*  
<https://europeanspallationsource.se/sites/default/files/tdr.pdf>, ISBN 978-91-980173-2-8, ESS-doc-274, 2013

## III Neutron Position Sensitive Detectors for the ESS

O. Kirstein, R. Hall-Wilton, I. Stefanescu, M. Etxegarai, M. Anastasopoulos, K.G. Fissum, A. Gulyachkina, C. Höglund, M. Imam, K. Kanaki, A. Khaplanov, T. Kittelmann, S. Kolya, B. Nilsson, L. Ortega, D. Pfeiffer, F. Piscitelli, J. Freita Ramos, L. Robinson, **J. Scherzinger**  
PoS (Vertex2014) 029.

IV Overcoming High Energy Backgrounds at Pulsed Spallation Sources

N. Cherkashyna, R. Hall-Wilton, D.D. Di Julio, A. Khaplanov, D. Pfeiffer, **J. Scherzinger**, C.P. Cooper-Jensen, K.G. Fissum, S. Ansell, E.B. Iverson, G. Ehlers, F.X. Gallmeier, T. Panzner, E. Rantsiou, K. Kanaki, U. Filges, T. Kittelmann, M. Extegarai, V. Santoro, O. Kirstein, P.M. Bentley  
JAEA-Conf 2015-002, <http://dx.doi.org/10.11484/jaea-conf-2015-002>. Preprint available at <https://arxiv.org/abs/1501.02364>

V Characterization of the radiation background at the Spallation Neutron Source

Douglas D. Di Julio, Nataliia Cherkashyna, **Julius Scherzinger**, Anton Khaplanov, Dorothea Pfeiffer, Carsten P. Cooper-Jensen, Kevin G. Fissum, Kalliopi Kanaki, Oliver Kirstein, Georg Ehlers, Franz X. Gallmeier, Donald E. Hornbach, Erik B. Iverson, Robert J. Newby, Richard J. Hall-Wilton, Phillip M. Bentley  
Journal of Physics: Conference Series, 746 (2016) 012033

# Contributions to Workshops and Conferences

## Talks

- I DNPLU–MAX IV–ESS Three-Party Detector Lab  
In-Kind and Collaborative Detector Meeting, Lund, Sweden, 2013
- II A Neutron Source Facility for Energy Dependent Detector Characterization  
SFAIR and Swedish Nuclear Physicists Meeting, Stockholm, Sweden, 2013
- III A Neutron Source Facility for Energy Dependent Detector Characterization  
Position Sensitive Neutron Detector Workshop, Jülich, Germany, 2014
- IV The Source Testing Facility at Lund University  
IEEE Nuclear Science Symposium and Medical Imaging Conference, Strasbourg, France, 2016

## Posters

- I Novel Scintillator Materials for Neutron Detection  
IKON 3, Lund, Sweden, 2012
  
- II Characterization of a Liquid Scintillator Detector  
IKON 3, Lund, Sweden, 2012
  
- III Characterization of a Liquid Scintillator Detector with an Americium-Beryllium source  
IKON 4, Lund, Sweden, 2013
  
- IV A broad-band neutron source facility for detector characterization  
IEEE Nuclear Science Symposium and Medical Imaging Conference, Seattle, USA, 2014

# Popular Scientific Summary

In late 2016, Lund is on the verge of becoming the center of accelerator-based material science in Europe. The MAX IV Laboratory, an electron synchrotron, was inaugurated in June 2016 with a scientific program to commence shortly and the European Spallation Source ERIC (ESS), a spallation neutron source, is presently under construction and anticipated to be fully operational by 2022. These facilities will put Lund firmly on the map as the location to conduct world-class research in advanced material science and engineering. And while both facilities share many scientific objectives, they provide access to very different probes of matter.

The soft photons produced at the MAX IV Laboratory preferentially interact with atomic electrons. In contrast, as neutrons are electrically uncharged, they tend to interact with the atomic nucleus. This makes neutrons highly penetrating particles and allows them to deeply probe samples. Further, neutrons have a magnetic moment. They can therefore be used to test magnetic properties of materials. As scattering cross sections are highly isotope dependent, neutrons are excellent probes for the identification of the isotopic composition of a sample. These properties make neutrons an ideal complementary probe to photons, which scale in their interaction strength by atomic number.

When constructed, ESS will be the neutron source with the highest neutron brilliance in the world. This makes ESS a technically challenging design with many firsts for the neutron-scattering community. With respect to neutron detection, two major challenges must be overcome to make ESS a success. First, the detectors of many instruments are designed to perform at never before seen neutron count rates and resolutions. Second, the lack of commercially available  $^3\text{He}$  has resulted in large-scale neutron detectors based on  $^3\text{He}$  technologies no longer being affordable. This new reality has resulted in a major effort worldwide to develop replacement neutron-

detector technologies. Many of these technologies are in their infancy and need to be thoroughly tested before becoming mainstream, while others are approaching commercialization and need to be certified. Still others, being commercially available today, need to be tested before being installed in instruments.

To test detector technologies in all three stages of development, neutron sources for controlled irradiation are needed. Such sources of neutrons include accelerators, nuclear reactors and radioactive sources. Neutrons produced in nuclear reactors and at accelerators have a very high cost-of-entry and a very high cost-per-neutron. In contrast, radioactive sources produce neutrons at a significantly lower cost-per-neutron and with a substantially lower cost-of-entry. The Source Testing Facility (STF) has been established in Lund to provide a source-based irradiation facility to academic users and industry.

In this work, the development of a fast-neutron test bed, the core component of the STF, is presented. The neutron-irradiation techniques subsequently discussed are based on well-understood nuclear-physics methods. In particular, the “neutron tagging” technique is employed to measure neutron energy by time-of-flight. Time-of-flight is simply the elapsed time between neutron emission from a source and neutron detection at a well-defined distance from the source. This technique is used to establish energy-dependent neutron-response functions of detectors. To improve the resolution of the measurements, particle identification methods such as pulse-height and pulse-shape discrimination are employed. This is possible because the signals produced by many detectors differ in amplitude or shape for different incident radiations.

This thesis presents an overview of the results of a successful, inaugural collaboration between the Division of Nuclear Physics at Lund University and the Detector Group of the European Spallation Source ERIC.

# Contents

List of Tables	xv
List of Figures	xvii
Introduction	I
<b>1 Background</b>	<b>3</b>
1 Radioactive Neutron Sources . . . . .	3
1.1 Actinide/Be Neutron Sources . . . . .	3
1.2 $^{252}\text{Cf}$ – a Spontaneous Fission Neutron Source . . . . .	7
2 Scintillation Light . . . . .	8
3 Scintillator Materials . . . . .	9
3.1 Organic Scintillators . . . . .	10
3.2 Inorganic Scintillators . . . . .	10
3.3 $^4\text{He}$ Noble-Gas Scintillator Detectors . . . . .	12
4 Scintillator Detectors . . . . .	13
5 Fast-Neutron Detection with Scintillator Detectors . . . . .	14
5.1 Detector Efficiency . . . . .	16
<b>2 Setup and Experimental Techniques</b>	<b>17</b>
1 Neutron Sources . . . . .	17
2 The Source Testing Facility . . . . .	18
3 Source Tank and Shielding . . . . .	18
4 Detectors . . . . .	21
4.1 The YAP Scintillator Detector . . . . .	21
4.2 The $\text{CeBr}_3$ Scintillator Detector . . . . .	21
4.3 The Liquid Scintillator Detectors . . . . .	22
4.4 The $^4\text{He}$ -based Neutron Diagnostic Tool . . . . .	23
4.5 The $^4\text{He}$ Fission-Fragment Detector . . . . .	24
5 Data Acquisition and Electronics . . . . .	25
6 Experimental Configuration . . . . .	26

7	Calibration of Liquid-Scintillator Detectors . . . . .	28
8	Pulse Shape Discrimination . . . . .	31
9	Energy-Tagged Fast-Neutrons and Time-of-Flight . . . . .	33
<b>3</b>	<b>Results</b>	<b>37</b>
	<b>Closing Remarks</b>	<b>39</b>
	<b>Acknowledgements</b>	<b>41</b>
	<b>Bibliography</b>	<b>43</b>
<b>A</b>	<b>Papers</b>	<b>51</b>
	Paper I: Tagging fast neutrons from an $^{241}\text{Am}/^9\text{Be}$ source . . . . .	55
	Paper II: A first comparison of the responses of a $^4\text{He}$ -based fast-neutron detector and a NE-213 liquid-scintillator reference detector . . . . .	63
	Paper III: The light-yield response of a NE-213 liquid-scintillator detector measured using 2 – 6 MeV tagged neutrons . . . . .	73
	Paper IV: A comparison of untagged gamma-ray and tagged-neutron yields from $^{241}\text{AmBe}$ and $^{238}\text{PuBe}$ sources . . . . .	83
	Paper V: Tagging fast neutrons from a $^{252}\text{Cf}$ fission fragment source . . . . .	101
<b>B</b>	<b>Posters</b>	<b>119</b>
	Poster I: Novel Scintillator Materials for Neutron Detection . . . . .	121
	Poster II: Characterization of a Liquid Scintillator Detector . . . . .	125
	Poster III: Characterization of a Liquid Scintillator Detector with an Americium- Beryllium source . . . . .	129
	Poster IV: A broad-band neutron source facility for detector characterization	133

# List of Tables

1.1	Neutron Energy Transfer . . . . .	15
2.1	Actinide-Beryllium Neutron Sources . . . . .	18
2.2	List of Electronic Modules . . . . .	26
2.3	Compton Edge Energies of $^{22}\text{Na}$ and $^{137}\text{Cs}$ . . . . .	29



# List of Figures

1.1	The Production of Fast Neutrons in the Lab Frame and in the Center-of-Mass Frame . . . . .	5
1.2	Actinide/Be Neutron Spectrum . . . . .	6
1.3	$^{252}\text{Cf}$ Neutron Spectrum . . . . .	7
1.4	Light Yield of NE-213 for Electrons, Protons and Heavy Ions . . . . .	9
1.5	The Scintillation Mechanism in Organic Scintillator. . . . .	11
1.6	The Scintillator Detector Concept . . . . .	13
1.7	The Basic Elements of a PMT . . . . .	14
1.8	Elastic Scattering . . . . .	15
1.9	Neutron Scattering Cross Sections . . . . .	16
2.1	Source Testing Facility . . . . .	19
2.2	The Aquarium . . . . .	20
2.3	YAP Detector . . . . .	21
2.4	$\text{CeBr}_3$ Detector . . . . .	22
2.5	NE-213 Detector . . . . .	23
2.6	NDT . . . . .	24
2.7	$^4\text{He}$ Scintillator Detector . . . . .	25
2.8	Tagged-Neutron Setup . . . . .	27
2.9	$^{252}\text{Cf}$ Setup . . . . .	27
2.10	$^{22}\text{Na}$ Gamma-Ray Spectrum of the NE-213 Detector . . . . .	29
2.11	Energy Calibration of the NE-213 Detector . . . . .	30
2.12	Measured and Simulated Response of NE-213 to $^{22}\text{Na}$ Gamma-Ray Field . . . . .	30
2.13	Pulse Shape in NE-213 . . . . .	31
2.14	Integrated Pulse Shape . . . . .	32
2.15	Contour Plot of PS versus L of NE-213. . . . .	33
2.16	Schematic Drawing of a Time-of-Flight Measurement . . . . .	34

2.17	Time-of-Flight Spectrum . . . . .	35
2.18	Tagged-Neutron Spectra . . . . .	36

# Introduction

Neutrons are important probes of matter [1, 2, 3, 4, 5, 6, 7] and are used in a wide variety of fields from fundamental physics and material science to geological studies and homeland-security applications. Their particle properties make them an ideal candidate for imaging. They are electrically uncharged and deeply penetrating and can probe the interior of large and dense structures. Neutron scattering cross sections have a high isotope dependency which makes neutrons an ideal probe of the isotope composition of samples. Further, as they are spin-1/2 fermions, they have a magnetic moment which allows for the magnetic properties of materials to be probed.

However, the drawback associated with using neutrons is that they are difficult to detect. Neutrons, unlike charged particles, cannot be detected by their direct ionization of the detector medium. Instead, neutrons must be detected indirectly by a reaction. This reaction can be either elastic scattering on a light target nucleus (protons or  $^4\text{He}$ ) used to detect fast-neutrons ( $>0.5$  MeV) or it can be a nuclear capture reaction on high cross section isotopes ( $^6\text{Li}$ ,  $^{10}\text{B}$  and  $^3\text{He}$ ) used for cold ( $\sim 2.2$  meV), thermal ( $\sim 25$  meV) or epithermal ( $\sim 1$  eV) neutrons. The charged products from these reactions can then ionize the detector medium or produce scintillation light. In either case, neutrons are detected when the freed charges are collected or when the scintillation photons are detected with a photo-sensitive device. In both cases, the ultimate result is an electric signal.

One of the most common detector materials for neutrons of all energies is  $^3\text{He}$  which is a high cross section neutron converter for thermal neutrons and is used together with moderators to detect fast neutrons.  $^3\text{He}$  is one of the two stable helium isotopes, but its natural abundance is only 0.000137%. It has been produced as a byproduct of the nuclear weapons programs in the USA and the former Soviet Union.  $^3\text{He}$  is created when tritium ( $^3\text{H}$ ) decays by beta decay. In the last decade, the stockpile of

this scarce substance was depleted and its price has become too great for large-scale detector applications [8, 9, 10]. This  $^3\text{He}$  “crisis” [8, 9, 10, 11, 12] has triggered an interest in the development of new detector technologies to be used for large-area detectors [13, 14]. Many of these “replacement” technologies are still in their infancy [15], while others have been successfully tested and are approaching maturity [16] and still others have been in common use for years [17].

In order to become established, new technologies need to be carefully characterized in well-defined laboratory environments. Essential to these tests are sources of neutrons for controlled irradiations – accelerators, nuclear reactors and radioactive sources. Neutrons produced in nuclear reactors and in accelerator environments have a very high cost per neutron. In contrast, radioactive sources produce neutrons at a substantially lower cost per neutron and are (after a one-time investment) continuously available. Some of the drawbacks associated with using radioactive sources are the broad neutron-energy spectrum and the intense gamma-ray field that is associated with them. It follows that the use of radioactive neutron sources is often limited to early detector functionality tests. But by using advanced experimental techniques, radioactive sources can be employed beyond these initial detector tests.

This work describes the conceptualization, development and implementation of source-based fast-neutron irradiation techniques performed for the recently established Source Testing Facility (STF) at the Division of Nuclear Physics at Lund University. The main focus is on the development and subsequent use of a cost-efficient precision test bed for the production of “tagged” neutrons from actinide/Be sources and a  $^{252}\text{Cf}$ , a spontaneous fission source. At this test bed, well-understood shielding, coincidence, and time-of-flight measurement techniques are employed to attenuate and subsequently unfold the mixed decay-product radiation field provided by the sources, resulting in a polychromatic energy-tagged neutron beam useful for characterizations of detector response, gamma-ray rejection, and detector efficiency.

# Chapter 1

## Background

In this chapter, some theory behind detecting neutrons from radioactive sources with scintillator detectors is given. The mixed-field neutron/gamma-ray sources used in this work are introduced. The intrinsic properties of scintillator materials and the different scintillation processes in organic scintillators, inorganic scintillators and noble-gas scintillators are presented. The general detector concept of scintillator detectors is presented. Last, the detection of fast neutrons with scintillator detectors is discussed.

### 1 Radioactive Neutron Sources

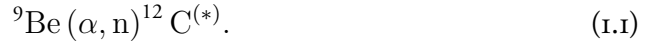
In radioactive sources, neutrons are produced by nuclear reactions following the radioactive decay of an unstable isotope. They are used widely in such diverse fields as landmine detection [18], education [19], detector characterizations [20] and oil-well logging [21]. In this thesis, two types of radioactive neutron sources (actinide/<sup>9</sup>Be sources and the spontaneous fission source <sup>252</sup>Cf) were employed to characterize fast-neutron detectors with source-based neutron-irradiation techniques.

#### 1.1 Actinide/Be Neutron Sources

Neutrons produced by actinide/Be sources have been essential to the field of neutron physics since the discovery of the neutron by Chadwick [22] in 1932. Chadwick

used a polonium alpha-particle source and a  ${}^9\text{Be}$  target to produce neutrons in his famous experiment. Today, the most commonly employed neutron sources of the actinide/Be type are either mixed-isotope Pu [23, 24, 25] or  ${}^{241}\text{Am}$  [26, 27, 18]. The Pu-based sources are often legacy sources from the 1970s and earlier, while Am/Be sources continue to be supplied commercially.

In actinide/Be sources most of the fast neutrons ( $E > 0.5$  MeV) are produced when an alpha-particle interacts with  ${}^9\text{Be}$  to produce  ${}^{12}\text{C}$  and a fast neutron according to:



When  ${}^{12}\text{C}$  is produced in the ground state, the  $Q$ -value, which is the energy released in the nuclear reaction, can be calculated from the mass-difference of the initial particles and the final products according to:

$$Q = m_{{}^9\text{Be}} + m_\alpha - m_n - m_{{}^{12}\text{C}}, \quad (1.2)$$

where  $m_{{}^9\text{Be}}$  is the mass of  ${}^9\text{Be}$ ,  $m_\alpha$  is the mass of the alpha particle,  $m_n$  is the neutron mass and  $m_{{}^{12}\text{C}}$  is the mass of  ${}^{12}\text{C}$ . The reaction is exothermic with a  $Q$ -value of 5.7 MeV. From a purely kinematic view, the reaction is possible for alpha-particles with a kinetic energy of 0 MeV.

The interaction  ${}^9\text{Be}(\alpha, n){}^{12}\text{C}$  is illustrated in Fig. 1.1 for both the lab system and the center-of-mass system. The neutron energy can be calculated from the reaction kinematics. In the lab system, energy and momentum conservation equations can be rearranged to correlate the neutron energy  $E_n$  to the neutron scattering angle  $\theta$ , the  $Q$ -value and the alpha-particle energy  $E_\alpha$  [28]:

$$Q = E_n \left( 1 + \frac{m_n}{m_{{}^{12}\text{C}}} \right) - E_\alpha \left( 1 - \frac{m_\alpha}{m_{{}^{12}\text{C}}} \right) - \frac{2}{m_{{}^{12}\text{C}}} \sqrt{m_\alpha m_n E_\alpha E_n} \cos \theta. \quad (1.3)$$

Equation 1.3 allows for the investigation of some properties of actinide/Be sources governed by reaction kinematics. Neutrons correlated to the ground state of  ${}^{12}\text{C}$  ( $n_0$ ) have a well-defined emission energy range. The minimum energy for  $n_0$  neutrons can be estimated by setting the alpha-particle energy to 0 MeV in Eq. 1.3.

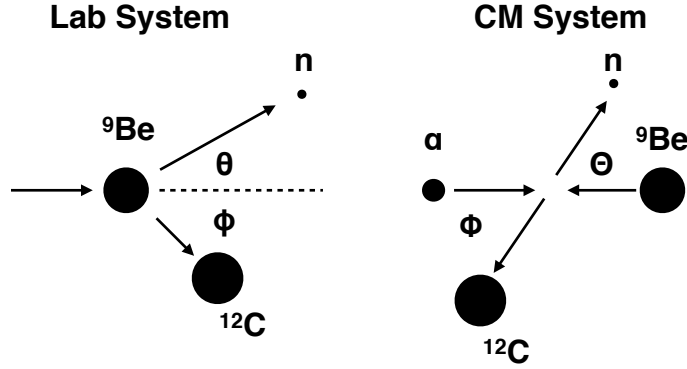


Figure 1.1: Fast neutron production in the  $^{12}\text{C}$  channel in both the lab system (to the left) and the center-of-mass system (to the right).

$$E_{n,0}^{\min} (E_{\alpha} = 0) = Q \frac{m_{^{12}\text{C}}}{m_{^{12}\text{C}} + m_n} \approx \frac{12}{13} Q = 5.27 \text{ MeV}. \quad (1.4)$$

The real minimum energy of  $n_0$  neutrons will be slightly higher than this value due to Coulomb repulsion between the alpha-particle and  $^9\text{Be}$ . The maximum possible neutron energy  $E_{n,0}^{\max} = 11.04 \text{ MeV}$  for a maximum alpha-particle energy of  $E_{\alpha}^{\max} \sim 5.5 \text{ MeV}$  results from scattering in forward direction  $\theta = 0$

$$0 = \frac{13}{12} E_n - \frac{1}{3} \sqrt{E_{\alpha}^{\max}} \sqrt{E_n} - \frac{2}{3} E_{\alpha}^{\max} - Q, \quad (1.5)$$

where  $\cos \theta$  was set to 1. The exact nuclear masses were replaced with their mass numbers to simplify the equation. If  $\sqrt{E_n}$  is replaced with the variable  $x$ , Eq. 1.5 is a simple quadratic equation and can be solved analytically.

For neutrons corresponding to the first excited state of  $^{12}\text{C}$  ( $n_1$ ), the general reaction mechanism is similar. However, the energy released by the scattering interaction is reduced by 4.44 MeV, the excitation energy of the first excited state of  $^{12}\text{C}$ . Following the same investigation as before, a maximum neutron energy is  $E_{n,1}^{\max} = 6.37 \text{ MeV}$  and a minimum neutron energy is  $E_{n,1}^{\min} = 1.16 \text{ MeV}$ .  $^{12}\text{C}$  in the first excited state de-excites by the emission of a 4.44 MeV gamma-ray.

The energy released by the mass difference of the initial particles and the reaction products is not large enough to excite the second excited state of  $^{12}\text{C}$ . This means there is a kinematic reaction threshold for alpha-particles. A minimum energy can be

calculated for each scattering angle  $\theta$ . The smallest value is at  $\theta = 0^\circ$  and the absolute threshold energy  $E_\alpha^{\min} \approx 2.82$  MeV is given by:

$$E_\alpha^{\min} \approx (Q - E_{12C}^{x,2}) \frac{m_{12C} + m_n}{m_{12C} + m_n - m_\alpha}. \quad (I.6)$$

The minimum neutron energy is therefore  $E_{n,2}^{\min} = 0$  MeV and the maximum energy can be calculated to be  $E_{n,2}^{\max} = 2.79$  MeV.

Figure 1.2 shows the ISO 8529-2 reference spectrum for Am/Be sources in blue.

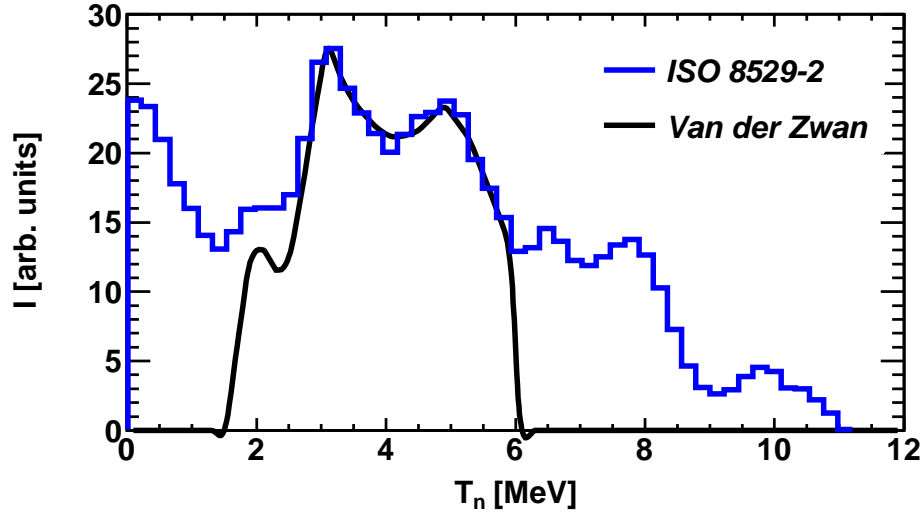


Figure 1.2: The ISO 8529-2 reference neutron spectrum (blue) and a theoretical neutron spectrum (black) corresponding to the first excited state of  $^{12}\text{C}$  as calculated by van Der Zwan [29].

The mean energy of the spectrum is  $\sim 4.5$  MeV and the maximum is located at  $\sim 11$  MeV. The theoretical neutron spectrum corresponding to the first-excited state of  $^{12}\text{C}$  as calculated by van Der Zwan [29] is shown in black. This calculated energy spectrum is limited to energies between  $\sim 1.5$  MeV and 6.2 MeV. The minimum neutron energy associated with the excitation of the first excited state of  $^{12}\text{C}$  is  $\sim 1.5$  MeV. The energy of fast neutrons from actinide/Be sources accompanied by 4.44 MeV gamma-rays is therefore limited for energies between 1.5 – 6.5 MeV.

## 1.2 $^{252}\text{Cf}$ – a Spontaneous Fission Neutron Source

$^{252}\text{Cf}$  has a half-life of 2.645 years and decays by alpha-emission (96.908%) and spontaneous fission (3.092%). Neutrons are produced when a  $^{252}\text{Cf}$  nucleus breaks up by spontaneous fission. The daughter nuclei resulting from a fission event are highly excited and release some of their excess energy by neutron emission. The average neutron energy is  $\sim 2$  MeV and the maximum neutron yield per fission event is between 0.5 MeV and 1 MeV. Above 10 MeV, the neutron yield is quite reduced. A typical fission spectrum (see Fig. 1.3) can be approximated to first order by a Maxwell-Boltzmann function [30, 31, 32]

$$\frac{dN}{dE} = A \cdot T^{3/2} \cdot \sqrt{E} \cdot \exp\left(-\frac{E}{T}\right), \quad (1.7)$$

where  $T$  is the effective temperature ( $T=1.42$  MeV),  $E$  is the energy of the emitted neutron and  $A$  is a scaling parameter to adjust for source intensity. The mean energy of the emitted neutron is  $\bar{E} = \frac{3}{2} \cdot T$ .

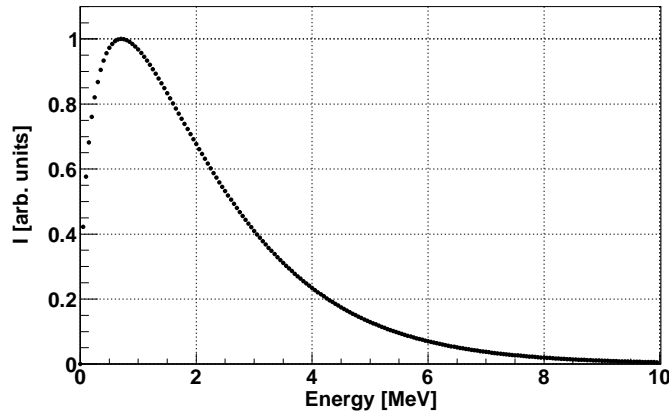


Figure 1.3: The Maxwell-Boltzmann distribution approximating the  $^{252}\text{Cf}$  Spectrum.

The model assumes that the  $^{252}\text{Cf}$  nucleus is in thermal equilibrium at temperature  $T$  and that neutrons “boil off” with a statistical energy distribution consistent with that of standard gas molecules.

## 2 Scintillation Light

Scintillation light is a form of luminescence that results from the de-excitation of electron states which were excited by the interaction with ionizing radiation. Depending on the time scale of the de-excitation, it is common to divide the emitted scintillation light into two groups: phosphorescent light for slow decays ( $\tau \geq 1\mu\text{s}$ ) and fluorescent light for fast decays ( $\tau \sim 1\text{ns}$ ). Both time scales can be correlated to different electron excitation-states, singlet or triplet. Fluorescence corresponds to photo-emissions from de-excitation of an excited singlet state to a lower state of the same spin multiplicity. Singlet-singlet transitions are quantum mechanically favored and are therefore fast. Phosphorescence corresponds to photo-emissions from the de-excitation of an excited triplet state to a lower singlet state. Triplet-singlet transitions are quantum mechanically forbidden and the decays are thus delayed.

Scintillation in most materials is an inefficient process and scintillators convert only a small fraction of the energy deposited by ionizing radiation into scintillation light. Most of this energy is lost to heat and vibrational excitation and not available for light production. The fraction of the deposited energy that becomes scintillation light, the scintillation efficiency  $S$ , depends for most scintillator materials on both the type of ionizing radiation and the incident particle energy. This is explained by a reduction of the scintillation efficiency (quenching) of (organic) molecules damaged by the high ionization density of protons and heavy ions. If  $S$  is independent of the particle energy, the light yield  $L$ , the amount of scintillation light produced, is linear with respect to the incident particle energy. This is the case for all particles in noble-gas scintillator detectors and for electrons in both inorganic and organic (above 100 keV) scintillator materials.

The amount of scintillation light  $\frac{dL}{dx}$  created by a particle per unit path length is given by [30]

$$\frac{dL}{dx} = S \frac{dE}{dx}, \quad (1.8)$$

where  $\frac{dE}{dx}$  is the energy deposition per unit path length. The density of damaged molecules along the path of a particle is to good approximation directly proportional to the ionization density of the particle. The damaged molecule density can therefore be estimated to be  $B \frac{dE}{dx}$ , where  $B$  is a proportionality constant. If quenching occurs in only a fraction  $k$  of these damaged molecules, the light yield  $L$  of a proton and

heavy ion can be estimated by [33, 30]

$$\frac{dL}{dx} = \frac{S \frac{dE}{dx}}{1 + kB \frac{dE}{dx}} \quad (1.9)$$

The different light yields of a NE-213 liquid scintillator detector for electrons, protons, alpha-particles and  $^{12}\text{C}$  are shown in Fig. 1.4. A more detailed description of light production in scintillators can be found in [30, 33, 34].

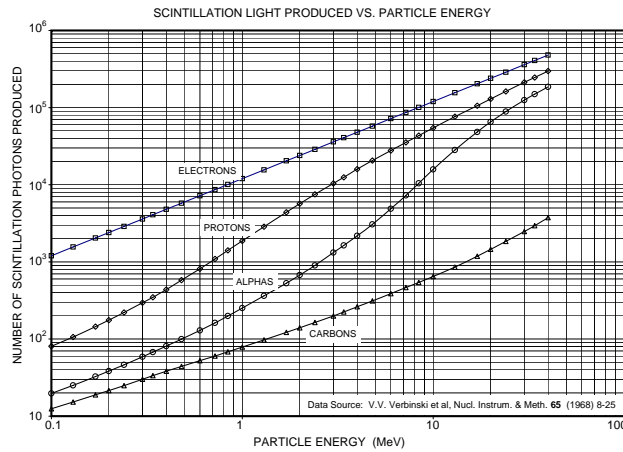


Figure 1.4: The light yield of NE-213 for electrons, protons, alpha-particles and  $^{12}\text{C}$ . The non-linear light production and the quenching of the light yield from protons and ions can be clearly identified. Figure from [35].

### 3 Scintillator Materials

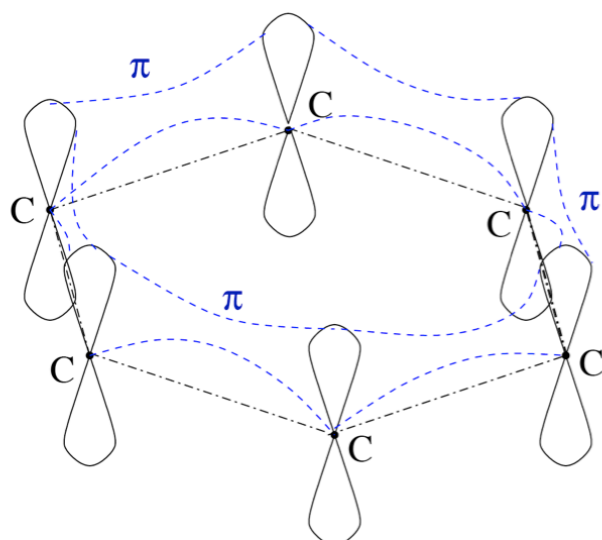
Scintillators come in all states of matter and the fundamental interactions leading to scintillation light are diverse. It is often convenient to divide scintillator materials into three groups: organic scintillators, inorganic scintillators, and noble-gas scintillators. Organic scintillators are mixtures of aromatic molecules which are in liquid solutions, plastics or organic crystals. Inorganic scintillators come in a wide variety of states such as single crystals, glasses, ceramics and gases. Noble-gas scintillators can be used as gases or liquids. In this work, a liquid organic scintillator (NE-213 based on xylene), two inorganic crystals (YAP and  $\text{CeBr}_3$ ) and two  $^4\text{He}$  noble-gas scintillator detectors are employed.

### 3.1 Organic Scintillators

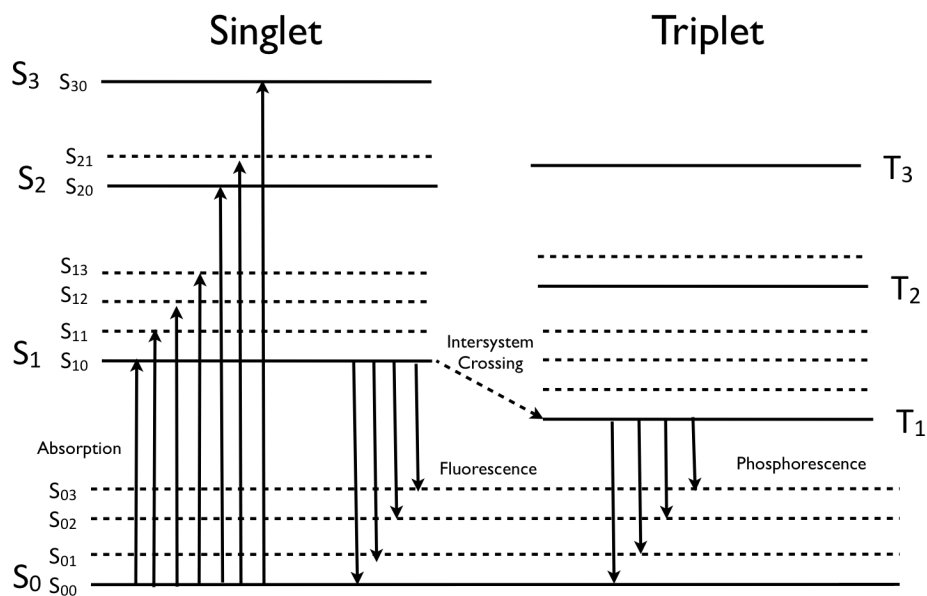
Organic scintillators consist of aromatic organic molecules, hydrocarbons with benzene like cyclo-hexal structures (see Fig. 1.5 (a)). Carbon atoms have four available valence electrons and form with hydrogen either saturated hydrocarbons or molecules with double or triple electron bonds. In aromatic molecules, carbon atoms form double bonds and one s-orbital and two p-orbitals combine to three equivalent orbitals ( $sp^2$  hybridization). Such  $\sigma$ -electrons are strongly bound and the orbitals do not produce luminescence. However, the last p-orbital is symmetric with respect to the molecular plane and the associated electron is called a  $\pi$ -electron. Such  $\pi$ -electrons are weakly bound (see Fig. 1.5 (a)) and form in aromatic molecules one de-localized orbit. In organic scintillators, scintillation is caused by transitions from the excited states of these  $\pi$ -orbitals to the ground state. An electron excitation diagram of the  $\pi$ -molecular orbitals is shown in Fig. 1.5 (b) [30]. The different energy levels are a result of the relative spin orientation of the excited electron, compared to the spin orientation of the unpaired electron in the ground state, in either parallel (triplet  $T_i$ ) or anti-parallel alignment (singlet  $S_i$ ). The vibrational excitation states ( $S_{ij}$ ) arise from the collective motion of atoms in a molecule. The de-excitation from the singlet state  $S_1$  to  $S_0$  (fluorescence) by the emission of light is a fast ( $\sim$  ns) process. The excited triplet state  $T_1$  de-excites by slower processes. The highly forbidden transition process  $T_1 \rightarrow S_0$  (phosphorescence) has a time scale of  $\mu$ s or longer. The most common way to de-excite the  $T_1$  states is indirect delayed-luminescence via  $S_1 \rightarrow S_0$ . This process is considerably faster than phosphorescence and responsible for the delayed part of scintillator light pulses in organic scintillators.  $T_1$  can be excited by inter-molecular interaction to singlet states. For a detailed description of scintillation in organic scintillators, see [30, 33]

### 3.2 Inorganic Scintillators

Scintillation-light production in inorganic scintillators depends on the energy states of the crystal lattices of the material. In crystals, electrons have only discrete energy levels available which form clearly separated energy bands. Electrons in the the valence band, the lower energetic band, are strongly bound at the lattice site. Electrons in the conduction band have sufficient energy to freely migrate through the crystal. In the band gap of a pure crystal, the energy levels between the valence band and the conduction band, no electrons are found. If energy is absorbed by the crystal, an electron from the valence band can be excited to the conduction band.



(a)



(b)

Figure 1.5: The scintillation mechanism in organic scintillator. (a) A representation of the  $\pi$ -orbital (dashed line) structure of aromatic hydrocarbons. The original p-orbitals forming the delocalized  $\pi$ -orbital are also shown. Figure from [36]. (b) A schematic representation of the excitation states of organic scintillators. Figure from [30].

The hole left by such a process can then be filled again if the electron returns to the valence band resulting in the emission of light. It is important to remember that in pure crystals this process has two major drawbacks for detectors. First, the excited electron state has a long life time and the light emission process is often delayed ( $\sim 100$  ms). Second, the band gap in typical scintillator materials is large ( $\sim 4$  eV) and the emitted (UV) light is outside the sensitivity range of photo-multiplier tubes (PMTs) (see Sec. 4).

To increase the amount of visible scintillation light, small amounts of impurities are regularly added to inorganic scintillators. These activator atoms create locations in the crystal lattice where the energy-band structure of the pure crystal is modified. The activators are normally chosen to create new energy states in the otherwise forbidden energy-band gap. Electrons can now de-excite in a two-step process through the intermediate activator state. The light emitted by these transitions will be shifted to lower energies compared to the full band gap and can be detected with PMTs. For a more detailed explanation of the scintillation process in inorganic scintillators, see [30, 33, 34].

### 3.3 $^4\text{He}$ Noble-Gas Scintillator Detectors

Noble-gas scintillators are used in modern detectors as both gases and liquids. They have the advantage that their light yield is linear for almost all charged particles and energies [33] and thus no particle quenching is observed. While the mechanism producing scintillation light is relative simple in that ionizing radiation excites gas molecules, the precise emission spectrum of a noble-gas scintillator is the result of ion recombination and its de-excitation process and is quite complex. The spectrum is the product of several different states of the gas atoms (atomic ions, molecular ions, excited dimers) and of different excitation states of the non-ionized molecules. Many of these de-excitation processes are fast and the decay times are on the order of ns or less. This makes noble-gas scintillator detectors one of the fastest radiation detector types available. The scintillation light emitted by noble-gas scintillators is ultra-violet ( $\sim 390$  nm for  $^4\text{He}$  at atmospheric pressure). To shift the light to longer wavelengths in the PMT sensitive region (visible light), wavelength shifters have to be employed. This can be either done by painting the scintillation cell with a special coating such as EJ-298 [37] or by adding a small quantity ( $\sim 500$  ppm) of a second gas like nitrogen. For a more detailed explanation of the scintillation process in noble-gas scintillators, see [33].

## 4 Scintillator Detectors

The general detector concept is the same for all three scintillator types employed in this thesis. The scintillation material is enclosed in a light-tight housing which can be thin aluminum layers and black tape for plastic scintillators or several millimeter thick metal cells for gas scintillators. The inside of this housing is often covered with a reflective material, polished metal or reflective paint. If a particle interacts in the detector medium, it creates scintillation light. This light is focused onto a light detector which is optically coupled to the scintillator material with a window and a non-scintillating light guide. For solid materials, direct coupling between the scintillator material and the light detector is also possible. Figure 1.6 illustrates this concept for a liquid-scintillator detector interacting with a neutron. The most common light sensitive devices used to register scintillation light are photo-multiplier tubes (PMTs). Figure 1.7 shows a schematic drawing of a PMT. An evacuated glass tube is the outer envelope containing the photo-cathode, a photo-sensitive metal layer, and the electron-multiplying dynode assembly. The photocathode transforms  $\sim 25\%$  of the incident light quanta into photo-electrons [30].

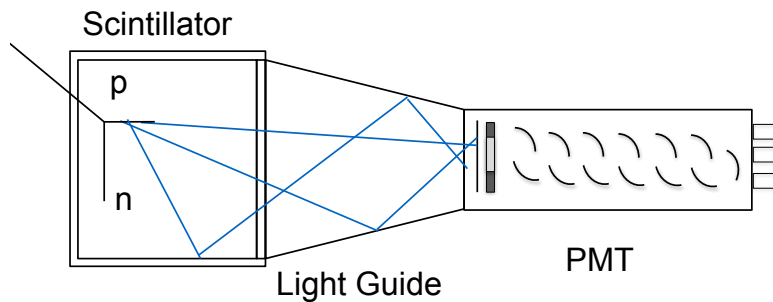


Figure 1.6: The basic concept behind a scintillator detector. Scintillation light is produced by a neutron-induced recoiling proton. The light is guided from the detector cell through the light guide to the photo-cathode.

Focusing electrodes guide the primary electrons to the first multiplying dynode. The electron number increases throughout the dynode system in an avalanche-like process. The amplified pulse eventually strikes the anode and the resulting anode current can be measured.

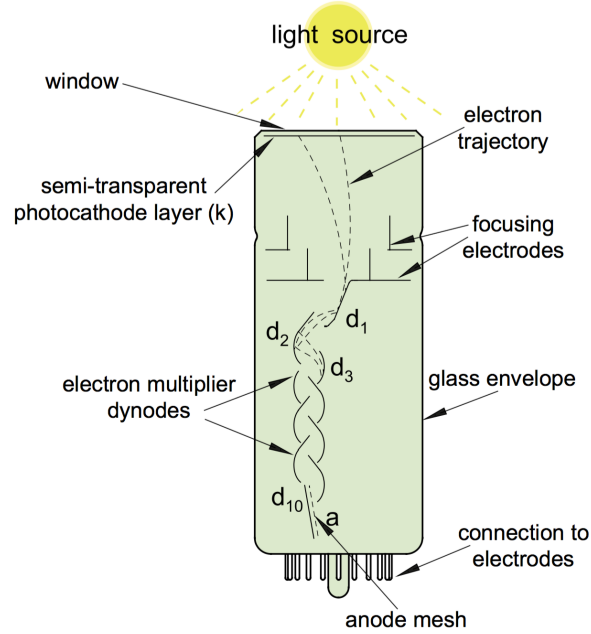


Figure 1.7: The basic elements and functions of a PMT. Light is converted on the photo-cathode into electrons. The focusing electrodes and electron multiplier dynodes are also shown. Figure from [38].

## 5 Fast-Neutron Detection with Scintillator Detectors

Neutrons are electrically uncharged particles which are detected by reactions with the detector medium. The preferred detection reactions are energy dependent. Neutrons can be captured on high cross section target isotopes such as  $^{10}\text{B}$ ,  $^6\text{Li}$ ,  $^{155,157}\text{Gd}$  and  $^3\text{He}$ . This is the predominant detection concept for cold ( $\sim 2.2$  meV), thermal ( $\sim 25$  meV) and epithermal ( $\sim 1$  eV) neutrons. For fast neutrons ( $>0.5$  MeV) elastic neutron-nucleus scattering is employed as the more common detection technique. Figure 1.8 shows the elastic neutron-nucleus scattering process in the laboratory frame and in the center-of-mass frame. The energy of the recoil nucleus in the lab system can be calculated for non-relativistic neutrons by:

$$E_R = \frac{4A}{(1+A)^2} \cos^2(\theta) E_n, \quad (1.10)$$

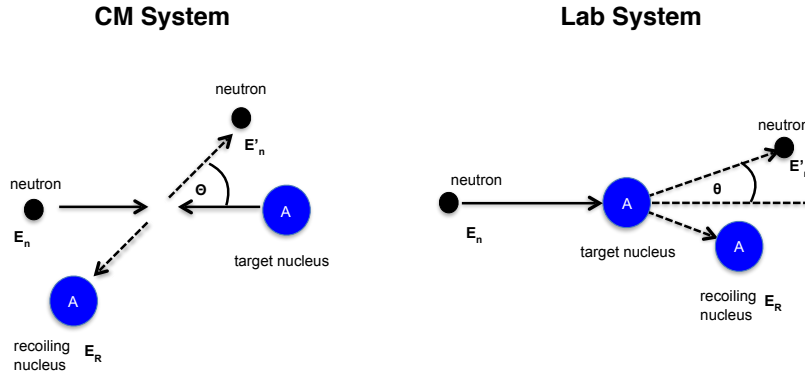


Figure 1.8: Elastic scattering of an incoming neutron of the energy  $E_n$  and the target nucleus with recoil energy  $E_R$  in the center-of-mass frame on the left side and in the lab fram on the right side. Figure from [30]

where  $A$  is the mass number of the target nucleus,  $E_R$  is the kinetic energy of the recoil nucleus,  $\theta$  represents the scattering angle of the scattered nucleus in the lab frame and  $E_n$  is the kinetic energy of the neutron [30]. Equation 1.10 shows that the energy transfer is inversely proportional to the mass number of the target nucleus and hence light targets are preferred. The maximum energy transfer to some of the typical target materials in fast-neutron detectors are listed in Table 1.1.

Table 1.1: Maximum neutron–energy transfer for different target isotopes.

Target	A	Maximum Energy Transfer
$^1\text{H}$	1	1.000
$^2\text{H}$	2	0.889
$^3\text{He}$	3	0.750
$^4\text{He}$	4	0.640
$^{12}\text{C}$	12	0.284
$^{16}\text{O}$	16	0.211

Table 1.1 shows that hydrogen and helium are the preferred target materials for elastic neutron scattering. In NE-213 liquid scintillator made from hydrogen and  $^{12}\text{C}$ , neutrons are detected mainly by elastic neutron-proton scattering. In  $^4\text{He}$ -based scintillator detectors, elastic neutron- $^4\text{He}$  scattering is the main detection mechanism.

## 5.1 Detector Efficiency

The neutron detection-efficiencies of NE-213 liquid-scintillator neutron detectors and of  $^4\text{He}$  noble-gas neutron detectors are correlated to the elastic-scattering cross section  $\sigma_s$ . The energy-dependent neutron elastic-scattering cross sections of protons,  $^4\text{He}$  and  $^{12}\text{C}$  are shown in Fig. 1.9. The cross sections of the two most important components in organic scintillators, protons and  $^{12}\text{C}$ , are of similar strength in the region of interest between 1 MeV and 10 MeV. Elastic scattering on  $^{12}\text{C}$  produces next to no scintillation light because the recoiling  $^{12}\text{C}$  has a large quenching factor in organic scintillators (see Fig. 1.4). The cross section of  $^4\text{He}$  is of the same magnitude as that of protons.

For a single component detector, the intrinsic neutron-detection efficiency  $\epsilon$  is given by:

$$\epsilon = 1 - \exp(-N\sigma_s d), \quad (1.11)$$

where  $N$  is the number density of the target material,  $\sigma_s$  is the elastic scattering cross section and  $d$  is the path length of the neutrons through the detector [30].

Organic scintillators, such as NE-213, are to good approximation two-component materials and scattering on  $^{12}\text{C}$  has to be taken into consideration. If multiple scattering is neglected, the neutron-detection efficiency can be calculated [30]:

$$\epsilon = \frac{N_H\sigma_H}{N_H\sigma_H + N_C\sigma_C} \{1 - \exp(-(N_H\sigma_H + N_C\sigma_C)d)\}, \quad (1.12)$$

where  $N_H$  is the number density of the protons,  $N_C$  is the number density of  $^{12}\text{C}$ ,  $\sigma_H$  the elastic scattering cross section for protons,  $\sigma_C$  the elastic scattering cross section for  $^{12}\text{C}$  and  $d$  the path length of incident neutron through the detector [30].

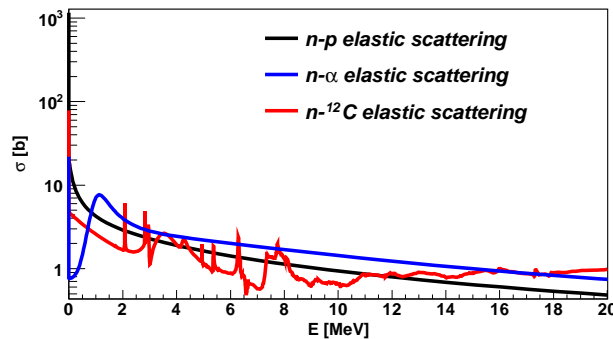


Figure 1.9: Elastic neutron scattering cross section of protons,  $^4\text{He}$  and  $^{12}\text{C}$ . The Figure was created with data from [39].

## Chapter 2

# Setup and Experimental Techniques

In this chapter, an overview of the measurement setup and the experimental techniques is given. The neutron sources, the laboratory environment of the Source Testing Facility (STF), the shielding, the detectors and the data-acquisition systems are described. The detector calibration of the liquid-scintillator detectors, the pulse-shape discrimination technique and the time-of-flight technique for the detection of energy-tagged fast neutrons are presented.

### I Neutron Sources

The four different neutron sources used for this work and some of their properties are listed in Table 2.1. The three actinide/Be sources are all housed in robust X.3 type cylinders of tig-welded, double-layered stainless steel, and are 31 mm in height and 22.4 mm in diameter. The alpha-particles from the decay of the actinide isotopes are therefore completely stopped in the capsules. The active diameter of the  $^{252}\text{Cf}$  source is 5 mm and one side is sealed by a  $50\mu\text{g}/\text{cm}^2$  sputtered gold film. Alpha-particles and fission fragments can escape through this thin gold layer.

Table 2.1: An overview of the properties of the neutron sources employed in this work.

Location	STF	STF	STF	The MAX IV Laboratory
	$^{241}\text{Am}/^9\text{Be}$	$^{238}\text{Pu}/^9\text{Be}^a$	$^{252}\text{Cf}$	$^{241}\text{Am}/^9\text{Be}$
Supplier	High Technology Sources (HTS) [40]	The Radiochemical Centre Amersham [41]	Eckert and Ziegler [42]	HTS
year of production	2015	1972	2015	2010
neutron yield	$1.1 \cdot 10^6 \frac{n}{s}$	–	$0.4 \cdot 10^6 \frac{n}{s}$	$1.1 \cdot 10^6 \frac{n}{s}$
nominal activity	18.5 GBq	–	3.7 MBq	18.5 GBq
unwanted radiation	$\gamma$ -ray $\sim 60$ keV	n/a	n/a	$\gamma$ -ray $\sim 60$ keV

<sup>a</sup>Additional information available upon request.

## 2 The Source Testing Facility

The Source Testing Facility has been established at Lund University in a joint effort between the Division of Nuclear Physics and the Detector Group of the European Spallation Source ERIC (ESS). Envisioned as a user-facility, the STF not only provides access to a wide array of neutron and gamma-ray sources but also to all infrastructure necessary for neutron-detector development and shielding studies. It is located next to the Lund Ion-Beam Analysis Facility (LIBAF) [43].

A schematic 3-D drawing of the STF is shown in Fig. 2.1. The interlocked irradiation area is shown on the left side of the figure. This is the space where irradiations are performed. The interlocked area is separated from the main part of the STF by an access-controlled gate. Patch-panels route signals, high voltage and gas connections to the DAQ area on the right side of the gate. Here, the measurements can be remotely controlled and data-acquisition performed. Additional storage space for detectors and electronics as well as a staging area for equipment are also provided.

## 3 Source Tank and Shielding

A major component of the apparatus located at the STF is a water-filled tank (see Fig. 2.2), known as the Aquarium. It is located in the interlocked area of the STF and is used to define beams from the mixed neutron/gamma-ray radiation field that

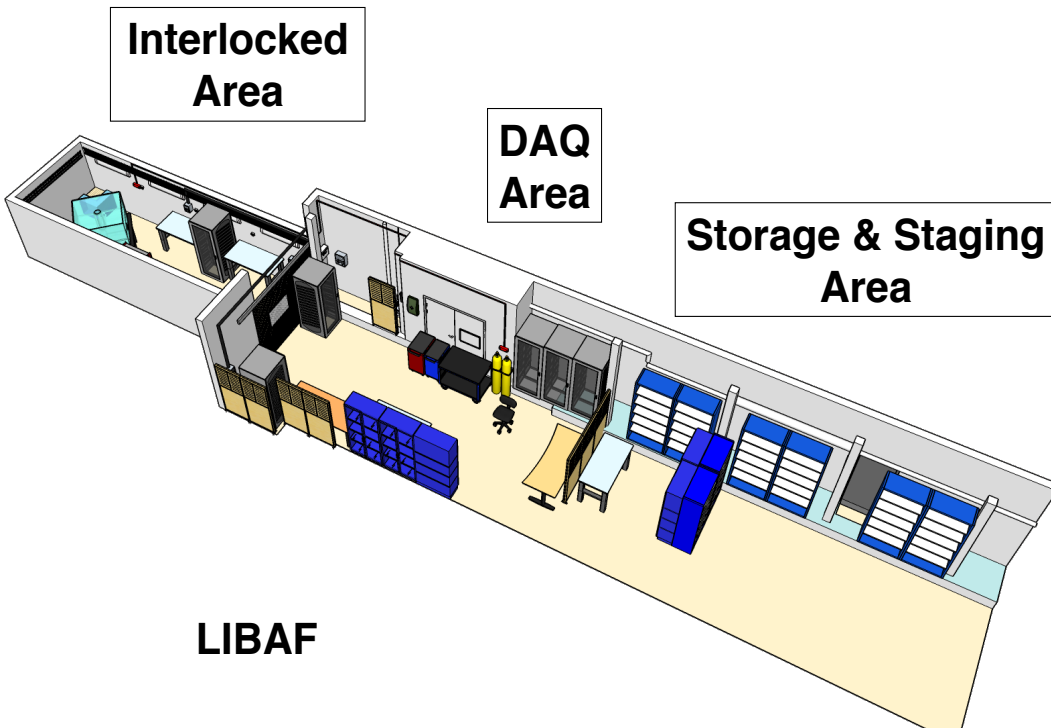


Figure 2.1: A schematic drawing of the STF. The interlocked area, the DAQ area and the detector storage and staging area are identified by the boxed labels. The position of the LIBAF is indicated. The original schematic drawing was supplied by Nicholai Mauritzson.

is emitted by a neutron source. The design of the Aquarium was developed with both functionality and safety in mind. First tests with the neutron sources were performed with temporarily assembled shielding made from concrete blocks, borated paraffin boxes and water jugs. The paraffin boxes were judged to be inappropriate for permanent shielding due to the associated fire hazard. It was therefore decided to employ water for the bulk shielding. A FLUKA [44] simulation<sup>1</sup> was used to determine the minimum thickness of pure-water shielding which could reduce the total dose rate at 1 m from the exterior surface of the source tank to less than  $0.5 \mu\text{Sv/h}$ . If the actinide/Be

<sup>1</sup>The simulation was written as part of a radiological evaluation of the MAX IV Laboratory Am/Be source performed by Dr. Magnus Lundin of the Radiation Safety Group at the MAX IV Laboratory [45].

sources are located in the park position within the Aquarium, the construction fulfills this requirement<sup>2</sup>. The Aquarium is made from poly-methyl-methacrylate (PMMA), also known as plexiglass and lucite, and was produced by VINK in Malmö [46] in a three part modular design of lower tank, upper tank and inner tank (see Fig. 2.2). The Aquarium has outer dimensions of 1400 mm × 1400 mm × 1400 mm.

A modular design concept<sup>3</sup> was employed to increase accessibility to the inner chamber in the lower tank. The Aquarium can be easily re-positioned since it sits on an air-pad frame. The inner chamber (400 mm × 400 mm × 280 mm) houses the neutron source (see Fig. 2.2) and up to 4 YAP detectors (see Section 4.1). PMMA sleeves (see Fig. 2.2) are used to set the YAP detectors in well-defined positions. These sleeves are inserted through designated openings 30 mm in diameter and 480 mm in length. A fifth slightly smaller vertical penetration (26 mm in diameter) for the source is located in the geometrical center of the Aquarium. The Aquarium is filled with ~ 2650 liters of ultra pure, de-ionized water. Four beamports 172 mm (diameter) and 500 mm (length) allow for four simultaneous, independent irradiations.

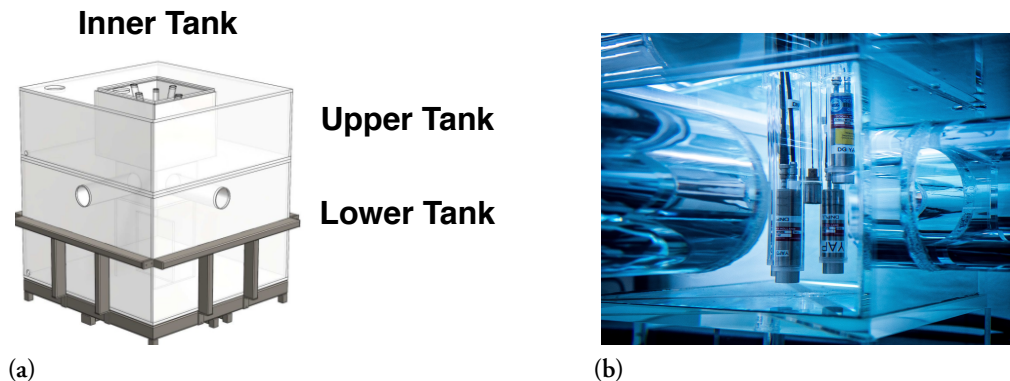


**Figure 2.2:** The Aquarium. (a) 3-D schematic drawing of the Aquarium, made up of the lower tank, the upper tank and the inner tank. The air-pad frame is also shown. (b) A photograph of the inner chamber. The 4 YAP detectors and the sleeves holding them in position are clearly visible.

<sup>2</sup>The gamma-ray and neutron dose rates have been measured with a FH 40 G-10 gamma-ray dosimeter and a FHT 752 neutron dosimeter from Thermo Fischer.

<sup>3</sup>The detailed CAD drawings were provided by Håkan Svensson of the MAX IV Laboratory.

## 4 Detectors

Four different kinds of radiation, gamma-rays, neutrons, alpha-particles and heavy ions, were investigated with the detectors presented here.

### 4.1 The YAP Scintillator Detector



Figure 2.3: Photograph of a YAP detector. The PMT and the PMT assembly (base and magnetic shielding) are located on the polished side to the left. The YAP crystal is located under the matt surface to the right.

YAP:Ce detectors (Ce<sup>+</sup> doped yttrium aluminum perovskite) were used to measure the 4.44 MeV gamma-rays from the first excited state of <sup>12</sup>C. YAP is an excellent choice for a gamma-ray detector operated near an intense neutron source. The material is radiation hard and is quite (but not completely) insensitive to neutrons. YAP is a mechanically and chemically resistant, single-crystal scintillator with a relative low effective  $Z \sim 31.4$ . The material has a fast risetime ( $\sim 5$  ns) and a short decaytime ( $\sim 27$  ns) which allows for fast timing information and high count rates. The 1 inch high and 1 inch diameter single crystal is coupled to a 1 inch PMT. The PMTs are operated at about  $-800$  V. The energy resolution was determined to be  $\sim 10\%$  at 662 keV determined using <sup>137</sup>Cs. The YAP detectors are not used for spectroscopy but rather as trigger detectors.

### 4.2 The CeBr<sub>3</sub> Scintillator Detector

A Cerium(III)bromide (CeBr<sub>3</sub>) scintillator detector was used to measure the gamma-ray field of actinide/Be sources. CeBr<sub>3</sub> is a relative new, hygroscopic, single-crystal detector material that has an excellent energy resolution of  $\sim 3.8\%$  at 662 keV using



Figure 2.4: Photograph of the  $\text{CeBr}_3$  detector. The scintillator crystal is to the left. The PMT and the base are to the right.

$^{137}\text{Cs}$ . The material also has a low intrinsic activity and the measured spectrum is not disturbed by naturally occurring radioactive decays in the detector material. This makes  $\text{CeBr}_3$  superior to other high-resolution scintillator materials which often suffer from intrinsic activity [47]. The 1.5 inch high and 1.5 inch diameter single crystal is coupled to a 2 inch PMT. The PMT was operated at about  $-850\text{ V}$ .

### 4.3 The Liquid Scintillator Detectors

Three liquid-scintillator detectors were constructed. The detectors are sensitive to both gamma-rays and fast-neutrons. An assembled fast-neutron detector is shown in Fig. 2.5. Each of the detectors consisted of a 3 mm thick aluminum cell with a 94 mm inner diameter and a 62 mm inner depth filled with  $\sim 430\text{ ml}$  of NE-213 [48], EJ-305 [49] and EJ-331 [50], respectively. NE-213 is a commonly used liquid organic scintillator for fast-neutron detection based on xylene<sup>4</sup>, an aromatic molecule of the formula  $\text{C}_6\text{H}_4(\text{CH}_3)_2$ . The scintillator emits light at 425 nm and has a bulk light-attenuation length of  $\sim 3\text{ m}$ . EJ-305 and EJ-331 are both based on 1,2,4-trimethylbenzene, also known as pseudocumene, an aromatic molecule of the formula  $\text{C}_6\text{H}_3(\text{CH}_3)_3$ .

The cells were sealed with 5 mm thick borosilicate glass windows [51] using Araldite 2000+ [52] glue which is highly resistant to both high temperature and chemicals. Borosilicate glass is a good choice to couple the scintillator cell to the PMT since the

<sup>4</sup>Newer versions are based on pseudocumene which is both less toxic and less flammable than xylene.

refractive index of the scintillator ( $\sim 1.505$ ) and the refractive index the glass window ( $\sim 1.517$ ) are close to each other. Two penetrations sealed by M8 threaded aluminum screws with 20 mm diameter heads and 14 mm diameter Viton O-rings [53] were used to fill the detectors. The inner walls of the detectors were painted with the reflective paint EJ-520 [54] to increase the amount of light guided to the PMT photo-cathode. This paint is able to withstand the highly aggressive solvents in the scintillators. The scintillators were flushed with nitrogen before they were transferred to the detector cells. Nitrogen flushing is a common method to reduce the oxygen content in liquid scintillators. Oxygen is known to negatively affect the scintillation properties of organic scintillators over time [30]. In addition, a nitrogen-transfer system was used to fill the cells.



Figure 2.5: A photograph of an assembled liquid-scintillator detector. The black tube attached to the detector cell is a magnetically shielded 3 inch ET Enterprises 9821KB PMT assembly.

The filled cells were coupled to 72.5 mm (diameter)  $\times$  34 mm (length) PMMA lightguides. Acrylic PMMA transmits light down to wavelengths of 300 nm [55] and has a refractive index of  $\sim 1.491$ . The walls of the lightguides were painted with water-soluble EJ-510 [56] reflective paint. The lightguides were pressure-coupled to spring-loaded, magnetically shielded 3 inch ET Enterprises 9821KB PMT assemblies [38] operated at about -2000 V. To ensure that the behavior of the detectors is stable over an extended period of time, no optical grease was used in the assembly.

#### 4.4 The $^4\text{He}$ -based Neutron Diagnostic Tool

A short version neutron diagnostic tool (NDT) from Arktis Radiation Detectors [57] (Arktis) is shown in Fig. 2.6. The pressure vessel, a stainless-steel tube with an outer diameter of 5.08 cm and an active length of 19.5 cm, was sealed on both ends with optical windows.  $^4\text{He}$  was filled into the active detector volume to a pressure of

120 bar. This high pressure is necessary to achieve an acceptable neutron-detection efficiency [57]. The interior surface of the stainless-steel cylinder was coated with a PTFE-based diffuse reflector [58] which was itself coated with an organic phosphor that converted the wavelength of the scintillation light from 80 nm to 430 nm. Signal loss in the detector was almost exclusively due to multiple reflections inside the detector. Light losses due to re-absorption in the detector medium were negligible, since  $^4\text{He}$  is essentially transparent to its own scintillation light [59]. The scintillation pulses were read out via both optical windows by dry-fitted Hamamatsu R580 [60] PMTs.



Figure 2.6: A picture of the NDT pressurized  $^4\text{He}$  noble-gas fast-neutron detector. The outer diameter was 5.08 cm and the active length was 19.5 cm.

## 4.5 The $^4\text{He}$ Fission-Fragment Detector

The  $^4\text{He}$  noble-gas scintillator detector<sup>5</sup> used to detect the  $^{252}\text{Cf}$  fission fragments is shown in Fig. 2.7. The cell was machined from a solid block of aluminum. The inner cylindrical volume  $\sim 72\text{ mm} \times 58\text{ mm}$  (diameter) is  $\sim 350\text{ ml}$ . The inner cell was sandblasted and painted with water soluble EJ-510 [56] reflective paint. A fused-silica optical window is pressed against the cell and allows the scintillation light to escape. The gas mixture was chosen to be 5 bar  $^4\text{He}$  (99.99999% pure) and 2.5 mbar (500 ppm) nitrogen (99.99999% pure) which was used as a wavelength shifter. The gas mixture is 24 times less dense than in the Arktis NDT detector that was introduced in Sec. 4.4. The neutron-detection efficiency of the cell is therefore about 4% of that of the NDT. A 2 inch XP2262Q PMT from Photonis [62] is coupled with optical grease (EJ-550 [63]) to the optical window. The PMT was operated at -1750 V.

<sup>5</sup>The detector is an active target prototype that was developed and built at the University of Glasgow [61].



Figure 2.7: A picture of the  $^4\text{He}$  fission fragment detector. From left to right, a high pressure valve, the aluminum pressure vessel and the PMT assembly with a black mu-metal shield are shown.

## 5 Data Acquisition and Electronics

The data-acquisition system used for this work<sup>6</sup> was continuously improved upon during the last five years. However, the general layout was kept the same. Signals were recorded on an event-by-event basis for offline analysis using a LINUX PC DAQ system. The DAQ uses the C++ based data-analysis framework ROOT [64] to provide online data monitoring and data storage. The analog signals from the liquid-scintillator detectors, the YAP detectors, the  $\text{CeBr}_3$  and the  $^4\text{He}$  fission detector were passed to long-gated (LG) charge-to-digital converters (QDCs) with integration gates of 500 ns and to short-gated (SG) QDCs with integration gates of 60 ns. The gates were opened  $\sim 25$  ns before the analog pulses arrived. The analog signals were also passed to constant fraction (timing) discriminators (CFDs). The logic signals from the discriminators were passed to digital scalers and time-to-digital converters (TDCs). The VME and CAMAC crates containing the QDCs, TDCs and scalers were connected to the PC by a PCI-VME bus adapter and CAMAC branch drivers (CBDs). The DAQ was triggered for the distant detector, NE-213 and  $\text{CeBr}_3$ , if actinide/Be sources were used. For the measurement with the  $^{252}\text{Cf}$  source the trigger was provided by the fission-fragment detector. The modules used in this work are listed in Table 2.2.

<sup>6</sup>The data in PAPER II were taken with the commercial WaveDREAM-B16 digitizer that was supplied by Arktis Radiation Detectors. All other data were taken with the DAQ described in the text.

Table 2.2: An overview of the electronic modules used in the experiments.

Type	Module Name	Manufacture	Standard
CFD	PS 715	Phillips Scientific	NIM
CFD	Ortec 935	Ortec	NIM
SG QDC	LRS 2249A	LeCroy	CAMAC
SG QDC	V792	CAEN	VME
LG QDC	LRS 2249W	LeCroy	CAMAC
LG QDC	V792	CAEN	VME
TDC	LRS 2228A	LeCroy	CAMAC
TDC	V1190B-2eSST	CAEN	VME
Scaler	LRS 4434	LeCroy	CAMAC
Scaler	V830	CAEN	VME
PCI-VME adapter	SIS3100	Struck	Optical Fiber Connection
PCI-VME adapter	SBS616	SBS Technologies	Copper Cable Connection
CBD	CES 8210	Creative Electronic Systems	VME

## 6 Experimental Configuration

Three different experimental configurations were used in this work: the free irradiation configuration, the “tagged” fast-neutron configuration and the  $^{252}\text{Cf}$  configuration. The NE-213 detector was irradiated in all three configurations. The  $\text{CeBr}_3$  used to measure the gamma-ray field was freely irradiated. The fission fragments were detected with a  $^4\text{He}$  detector (see Sec. 4.5).

A block diagram of the tagged-neutron configuration is shown in Fig. 2.8. The actinide/Be sources were placed in the inner chamber of the Aquarium so that their cylindrical-symmetry axes corresponded to the vertical direction in the lab. A 3 mm thick cylindrical Pb sleeve (with the same orientation) could be placed to attenuate the associated 60 keV gamma-rays from the Am/Be source, if desired. The YAP detectors were placed with their crystals approximately 10 cm from the actinide/Be sources. The crystal orientation of the YAPs was such that their cylindrical symmetry axis also corresponded to the vertical direction in the lab. These detectors triggered overwhelmingly on the 4.44 MeV gamma-rays radiating from the source which came from the decay of the first excited state of  $^{12}\text{C}$ . The NE-213 cell was placed 0.5 m - 2.5 m from the actinide/Be sources at source height and was free-running. The NE-213 detector detected both neutrons and gamma-rays.

A block diagram of the  $^{252}\text{Cf}$  configuration is shown in Fig. 2.9. The  $^{252}\text{Cf}$  source was placed inside the  $^4\text{He}$  detector. The  $^4\text{He}$  detector triggered overwhelmingly on the



## 7 Calibration of Liquid-Scintillator Detectors

Gamma-ray sources are used to calibrate organic scintillators since the light yield of the recoiling atomic electrons is linear above  $\sim 100$  keV [30, 65].

However, the low  $Z$  value of liquid scintillators means that gamma-rays interact mainly by Compton scattering and no well-defined photo-peaks are visible in the pulse-height spectra. To calibrate the NE-213 liquid scintillator detector, resolution-broadened Compton edges have to be interpreted carefully. Knox and Miller [65] and Flynn *et al.* [66] have reported on two different prescriptions to extract the Compton edge from a resolution-smear distribution. However, no clear consensus on which is the more precise method exists so the exact location of the Compton edge must be determined with the aid of a Monte Carlo simulation [67, 68, 69, 70]. The maximum energy transfer  $E_{CE}$  of a gamma-ray by Compton scattering can be calculated using:

$$E_{CE} = \frac{2E_\gamma^2}{m_e + 2E_\gamma}, \quad (2.1)$$

where  $m_e$  is the electron rest mass and  $E_\gamma$  is the incident gamma-ray energy.

Knox and Miller predicted that the Compton-edge energy  $E_{CE}$  should be located at roughly 89%<sup>7</sup> of the full height of the resolution-broadened Compton-edge distribution, and the energy of the recoil electrons at this point should be the maximum transferred energy given by Eq. 2.1. The method suggested by Flynn *et al.* places the Compton edge at 50%<sup>8</sup> of the full height of the resolution-broadened Compton edge, and the energy of the recoil electrons should be about 4% above the maximum transferred energy given by Eq. 2.1. The gamma-ray energies  $E_\gamma$ , the Compton-edge energy  $E_{CE}$  and the energy at  $1.04 \times E_{CE}$  are shown in Table 2.3.

The QDC spectrum of a  $^{22}\text{Na}$  gamma-ray source is shown in shown in Fig. 2.10. The edge location as predicted for both methods are indicated by blue arrows for the Knox and Miller method and by black arrows for the Flynn *et al.* method. The pedestal peak corresponds to the null value for the source energy spectrum and is clearly visible at about channel 50.

<sup>7</sup>The position of the Compton-edge (Knox and Miller method) can be calculated as  $\mu + \frac{1}{2} \cdot \sigma$ , where  $\mu$  is the mean of the Gaussian fit and  $\sigma$  the standard deviation.

<sup>8</sup>The position of the Compton edge (Flynn *et al.* method) can be calculated as  $\mu + \sqrt{2\ln 2} \cdot \sigma$ , where  $\mu$  is the mean of the Gaussian fit and  $\sigma$  the standard deviation.

Table 2.3: The gamma-ray energies of  $^{22}\text{Na}$  and  $^{137}\text{Cs}$ , the energies of the Compton edges and the energies at the half-height position as described by Flynn *et al.* [66].

Source	$E_\gamma$ [MeV]	$E_{CE}$ [MeV]	$1.04E_{CE}$ [MeV]
$^{22}\text{Na}$	0.511	0.341	0.354
	1.274	1.061	1.104
$^{137}\text{Cs}$	0.662	0.478	0.497

To calibrate the NE-213 detector, the locations of the Compton edges in QDC channels which were determined by the Knox and Miller and Flynn *et al.* methods, are correlated with calculated values in Table 2.3. Figure 2.11 shows the resulting calibration curves. A clear discrepancy between both calibrations is visible and it follows that a Monte Carlo simulation is necessary to decide which method is best.

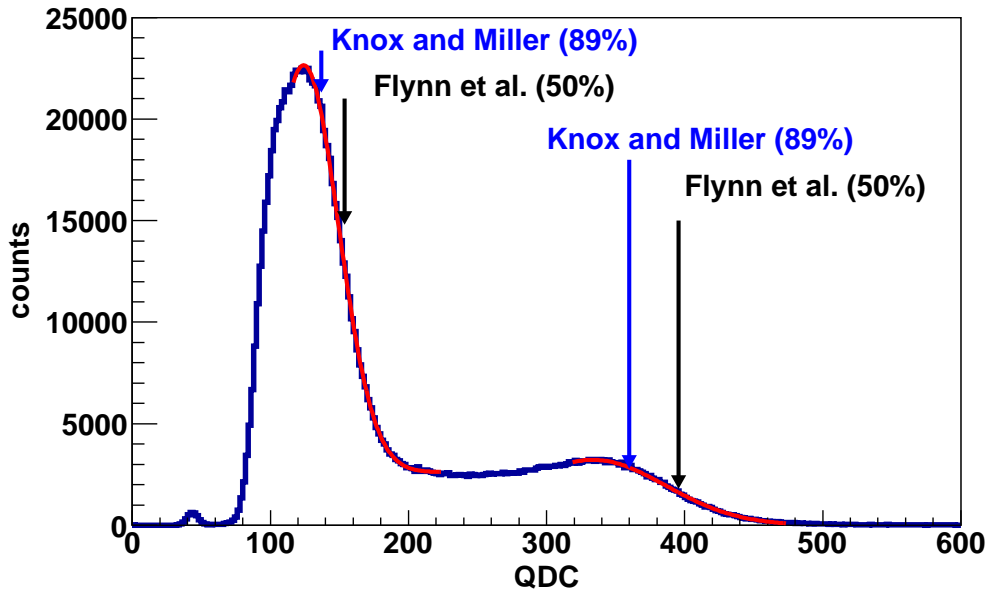


Figure 2.10: The  $^{22}\text{Na}$  gamma-ray spectrum of a NE-213 liquid scintillator detector. The location of the Compton edge according to Knox and Miller [65] is indicated by the blue arrows. The black arrows indicate the position of  $1.04E_{CE}$  as suggested by Flynn *et al.* [66].

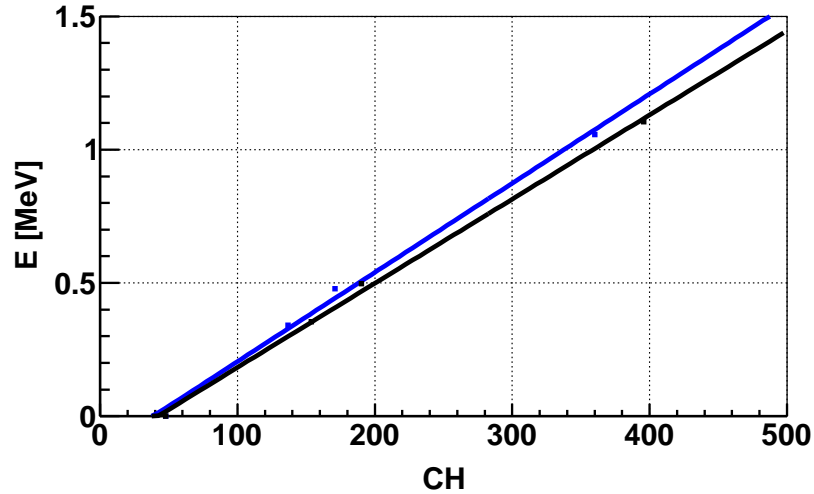


Figure 2.11: The gamma-ray energy calibration of the NE-213 liquid scintillator detector.

The gamma-ray calibration methods were validated with a GEANT 4 [71] simulation of the NE-213 detector. Figure 2.12 shows the measured  $^{22}\text{Na}$  gamma-ray spectrum (black dots), the simulated energy deposition (blue) and the simulated resolution-broadened detector response (red).

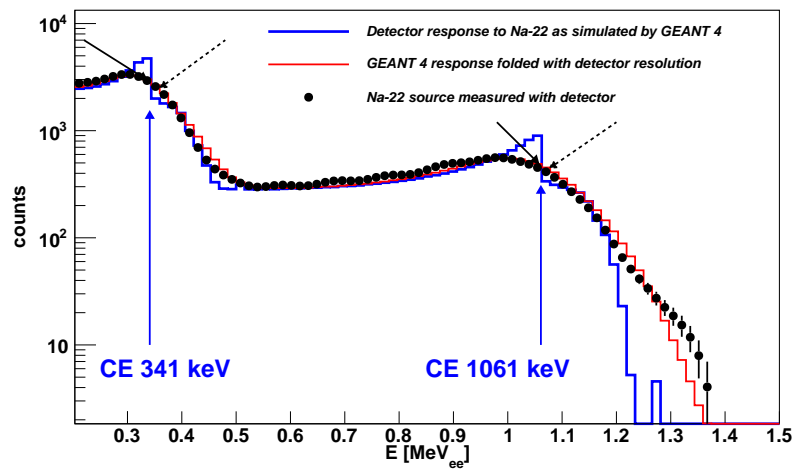


Figure 2.12: The gamma-ray spectrum of a  $^{22}\text{Na}$  source measured with the NE-213 detector and the GEANT 4 simulation of the detector response. The full arrows indicate the positions of the Compton edges according to Knox and Miller and the dashed arrows indicate the positions of the Compton edges according to Flynn *et al.*

The blue arrows indicate the positions of the Compton-edges at 341 keV and at 1061 keV. If the simulation is compared to these Compton edge prescriptions, the the Knox and Miller approach underpredicts systematically the locations of the Compton edges by less than 3% and Flynn *et al.* approach overpredicts systematically the locations of the Compton edges by more than 10%. The Knox and Miller approach corrected by 3% was therefore used to calibrate the NE-213 detector.

## 8 Pulse Shape Discrimination

The different shapes of the light pulses from gamma-ray-induced recoiling electrons and from neutron-induced recoiling protons were measured using the “Tail-to-Total” Charge Comparison Method [72, 73, 74] (see Fig.2.13). This method compares the delayed light (tail) of a scintillation pulse to the total light amount of a scintillation pulse produced by the incident radiation.

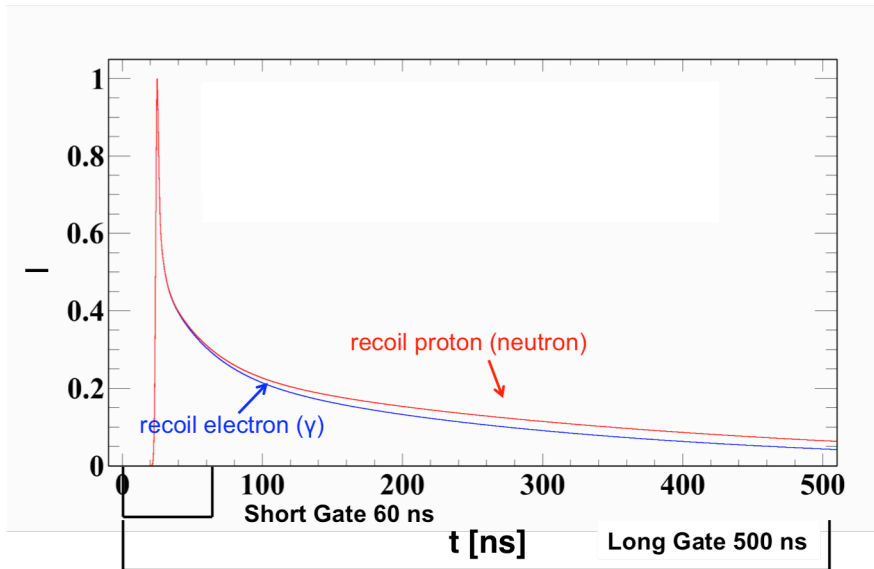


Figure 2.13: An illustration of the difference in the pulse shape of a neutron-induced recoiling proton (red) and a gamma-ray induced recoiling electron (blue) .

The pulse-shape function  $PS$  is defined to measure the ratio between delayed scintillation light and the total light pulse and uses the difference of the charge measured by the  $LG$  QDC (500 ns) and the  $SG$  QDC (60 ns) normalized to the  $LG$  QDC charge

$$PS = \frac{LG\ QDC - SG\ QDC}{LG\ QDC}. \quad (2.2)$$

The Figure-of-Merit (FOM), a value indicating the discrimination strength of a PSD technique, is a useful concept to measure the gamma-ray rejection strength of different scintillator materials and decide which is best. FOM are also useful if different discrimination techniques are to be tested with the same scintillator detector. The FOM is defined as

$$FOM = \frac{|m_n - m_\gamma|}{\delta_n + \delta_\gamma}. \quad (2.3)$$

An integrated PS spectrum ( $L \geq 0.58\ \text{MeV}_{ee}$ ) is shown in Fig.2.14. Two peaks are clearly visible. Events below  $PS = 0.2$  correspond to gamma-ray induced recoiling electrons. Events above  $PS = 0.2$  correspond to neutron-induced recoiling protons. The FWHMs of the Gaussian fits  $\delta_{n,\gamma}$  and the positions of the means  $m_{n,\gamma}$  are used to calculate the  $FOM = 1.03$  of the detector for a  $0.58\ \text{MeV}_{ee}$  pulse-height threshold cut.

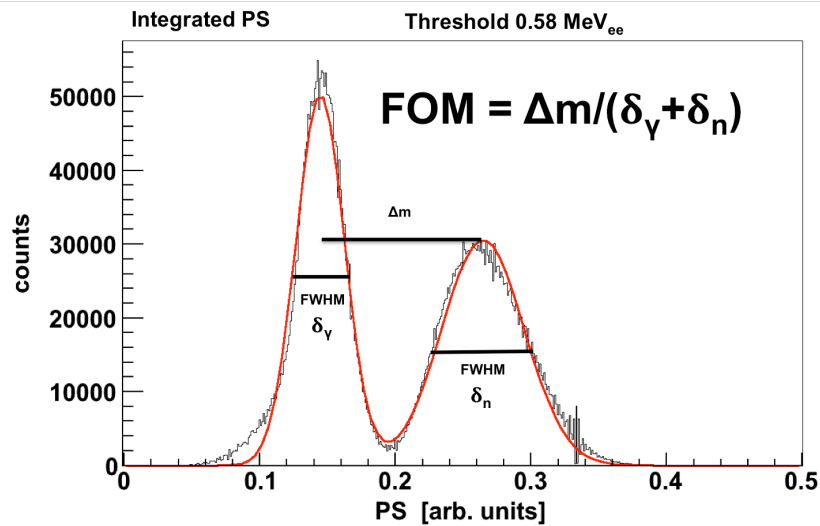


Figure 2.14: An integrated PS plot for all light yields larger than  $0.58\ \text{MeV}_{ee}$  is shown as an example of a FOM.

The FOM of the detector is a number strongly correlated to the integration threshold. The higher the threshold value, the better the discrimination and the larger the FOM.

Figure 2.15 shows a contour plot of  $PS$  plotted against the light yield  $L$  for the NE-213 detector.

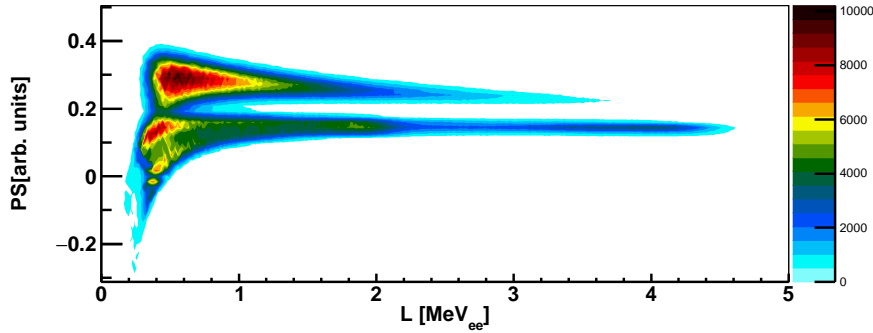


Figure 2.15: Contour plot of  $PS$  versus light yield  $L$  in  $\text{MeV}_{ee}$ .

The excellent discrimination between neutron and gamma-ray events is apparent for  $L > 0.5 \text{ MeV}_{ee}$ . A small overlap exists between the two distributions below this threshold in the vicinity of  $PS = 0.2$ . Gamma-rays events can be discriminated against by setting a  $PS$  threshold to about 0.2 so that only neutron like events will be processed further.

## 9 Energy-Tagged Fast-Neutrons and Time-of-Flight

A major part of the work presented in this thesis is based on coincidence measurements either between the products of the nuclear reaction  ${}^9\text{Be}(\alpha, n\gamma){}^{12}\text{C}$  in actinide/Be sources (see Chap. 1 Sec. 1.1) or between fission fragments and neutrons from the spontaneous fission of  ${}^{252}\text{Cf}$  (see Chap. 1 Sec. 1.2). Neutrons detected in these types of coincidence measurements have a well-defined reference to the time of the reaction  $T_0$ . They are thus tagged and their energy can be determined from their time-of-flight  $TOF_n$  and their flight path  $s$ .

The tagging setup used to measure  $TOF_n$  is illustrated in Fig. 2.16. The flight-path from the source to the NE-213 detector  $s$ , the point where the nuclear reaction occurs at the time  $T_0$ , and the time-of-flight of the gamma-rays to the NE-213 detector ( $TOF_\gamma$ ), of the neutrons to the NE-213 detector ( $TOF_n$ ) and of the gamma-rays to a YAP detector ( $t_{\text{YAP},\gamma}$ ) are all illustrated. The CFDs, the delay of the YAP signals

and the TDC are also shown. The TDC measures the time difference between the arrival of a start signal and the arrival of a stop signal.

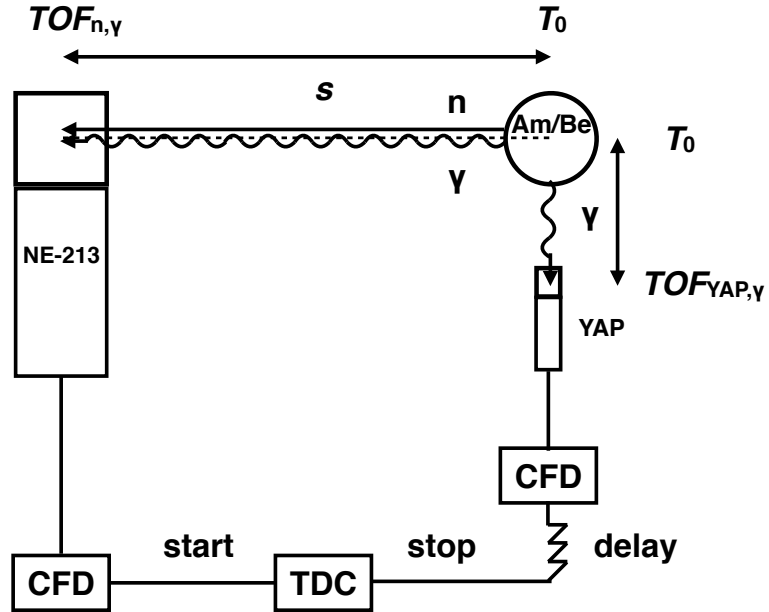


Figure 2.16: A schematic illustration of a TOF measurement.

The experiment shown in Fig. 2.16 does not measure the TOF direct. Instead, the time difference between the arrival of the start signal from the liquid-scintillator detector and the arrival of the stop signal from the YAP detector is measured. The absolute TDC values of a gamma-ray/gamma-ray coincidence ( $t'_{\gamma,\gamma}$ ) and a neutron/gamma-ray ( $t'_{n,\gamma}$ ) coincidence are thus influenced by the experimental setup and will change for example if the length of the cable connecting one of the detector to the DAQ is changed. However, the time difference between the two events  $|t'_{\gamma,\gamma} - t'_{n,\gamma}|$  will not change. This fixed difference is used to calculate the neutron  $TOF_n$ :

$$TOF_n = |t'_{\gamma,\gamma} - t'_{n,\gamma}| + TOF_{\gamma}, \quad (2.4)$$

where the  $TOF_{\gamma}$ , the gamma-ray TOF, can be calculated from the speed of light  $c$  and the flight-path  $s$ . The actinide/Be sources produce two prompt regions in the TDC spectrum: one from gamma-ray/gamma-ray coincidences and the other

from neutron/gamma-ray coincidences. The neutron/gamma-ray region is the result of a gamma-ray detected in the YAP detector and a neutron detected in the liquid-scintillator detector. The prompt neutron/gamma-ray distribution is wide and structured, since neutrons corresponding to the first-excited state in  $^{12}\text{C}$  are emitted with a wide range of energies. The gamma-ray/gamma-ray region is produced by the simultaneous detection of a gamma-ray in the NE-213 detector and a correlated gamma-ray in the YAP detector. The gamma-ray/gamma-ray coincidence produces a narrow peak called the gamma-flash. The gamma-flash position relative to  $T_0$  (when the reaction occurred) in the coincidence spectrum can be calculated from the flight-path  $s$  and the TDC time resolution ( $250 \frac{\text{ps}}{\text{CH}}$ ). The neutron region populates lower coincidence TDC channels, while the gamma-ray/gamma-ray region is at higher TDC channels. This is due to the delay of the YAP signal. The time between a start signal coming from a neutron detected in the NE-213 detector and the stop signal from a gamma-ray detected by the YAP detector is indicated by  $t'_{n,\gamma}$ . The time between a start signal arising from a gamma-ray in the NE-213 and a stop signal from a gamma-ray detected in the YAP is shown as  $t'_{\gamma,\gamma}$ .

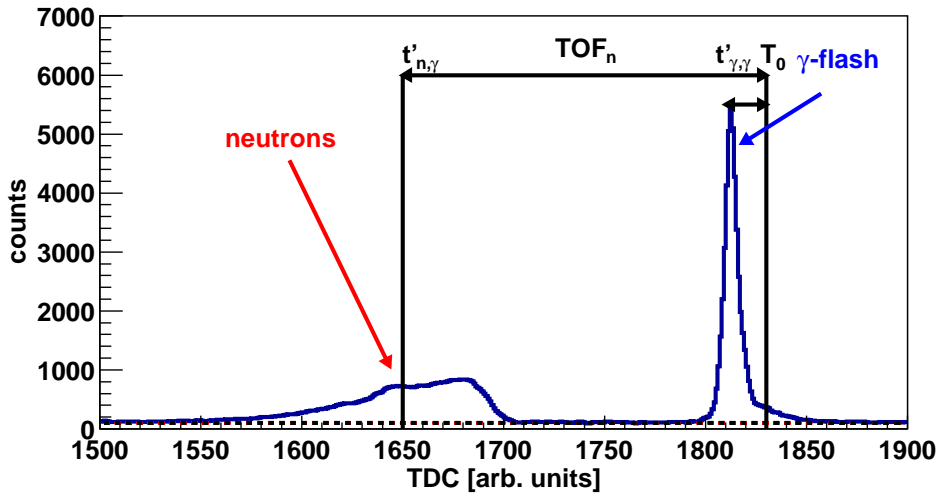


Figure 2.17: The measured TDC coincidence spectrum between particles detected in the NE-213 and particles detected in a YAP detector. A TDC entry represents the time between the arrival of the start signal from the NE-213 detector and the arrival of the stop signal from the YAP detector. The gamma-flash and the neutron region are indicated with a blue and a red arrow respectively.

The neutron TOF was transformed on an event-by-event base into neutron energy.

The kinetic energy was calculated according to:

$$T_n = \frac{1}{2} m_n c^2 \frac{s^2}{TOF_n^2 \cdot c^2} \quad (2.5)$$

where  $m_n$  is the neutron mass,  $s$  is the distance from the source to the detector,  $TOF_n$  is the neutron  $TOF$  and  $c$  is the speed of light. Using the classical energy formula is acceptable in this work due to the low energies (<10 MeV) involved.

Figure 2.18 shows the energy spectra for tagged neutrons corresponding to the first excited state of  $^{12}\text{C}$  from the Am/Be source and from the  $^{238}\text{Pu}$ /Be source. Both spectra are shown with previous measurements of the full-neutron spectra. The ISO standard neutron spectrum for Am/Be sources is also shown. It is clear that tagged neutron spectra and the previous measurements agree well in the region of interest (2 MeV - 6 MeV).

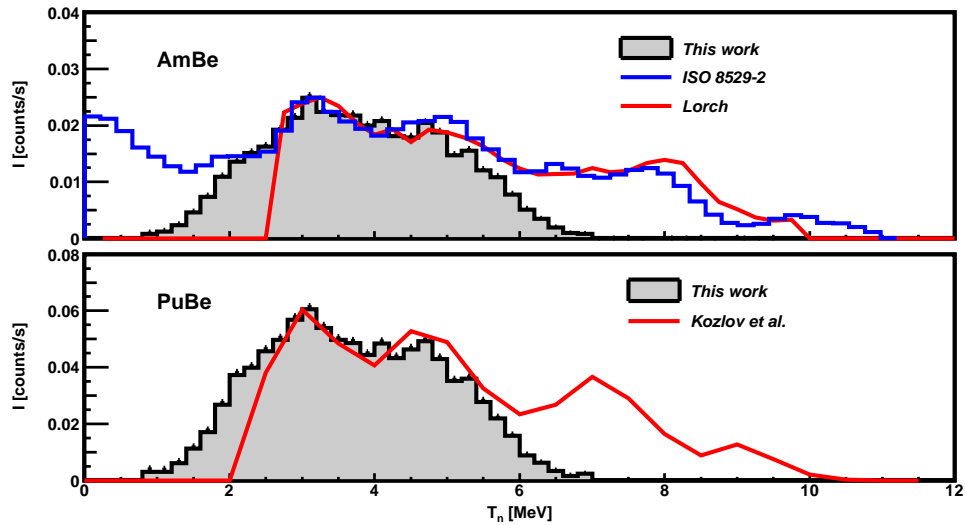


Figure 2.18: The tagged-neutron spectra together with the ISO 8529-2 reference spectrum and previous measurements. The gray-shaded histograms show the tagged-neutron spectra of the Am/Be and the Pu/Be sources. Note the different y-axis scales in the top and bottom panel. Previous measurements are also shown.

# Chapter 3

## Results

In this chapter, I summarize the five original articles this thesis is based on. The theme of my doctoral dissertation is neutron irradiation techniques.

**PAPER I: Development of the neutron tagging-technique** The neutron-tagging technique with actinide/Be sources was established. Fast-neutrons were energy-tagged by measuring the time-of-flight. From this, the neutron-energy spectrum was determined and compared to previous measurements and theoretical calculations. The agreement of the data with both was excellent in the region of interest between 2 - 6 MeV.

**PAPER II: Test of a commercial neutron detector against a liquid-scintillator detector using classic irradiation** The gamma-ray discrimination properties of a commercially developed neutron-diagnostic tool was bench-marked against a standard liquid-scintillator detector commonly used for fast-neutron detection. Threshold dependent figures-of-merit characterizing the detector pulse-shape discrimination strength were simultaneously established for both detectors. In the neutron-diagnostic tool, gamma-rays produced a maximum number of photons corresponding to about 750 keV<sub>ee</sub>. This enabled the use of pulse-height discrimination to suppress gamma-ray events. The neutron-diagnostic tool clearly outperformed the liquid-scintillator detector in the investigation.

**PAPER III: Detailed characterization of a liquid-scintillator detector using neutron tagging** Two proton light-yield parameterizations, two gamma-ray calibration methods, three different methods to determine the location of the neutron edge in a proton recoil-energy spectrum and two different scintillation-light integration times were tested. An extensive Monte Carlo simulation was used to validate the results.

**PAPER IV: Characterization of other actinide/Be neutron sources** The tagged neutron yield and the untagged gamma-ray yield of an Am/Be source and of a  $^{238}\text{Pu}/\text{Be}$  source were measured. It was not surprising that the shape of the tagged neutron spectra agreed well with each other, previous measurements and an ISO recommendation as the neutron production mechanism in both was essentially identical. The gamma-ray spectra of both sources were also similar to each other above 1 MeV and were clearly dominated by the 4.44 MeV gamma-rays from the de-excitation of the first-excited state of  $^{12}\text{C}$ .

**PAPER V: Extension of neutron-tagging techniques to  $^{252}\text{Cf}$  to facilitate studies of neutron-detection efficiency.** Fission-neutrons from a quasi-open  $^{252}\text{Cf}$  source were tagged. The corresponding fission fragments were detected in a noble-gas scintillator detector. The fission-neutrons and gamma-rays emitted by the source were detected in the previously characterized and now very well understood liquid-scintillator detector. As the fission neutron spectrum of  $^{252}\text{Cf}$  is very well-known, this technique will facilitate future studies of neutron-detection efficiency.

# Closing Remarks

In this thesis, I have presented source-based neutron-irradiation techniques useful for the characterization of neutron detectors. My work was centered upon the development of an energy-tagged fast-neutron test bed from first prototype to permanent installation. This test bed now offers a well-defined neutron beam. I have also extended the tagged-neutron technique to fission-fragments which potentially allows for neutron detection efficiency measurements. Here, the fission – neutrons of a quasi-open  $^{252}\text{Cf}$  source are detected in coincidence with the fission fragments escaping the source and being detected by a  $^4\text{He}$  scintillator detector. Furthermore, I have reported on the development of pulse-processing and particle-identification techniques for neutron-irradiation studies with and without energy-tagged fast-neutrons, providing in depth characterizations of both commercially available detectors as well as standard scintillators.

This thesis is part of an ongoing effort to build ESS. Key-infrastructure has been created and fundamental neutron-laboratory techniques have been established. My research was made possible by the generous support of the European Spallation Source ESS ERIC. A large number of my colleagues come from the ESS Neutron Technology Division, namely the Detector Group and the Neutron Optics and Shielding Group. They are interested in testing new detectors and shielding techniques, for both fast-neutron and gamma-ray responses. With the commissioning phase of the neutron detectors of the ESS approaching rapidly, I see the importance of the test bed in Lund increasing.

The test bed instruments have already attracted commercial interest from the Swiss company Arktis Radiation Detectors. They have used an Aquarium prototype to test one of their detectors and negotiations for further tests are ongoing. In addition, the test bed has been established as a popular place to educate students in radiation-

detection techniques. A large number of Bachelor and Master theses have been completed here and efforts are underway to create an irradiation lab for students. The vision is that even undergraduate students can use modern equipment for project work and laboratories side-by-side with professional researchers. I am proud to have been a part of these efforts.

Further goals include the measurement of neutron-detection efficiency using the fission-neutron tagging technique. In addition, shielding studies of novel shielding concretes for potential use at ESS have been conducted for some time now and publications are pending. An exciting project with a larger time frame is the plan to extend the energy-range of the tagged neutrons, towards thermal energies. This idea based on a triple-coincidence method exploiting active moderators, is under investigation. Simulation work has started.

I conclude my discussion of this thesis with some personal remarks. It has been an interesting five-year journey since I arrived in Lund and started with my research. In my time here, many changes have happened. The MAX IV Laboratory moved from its old location, less than 10 minutes on foot from the Department of Physics, to its new location in Brunnshög. The nuclear physics program at the MAX IV Laboratory (or MAX-lab as I used to know it) was still fully operational when I arrived, and I spent many long days in the nuclear “cave” setting up my experiments. However, it soon became clear that the MAX IV laboratory would discontinue its nuclear physics program and I refocused my work exclusively on developing neutron-irradiation techniques for detector characterizations. I was also able to witness the growth of the ESS from their original office space in downtown Lund to a full-fledged research organization. Along the way, I met colleagues who turned into friends and had the chance to see parts of Europe and North America. It was not always easy, often hard and at times frustrating. But with help and some stubbornness I managed to deliver a thesis that I am proud of and hope you enjoyed reading.

# Acknowledgements

Lund, Sweden

2016/11/22

The following acknowledgments are based, as are some other parts of this thesis, on the corresponding part in my Licentiate thesis. The increase of individuals and groups mentioned below is on one side the consequence of the developments that happened in Lund since my Licentiate defense, namely the establishment of the SoNnIG group in Lund; on the other side, it is the result of a more thorough reflection on people who supported me in the last 5 years. To those of you who recognize their acknowledgment from the last time I can only say thank you one more time, I feel as grateful for everything as the last time and appreciate all your help since even more.

At the start let me apologize. I most likely excluded a person/persons from these acknowledgments who supported me during the last couple of years or did me another kindness and deserved to be mentioned. This is neither intentional nor is it accidental, but simply unavoidable. I hope you may forgive me.

My first words of gratitude have to go to Dr. Kevin Fissum, my main supervisor. Kevin, thank you for everything. You supplied me with a great opportunity and I could not have done this without you. You always supported me, gave me guidance where needed and let me explore freely when appropriate. Thank you. My second thoughts go to Dr. Richard Hall-Wilton. Thank you Richard for your time and guidance. You had an open door for me, supported me and made time for me in your busy schedule. I hope you know how much I appreciated it. I want to say thank you to both Dr. John Annanad and Dr. Ramsey Al Jebali from the University of Glasgow. John, your help has been invaluable in many an endeavor from simulations to setting up the DAQ. Ramsey, thank you again for your support with the project and for all

the nice discussions about physics and life. I thank the European Spallation Source ESS ERIC for supplying a large part of the funding for my project, paying a large part of my salary, travel expenses and equipment. I want to say thank you to both the ESS Detector Group and the ESS Neutron Optics and Shielding Group. All of you have been helpful in one way or another over the last years. I thank the Photonuclear Group and the Radiation Safety Group at the MAX IV Laboratory for their support during the initial test "beamtimes" in the nuclear cave and for giving me access to their Am/Be source. A special thank you goes to Håkan Svensson. You supplied me with the technical drawings for both the water tank and the scintillator detector cells and turned vague ideas into reality. I want to thank all the people at the Division of Nuclear Physics for giving me a warm welcome and supporting me during my work. To my current and former office mates: Maciek, thank you for the great times talking, grilling or going out in Lund and in Gothenburg. Sandra, thank you for the nice talks and open ear. Ulrika, I hope you know how thankful I am to you. You helped keep me sane. Nathaly, thanks for all the nice fika times. To the members of the SoNnIG group, Hanno, Emil, Francesco and Nicholai, you have no idea how great it was to be finally part of a group. The help you gave me in the time you were in Lund was invaluable. Knowing that there was a person to ask for a hand gave me an incredible amount of comfort. I thank the Royal Physiographic Society in Lund for their support for new equipment to improve the DAQ system. And last but not least, I want to thank my family, my parents, Doris and Frank, and my siblings, Christoph, Lukas and Donata. I know I can always count on you.

Thank you,

Julius

# Bibliography

- [1] United States Committee on Army Science and Technology for Homeland Defense, Board on Army Science and Technology, Division on Engineering and Physical Sciences, National Research Council, Indications and Warning Technologies, in Science and Technology for Army Homeland Security: Report 1, National Academies Press (2003).
- [2] W.C. Lyons and G.J. Plisga. *Current practice in well logging, reservoir engineering and secondary recovery*. In: *The Petroleum Engineering Handbook: Sustainable Operations*. Gulf Publishing Company, 2013.
- [3] R. Chandra et al. *IEEE NSS/MIC*, page 508, 2010.
- [4] R. Chandra et al. *J. Instrum.*, 7:C03035, 2012.
- [5] M.R. Islam and M.I. Kahn. *Drilling and well completions, reservoir engineering*. In: *Standard Handbook of Petroleum and Natural Gas Engineering*. Gulf Publishing Company, 2011.
- [6] A. Tomanin et al. *Nucl. Inst. and Meth. A*, 756(0):45, 2014.
- [7] J. Walker. *Phys. Technol.*, 13:239, 1982.
- [8] A. Cho. *Science*, 326:778, 2009.
- [9] K. Zeitelhack. *Neutron News*, 23(4):10, 2012.
- [10] T.M. Persons and G. Aloise. *United States Government Accountability Office GAO-II-753*, 2011.
- [11] D. Kramer. *Physics Today*, 64:20, 2011.

- [12] R.T. Kouzes. *United States Government Accountability Office GAO-II-753*, 2011.
- [13] R. Hall-Wilton et al. *IEEE NSS/MIC*, page 4283, 2012.
- [14] O. Kirstein et al. *PoS (Vertex2014)*, page 29, 2014.
- [15] M Shoji et al. *J. Instrum.*, 7(05):C05003, 2012.
- [16] K. Andersen et al. *Nucl. Inst. and Meth. A*, 720(0):116, 2013.
- [17] C.L. Wang et al. *IEEE NSS/MIC*, page 4877, 2011.
- [18] D. Rezaei Ochbelagh, H. Miri Hakimabadb, and R. Izadi Najafabadib. *Nucl. Inst. and Meth. A*, 794:102, 2015.
- [19] [http://www3.nd.edu/~wzech/LabManual\\_0907c.pdf](http://www3.nd.edu/~wzech/LabManual_0907c.pdf).
- [20] A.A Naqvi et al. *Nucl. Inst. and Meth. A*, 353:156, 1994.
- [21] C.M. Frankle and G.E. Dale. *Nucl. Inst. and Meth. A*, 723:24, 2013.
- [22] J. Chadwick. *Nature*, 129:312, 1932.
- [23] I. El Agib and J. Csikai. *Nucl. Inst. and Meth. A*, 435:456, 1999.
- [24] Bulent Buyuk and A. Beril Tugrul. *Annals of Nuclear Energy*, 71:46, 2013.
- [25] J. Bagi, L. Lakos, and C.T. Nguyen. *Nucl. Inst. and Meth. B*, 366:69, 2016.
- [26] B. Milenkovic, N. Stevanovic, D. Nikezic, and D. Kosuti. *Appl. Radiat. Isot.*, 90:225, 2014.
- [27] R.B.M. Sogbadji et al. *Appl. Radiat. Isot.*, 90:192, 2014.
- [28] C. Iliadis. *Nuclear Physics of Stars*. Wiley-VCH, 2007.
- [29] L. Van der Zwan. *Can. J. Phys.*, 46:1527, 1968.
- [30] G.F. Knoll. *Radiation Detection and Measurement*. John Wiley and Sons, 1989.
- [31] F.D. Becchetti et al. *Am. J. Phys.*, 81:112, 2013.
- [32] R. Capote et al. *Nuclear Data Sheets*, 131:1, 2016.

- [33] J.B. Birks. *The Theory and Practice of Scintillation Counting*. Pergamon Press, 1964.
- [34] W.R. Leo. *Techniques for Nuclear and Particle Physics Experiments*. Springer, 1994.
- [35] [http://www.eljentechnology.com/images/products/data\\_sheets/EJ-301\\_EJ-309.pdf](http://www.eljentechnology.com/images/products/data_sheets/EJ-301_EJ-309.pdf).
- [36] Teresa Marrodan Undagoitia. *Measurement of light emission in organic liquid scintillators and studies towards the search for proton decay in the future large-scale detector LENA*. PhD thesis, TU München, 2008.
- [37] Eljen Technologies produces the wavelength shifting paint EJ-298 <http://www.eljentechnology.com/index.php/products/wavelength-shifting-plastics/ej-298-ej-298g>.
- [38] ET Enterprise Ltd. <http://www.et-enterprises.com>.
- [39] <https://www-nds.iaea.org/exfor/endl.html>.
- [40] Supplied by High Tech Sources Limited, Unit 6, Moorbrook, Southmead, Industrial Estate, Didcot, Oxfordshire, Uk OX11 7HP; <http://www.hightechsource.co.uk/>. For details see <http://www.hightechsource.co.uk/Legacy/Resources/Americium-Berryliu.pdf>.
- [41] The Radichemical Centre Amersham , England, is today a subsidiary of GE Healthcare.
- [42] <http://www.ezag.com>.
- [43] The Lund Ion Beam Analysis Facility (LIBAF) is a university laboratory at Lund University for material analysis using protons, deuterium and helium <http://www.nuclear.lu.se/english/research/applied-nuclear-physics/libaf/>.
- [44] <http://www.fluka.org>.
- [45] <http://www.maxlab.lu.se>.
- [46] VINK AS. <http://www.vink.se>.

- [47] F.G.A. Quaratu et al. *Nucl. Inst. and Meth. A*, 729:596, 2013.
- [48] NE-213 is no longer produced. Eljen Technologies offers EJ-301 [http://www.eljentechnology.com/images/products/data\\_sheets/EJ-301\\_EJ-309.pdf](http://www.eljentechnology.com/images/products/data_sheets/EJ-301_EJ-309.pdf) while Saint Gobain offers BC-501 [http://www.crystals.saint-gobain.com/sites/imdf.crystals.com/files/documents/sgc-bc501-501a-519-data-sheet\\_69711.pdf](http://www.crystals.saint-gobain.com/sites/imdf.crystals.com/files/documents/sgc-bc501-501a-519-data-sheet_69711.pdf).
- [49] Eljen Technologies produces EJ-305 <http://www.ggg-tech.co.jp/maker/eljen/ej-305.html>.
- [50] Eljen Technologies offers EJ-331 <http://www.eljentechnology.com/index.php/products/liquid-scintillators/ej-331-ej-335>.
- [51] <http://www.us.schott.com/borofloat/english/index.html> for details. Supplied by Glasteknik i Emmaboda AB, Utvägen 6 SE-361 31 Emmaboda, Sweden.
- [52] <http://www.huntsman.com>.
- [53] Viton is a registered trademark of DuPont Performance Elastomers LLC.
- [54] <http://www.eljentechnology.com/index.php/products/paints/87-ej-520>.
- [55] <http://www.eljentechnology.com/index.php/products/pmma-a-uvt-material/102-light-guides> .
- [56] <http://www.eljentechnology.com/index.php/products/paints/87-ej-510>.
- [57] <http://www.arktis-detectors.com/>.
- [58] Polytetrafluoroethylene, also known as Teflon; [http://www2.dupont.com/Products/en\\_RU/Teflon\\_and\\_Tefzel\\_FLUOROPOLYMERS\\_en.html](http://www2.dupont.com/Products/en_RU/Teflon_and_Tefzel_FLUOROPOLYMERS_en.html).
- [59] D.N. McKinsey and otherse. *Nucl. Inst. and Meth. A*, 516(2-3):475, 2004.
- [60] Hamamatsu Photonics. <http://www.hamamatsu.com/us/en/R580.html>.
- [61] Ramsey Al Jebali. *Measurement of the  $\gamma$  +<sup>4</sup>He Total Photoabsorption Cross-Section using a Gas-Scintillator Active Targe*. PhD thesis, University of Glasgow, 2013.

- 
- [62] <https://my.et-enterprises.com/pdf/XP2262.pdf>.
- [63] [http://www.eljentechnology.com/images/products/data\\_sheets/EJ-550\\_EJ-552.pdf](http://www.eljentechnology.com/images/products/data_sheets/EJ-550_EJ-552.pdf).
- [64] <https://root.cern.ch>.
- [65] H.H. Knox and T.G. Miller. *Nucl. Inst. and Meth.*, 101:519, 1972.
- [66] K.F. Flynn et al. *Nucl. Inst. and Meth.*, 27:13, 1964.
- [67] L.E. Beghian et al. *Nucl. Inst. and Meth.*, 35:34, 1965.
- [68] G. Dietze and H. Klein. *Nucl. Inst. and Meth.*, 193:549, 1982.
- [69] F. Arneodo et al. *Nucl. Inst. and Meth. A*, 418:285, 1998.
- [70] C. Matei et al. *Nucl. Inst. and Meth. A*, 676:135, 1998.
- [71] <http://geant4.cern.ch/>.
- [72] A. Jhingan et al. *Nucl. Inst. and Meth. A*, 585(3):165, 2008.
- [73] A. Lavagno, G. Gervino, and C. Marino. *Nucl. Inst. and Meth. A*, 617(1-3):492, 2010.
- [74] I.A. Pawełczak et al. *Nucl. Inst. and Meth. A*, 711(0):21, 2013.



# Scientific Publications



# Chapter A

## Papers

### Paper I

#### Tagging fast neutrons from an $^{241}\text{Am}/^9\text{Be}$ source

In this paper, we described the neutron-tagging technique and the PSD technique for a NE-213 liquid-scintillator fast-neutron detector. We measured the YAP-facilitated tagged-neutron spectrum from an Am/Be source and compared our result to previously measured neutron spectra and theoretical calculations. I contributed to the paper by planning, preparing and conducting the experiment, which included the construction of the liquid-scintillator detector, the assembly of the experimental setup (in particular, the prototype shielding), the construction of the trigger logic, and the optimization of the DAQ for our measurement. I performed the data analysis and assisted with the writing of the article.

## Paper II

### **A first comparison of the responses of a $^4\text{He}$ -based fast-neutron detector and a NE-213 liquid-scintillator reference detector**

In this paper, we compared the PSD capabilities of the NE-213 liquid-scintillator detector presented in Paper I to a commercially developed  $^4\text{He}$  scintillator detector (NDT). As expected, the commercially developed  $^4\text{He}$  scintillator detector demonstrated gamma-ray suppression that was superior to the NE-213 detector using both PHD and PSD discrimination techniques. This reduced gamma-ray sensitivity compared to NE-213 makes the NDT an interesting neutron-diagnostic tool in high-intensity gamma-ray fields. I helped to plan, prepare and conduct the experiment. I assisted with the data analysis and the writing of the article.

## Paper III

### **The light-yield response of a NE-213 liquid-scintillator detector measured using 2 – 6 MeV tagged neutrons**

In this paper, we thoroughly investigated the properties of the NE-213 liquid-scintillator detector presented in Papers I and II using the neutron-tagging technique described in Paper I. We tested two common gamma-ray calibration procedures against a dedicated GEANT4 simulation. We measured the neutron-response function of NE-213 at several neutron energies, compared the prompt portion of the scintillation-light pulse to the delayed portion, and evaluated two well-established parametrizations predicting the proton scintillation-light yield of the detector. Dedicated GEANT4 simulations of the neutron response were also performed. I planned, prepared and conducted the experiment, wrote the detector simulation, and performed the data analysis. I played a leading role in writing the article.

## Paper IV

### **A comparison of untagged gamma-ray and tagged-neutron yields from $^{241}\text{AmBe}$ and $^{238}\text{PuBe}$ sources**

In this paper, we performed detailed measurements of the gamma-ray and fast-neutron yields of two actinide/Be ( $^{241}\text{Am/Be}$  and  $^{238}\text{Pu/B}$ ) sources in an effort to identify which, if either, could be considered a superior source of fast neutrons. The NE-213 liquid-scintillator detector presented in Papers I to III and a previously untested  $\text{CeBr}_3$  gamma-ray detector were employed. Tagged-neutron beams as described in Paper I were used. I planned, prepared and conducted the experiment. I performed the data analysis and led the effort to write the article

## Paper V

### **Tagging fast neutrons from a $^{252}\text{Cf}$ fission fragment source**

In this paper, we tagged the spontaneous-fission neutrons emitted by a thin-backed  $^{252}\text{Cf}$  source. We employed a gaseous  $^4\text{He}$  scintillator connected to a photomultiplier tube to detect the fission fragments and the NE-213 liquid-scintillator detector presented in Papers I to IV to detect the fast neutrons. To our knowledge, this type of measurement has never before been attempted using a fission-fragment detector based upon a light, scintillating noble gas. I planned, prepared and conducted the experiment. I performed the data analysis and led the effort to write the the article.



Paper I







Contents lists available at ScienceDirect

## Applied Radiation and Isotopes

journal homepage: [www.elsevier.com/locate/apradiso](http://www.elsevier.com/locate/apradiso)Tagging fast neutrons from an  $^{241}\text{Am}/^9\text{Be}$  source

J. Scherzinger<sup>a,b</sup>, J.R.M. Annand<sup>c</sup>, G. Davatz<sup>d</sup>, K.G. Fissum<sup>a,b,\*</sup>, U. Gendotti<sup>d</sup>,  
R. Hall-Wilton<sup>b,f</sup>, E. Håkansson<sup>a</sup>, R. Jebali<sup>d,1</sup>, K. Kanaki<sup>b</sup>, M. Lundin<sup>e</sup>, B. Nilsson<sup>b,e</sup>,  
A. Rosborge<sup>e</sup>, H. Svensson<sup>e,g</sup>

<sup>a</sup> Division of Nuclear Physics, Lund University, SE-221 00 Lund, Sweden<sup>b</sup> Detector Group, European Spallation Source ESS AB, SE-221 00 Lund, Sweden<sup>c</sup> University of Glasgow, Glasgow G12 8QQ, Scotland, UK<sup>d</sup> Arktis Radiation Detectors Limited, 8045 Zürich, Switzerland<sup>e</sup> MAX IV Laboratory, Lund University, SE-221 00 Lund, Sweden<sup>f</sup> Mid-Sweden University, SE-851 70 Sundsvall, Sweden<sup>g</sup> Sweflo Engineering, SE-275 63 Blentarp, Sweden

## HIGHLIGHTS

- Neutrons emitted from a Be-compound source are tagged.
- The resulting beam of neutrons is continuous and polychromatic.
- The energy of each neutron is known.
- The approach is cost-effective.

## ARTICLE INFO

## Article history:

Received 15 September 2014

Received in revised form

30 December 2014

Accepted 5 January 2015

Available online 6 January 2015

## Keywords:

Americium–beryllium

Gamma-rays

Fast neutrons

Time-of-flight

## ABSTRACT

Shielding, coincidence, and time-of-flight measurement techniques are employed to tag fast neutrons emitted from an  $^{241}\text{Am}/^9\text{Be}$  source resulting in a continuous polychromatic energy-tagged beam of neutrons with energies up to 7 MeV. The measured energy structure of the beam agrees qualitatively with both previous measurements and theoretical calculations.

© 2015 Elsevier Ltd. Published by Elsevier Ltd. All rights reserved.

## 1. Introduction

Fast neutrons are important probes of matter and diagnostic tools (Walker, 1982; United States Committee on Army Science and Technology for Homeland Defense, 2003; <http://www.pos.sissa.it/cgi-bin/reader/conf.cgi?confid=25>; <http://www.hep.lu.se/staff/christiansen/proceeding.pdf>; <http://www.iopscience.iop.org/1748-0221/focus/extra.proc19>; Chandra et al., 2010, 2012; Lyons and Plisga, 2011; Peerani et al., 2012; <http://www.plone.ess.lu.se/>; Islam and Khan, 2013; Lewis et al., 2013, 2014; Tomanin et al., 2014). Sources of

fast neutrons for controlled irradiations include nuclear reactors, particle accelerators, and radioactive sources. Drawbacks associated with nuclear reactors and particle accelerators include their accessibility and availability, as well as the very high cost per neutron. In contrast, radioactive sources provide neutrons with a substantially lower cost per neutron. Drawbacks associated with radioactive sources include the complex mixed field of radioactive decay products which complicate the experimental situation. As a first step towards developing a source-based fast-neutron irradiation facility, we have employed well-understood shielding, coincidence, and time-of-flight (TOF) measurement techniques to attenuate and subsequently unfold the mixed decay-product radiation field provided by an  $^{241}\text{Am}/^9\text{Be}$  (hereafter referred to as Am/Be) source, resulting in a polychromatic energy-tagged neutron beam.

\* Corresponding author at: Division of Nuclear Physics, Lund University, SE-221 00 Lund, Sweden. Fax: +46 46 222 4709.

E-mail address: [kevin.fissum@nuclear.lu.se](mailto:kevin.fissum@nuclear.lu.se) (K.G. Fissum).

<sup>1</sup> Present address: University of Glasgow, Glasgow G12 8QQ, Scotland, UK.

## 2. Apparatus

### 2.1. Am/Be source

The heart of the irradiation facility consists of a (nominal) 18.5 GBq Am/Be radioactive source (<https://www.hightechsource.co.uk/>). This source is a mixture of americium oxide and beryllium metal contained in an X.3 capsule<sup>2</sup> (see Fig. 1).

Radioactive <sup>241</sup>Am has a half-life of 432.2 years and decays via  $\alpha$  emission (five different energies averaging  $\sim 5.5$  MeV) to <sup>237</sup>Np. The dominant energy of the resulting background gamma-rays from the decay of the intermediate excited states in <sup>237</sup>Np is  $\sim 60$  keV. <sup>237</sup>Np has a half-life of over 2 million years. <sup>9</sup>Be is stable.

Fast neutrons are produced when the decay  $\alpha$  particles interact with <sup>9</sup>Be. Depending on the interaction and its kinematics, <sup>12</sup>C and a free neutron may be produced. The resulting free-neutron distribution has a maximum value of about 11 MeV and a sub-structure of peaks whose energies and relative intensities vary depending upon the properties of the Am/Be source containment capsule and the size of the <sup>241</sup>AmO<sub>2</sub> and Be particles in the powders employed – see the detailed discussion presented in Lorch (1973). In general, approximately  $\sim 25\%$  of the neutrons emitted have an energy of less than  $\sim 1$  MeV with a mean energy of  $\sim 400$  keV (<https://www.hightechsource.co.uk/>). The average fast-neutron energy is  $\sim 4.5$  MeV. Both the gamma-ray and neutron dose rates at a distance of 1 m from our unshielded source in the X.3 capsule were measured to be 11  $\mu$ Sv/h, for a total unshielded dose rate of 22  $\mu$ Sv/h. The unshielded source has been independently determined to emit  $(1.106 \pm 0.015) \times 10^6$  neutrons per second nearly isotropically (National Physical Laboratory, 2012).

The kinematics and the reaction cross section for the <sup>9</sup>Be( $\alpha$ ,  $n$ ) interaction determine the state of the recoiling <sup>12</sup>C nucleus produced in the reaction. The calculations of Vijaya and Kumar (1973) (for example) suggest that the relative populations of the ground/first/second excited states for the recoiling <sup>12</sup>C nucleus are  $\sim 35\% / \sim 55\% / \sim 15\%$ . If the recoiling <sup>12</sup>C nucleus is left in its first excited state, it will promptly decay to the ground state via the isotropic emission of a 4.44 MeV gamma-ray. Mowlavi and Koohi-Fayegh (2004) as well as Liu et al. (2007) have measured  $R$ , the 4.44 MeV  $\gamma$ -ray to neutron ratio for Am/Be, to be approximately 0.58. Again, this is seemingly dependent upon the Am/Be capsule in question. Regardless, almost 60% of the neutrons emitted by an Am/Be source are accompanied by a prompt, time-correlated 4.44 MeV  $\gamma$ -ray. We exploit this property of the source to determine neutron TOF and thus kinetic energy by measuring the elapsed time between the detection of the 4.44 MeV  $\gamma$ -rays and the detection of the fast neutrons. Note that by employing this technique, we necessarily restrict our available “tagged” neutron energies to a maximum value of  $\sim 7$  MeV as 4.44 MeV of the reaction  $Q$ -value are “lost” to the de-excitation gamma-ray.

### 2.2. YAP:Ce 4.44 MeV gamma-ray trigger detectors

The 2 YAP:Ce<sup>3</sup> fast ( $\sim 5$  ns risetime) gamma-ray trigger detectors (hereafter referred to as YAPs) were provided by Scionix (<http://www.scionix.nl>). A detector (see Fig. 2) consisted of a cylindrical 1 in (diameter)  $\times$  1 in (height) YAP crystal (Moszyński et al., 1998) coupled to a 1 in Hamamatsu Type R1924 photomultiplier tube (PMT) (<http://www.hamamatsu.com>) operated at about  $-800$  V. Gains for the YAP detectors were set using a YAP

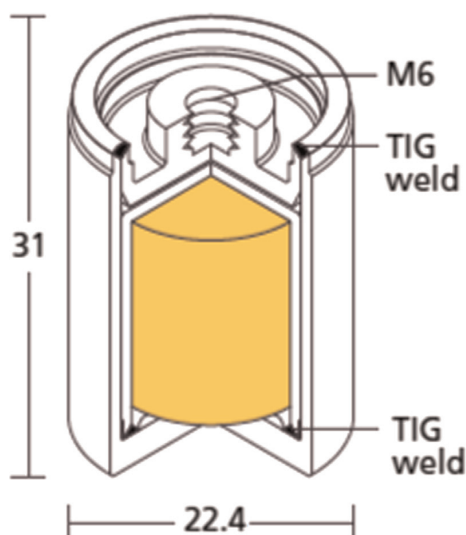


Fig. 1. The Am/Be source (figure from <https://www.hightechsource.co.uk/>). Dimensions in mm. The yellow shaded volume at the central core of the capsule corresponds to the Am/Be. (For interpretation of the references to color in this figure caption, the reader is referred to the web version of this article.)



Fig. 2. Photograph of a YAP detector. A 1 in (diameter)  $\times$  1 in (height) crystal has been mounted on a 1 in (diameter)  $\times$  10 cm (length) PMT.

event trigger and standard gamma-ray sources. Typical energy resolution obtained for the 662 keV peak of <sup>137</sup>Cs using such a detector was about 10%. YAP:Ce is radiation hard and quite insensitive to neutrons of all energies, which makes it ideal for detecting gamma-rays within the large fast-neutron field of the Am/Be source. We stress that because of their small volume, the YAP detectors were not used for spectroscopy, but simply to trigger on any portion of the energy deposited by the 4.44 MeV gamma-rays emitted by the source. A 3 mm thick Pb sleeve placed around the source (see Section 2.4) to attenuate the high intensity 60 keV gamma-ray field and a 350 keV<sub>ee</sub> discriminator threshold proved to be an effective combination for the YAP detection of these 4.44 MeV gamma-rays.

### 2.3. NE-213 fast-neutron and gamma-ray liquid-scintillator detector

The NE-213 fast-neutron and gamma-ray detector employed in this work is shown in Fig. 3. A 3 mm thick cylindrical aluminum cell with a depth of 62 mm and a diameter of 94 mm housed the NE-213. The inside of the cell was treated with xylene-solvent withstanding EJ-520 (<http://www.eljentechnology.com/index.php/products/paints/87-ej-520>) titanium dioxide reflective paint. The cell was sealed with a 5 mm thick borosilicate glass plate ([<sup>2</sup> An X.3 capsule is a tig-welded, double-layered, stainless-steel cylinder approximately 30 mm \(height\)  \$\times\$  22 mm \(diameter\).](http://</a></p>
</div>
<div data-bbox=)

<sup>3</sup> YAP:Ce stands for yttrium aluminum perovskite:cerium (YAlO<sub>3</sub>, Ce<sup>3+</sup> doped).



**Fig. 3.** CAD drawing of the NE-213 detector. Top panel: the detector. The large black cylinder to the right is the magnetically shielded 3 in ET Enterprises 9821KB photomultiplier-tube assembly. The small gray cylinder to the left contains the NE-213. Bottom panel: an enlargement of the small gray cylinder “cup”. The screws on top allow for the filling or draining of the liquid cylinder. A borosilicate-glass window (light brown) serves as the optical boundary. (For interpretation of the references to color in this figure caption, the reader is referred to the web version of this article.)

[www.us.schott.com/borofloat/english/index.html](http://www.us.schott.com/borofloat/english/index.html)) attached using Araldite 2000+ glue, which is highly resistant to both temperature and chemicals. The penetrations into the cell were closed with M-8 threaded aluminum plugs with 20 mm diameter heads and sealed with 14 mm diameter Viton O-rings. The assembled cell was filled with the nitrogen-flushed NE-213 using a nitrogen gas-transfer system.

After the cell was filled, the borosilicate glass window was coupled to a cylindrical PMMA UVT lightguide with a height of 57 mm and a diameter of 72.5 mm. The lightguide wall was painted with water-soluble EJ-510 (<http://www.eljentechnology.com/index.php/products/paints/86-ej-510>) reflective paint. The lightguide was then pressure-coupled to a spring-loaded, magnetically shielded 3 in ET Enterprises 9821KB PMT assembly ([www.et-enterprises.com/files/file/Pmtbrochure11.pdf](http://www.et-enterprises.com/files/file/Pmtbrochure11.pdf)) operated at about  $-2000$  V. In order to ensure the reproducibility of the behavior of the detector over an extended period of time rather than maximize light transmission, optical grease was not used in the assembly. Gain for the NE-213 detector was set using an NE-213 detector event trigger and a set of standard gamma-ray sources together with the prescription of Knox and Miller (1972).

#### 2.4. Configuration

A block diagram of the experiment configuration is shown in Fig. 4. The Am/Be source was placed so that its cylindrical-symmetry axis corresponded to the vertical direction in the lab at the center of a 3 mm thick cylindrical Pb sleeve (with the same orientation) to attenuate the 60 keV gamma-rays associated with the decay of  $^{241}\text{Am}$ .<sup>4</sup> A YAP detector was placed with its crystal approximately 5 cm from the Am/Be source at source height. The crystal orientation was such that its cylindrical symmetry axis also

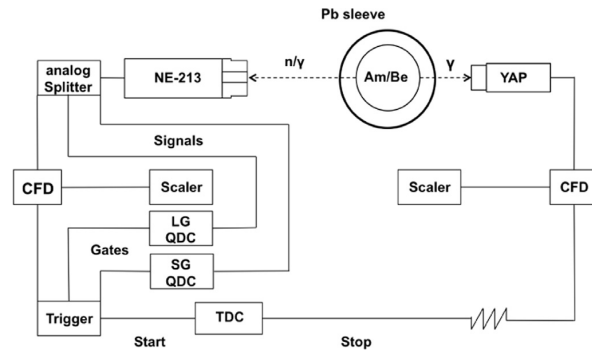


**Fig. 4.** A simplified overview of the experimental setup (not to scale). The Am/Be source, the Pb sleeve, a single YAP detector, and a NE-213 detector are all shown together with a block electronics diagram.

corresponded to the vertical direction in the lab. This detector triggered overwhelmingly on the 4.44 MeV gamma-rays radiating from the source which came from the decay of the first excited state of  $^{12}\text{C}$ . A NE-213 detector was placed approximately 68 cm from the Am/Be source at source height. The cylindrical symmetry axis of the NE-213 detector pointed directly at the center of the source. This detector triggered on both 4.44 MeV gamma-rays and fast neutrons coming from the source, as well as cosmic rays and room background.<sup>5</sup>

#### 2.5. Electronics and data acquisition

The analog signals from the YAP trigger detector and the NE-213 detector were passed to LRS 2249A and 2249W CAMAC charge-to-digital converters (QDCs) and PS 715 NIM constant-fraction (timing) discriminators. The resulting logic signals from the discriminators were passed to LRS 2228A CAMAC time-to-digital converters (TDCs) and LRS 4434 scalars. These signals were recorded on an event-by-event basis for offline processing using a LINUX PC-based data-acquisition (DAQ) system exploiting the ROOT (Brun and Rademakers, 1997) data-analysis framework. Connections to VME and CAMAC crates were respectively facilitated by a SBS 616 PCI-VME bus adapter and a CES 8210 CAMAC branch driver. In YAP calibration mode, signals from a YAP detector were periodically employed to trigger the DAQ and thus monitor the gains of the YAP detectors. In TOF mode, signals from the NE-213 detector were used to trigger the DAQ so that the gain of the NE-213 detector was continuously monitored. The NE-213 detector QDCs included a 60 ns short-gated (SG) QDC and a 500 ns long-gated (LG) QDC, both of which opened 25 ns before the analog pulse arrived. The NE-213 detector also provided the start trigger for the TOF TDC. The YAP trigger provided the stop trigger for the TOF TDC. By triggering our data-acquisition system on the NE-213 detector, we avoided unnecessary deadtime processing events seen only by the YAPs. Two particular source-related occurrences were of special interest: (1) a fast neutron detected in the NE-213 detector starting the TOF TDC with the corresponding 4.44 MeV gamma-ray detected in the YAP detector stopping it; and (2) prompt, time-correlated gamma-ray pairs emitted from the source being detected in coincidence in the NE-213 and YAP detectors (see below).

<sup>5</sup> Room background consisted primarily of 2.23 MeV gamma-rays associated with neutron capture on the hydrogen in the water and paraffin used as general radiation shielding about the source.

<sup>4</sup> The half-value layer for Pb for 60 keV gamma-rays is  $<1$  mm.

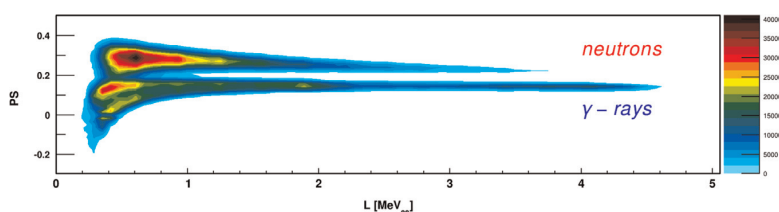


**Fig. 5.** A contour plot of pulse shape (PS) versus total energy deposited in the LG QDC (L) for correlated fast-neutron/gamma-ray events in the NE-213 detector. The upper distribution corresponds to neutrons while the lower band corresponds to gamma-rays.

### 3. Results

Fig. 5 shows a contour plot of the energy deposited in the NE-213 detector as a function of “pulse shape” (PS, see below) versus “L” (the energy deposited in the LG QDC). PS was calculated using the “tail-to-total” method (Jhingan et al., 2008; Lavagno et al., 2010; Pawczak et al., 2013); namely, the difference in the energies registered by the LG and SG QDCs was normalized to the energy registered by the LG QDC. As the NE-213 scintillator responded differently<sup>6</sup> to gamma-ray and fast-neutron events, the two distinct distributions appeared in the PS versus L contour plot. Particle identification (PID) based solely upon the pulse-shape discrimination (PSD) characteristics of the NE-213 detector was good, although some overlap between the distributions existed in the vicinity of  $PS \sim 0.2$ .

Fig. 6 presents the time-of-flight distribution of the data shown in Fig. 5. No software cut on L was applied in mapping the data from Figs. 5 and 6. The hardware threshold was 250 keV<sub>ee</sub>. The top panel shows a contour plot of PS versus time-of-flight. Time-of-flight based PID is clearly excellent. The bottom panel shows the projection of events from the top panel onto the time-of-flight axis subject to a  $PS = 0.19$  cut to separate neutrons from gamma-rays. The sharp (blue) unshaded peak centered at about 2 ns is known as the “ $\gamma$ -flash”.<sup>7</sup> The gamma-flash corresponds to a pair of prompt, time-correlated gamma-rays produced in the source which triggered both the NE-213 detector and the YAP detector. The  $\sim 1.8$  ns FWHM of the gamma-flash is consistent with the timing jitter on our PMT signals. The tail of events to the right of the gamma-flash corresponds to non-prompt gamma-rays<sup>8</sup> and randoms (see below). The broad (red) shaded peak centered at about 25 ns corresponds to time-correlated 4.44 MeV gamma-ray/fast-neutron pairs where the fast neutron triggered the NE-213 detector while the 4.44 MeV gamma-ray triggered the YAP detector. A neutron with time-of-flight measured in this manner has been tagged. The very low level of background consists of randoms. Random events arose when the NE-213 detector started the time-of-flight measurement, but no correlated stop was received from the YAP. Typical random events included cosmic rays, room background, Am/Be neutrons not correlated with a 4.44 MeV gamma-ray, and Am/Be neutrons where the 4.44 MeV gamma-ray was missed due to YAP inefficiency or geometry.

Fig. 7 shows our tagged-neutron results together with previous results, the ISO 8529-2 reference neutron radiation spectrum for Am/Be,<sup>9</sup> and theoretical calculations. Our data represent yield – they have not been corrected for neutron-detection efficiency or

detector acceptance. In all three panels, the maximum values of the spectra at  $\sim 3$  MeV have been normalized to our distribution. The reference neutron radiation spectrum is shown in the top panel together with the full-energy neutron spectrum of Lorch (1973) which is widely quoted in conjunction with work with Am/Be sources. Agreement between the Lorch data and the reference spectrum is very good between 2.5 MeV and 10 MeV. The reference spectrum shows some strength above 10 MeV which Lorch did not observe. Our data show no strength above  $\sim 7$  MeV due to the neutron-tagging procedure – 4.44 MeV potentially available to the neutron are “lost” to the creation of the de-excitation gamma-ray. This is neither an acceptance nor an efficiency effect, it is purely energetics. The reference spectrum shows considerable strength below 2.5 MeV. Our data also show some strength in this region. The Lorch data do not. The sharp cutoff at about 2.5 MeV in the Lorch data is not directly discussed in the reference, but based upon its appearance in spectra from several different sources all measured with the same apparatus, we attribute it to an analysis threshold cut as it lies well above their quoted neutron-detector threshold of 1 MeV. Our hardware threshold was 250 keV<sub>ee</sub> corresponding to a neutron energy of  $\sim 1.3$  MeV, and no analysis threshold cut was employed. The agreement between our data, those of Lorch, and the reference spectrum between 2.5 and 5 MeV (in the region of overlap) is excellent. The method of tagging the 4.44 MeV de-excitation gamma-ray and a comparable Am/Be source<sup>10</sup> were employed by Geiger and Hargrove (1964) in obtaining the results shown in the middle panel. Both the neutrons and the gamma-rays from their source were detected in Naton 136 plastic scintillators. Agreement with our results is very good. We attribute the small difference in the strengths observed in the two measurements to neutron-detection efficiency and acceptance effects which we do not consider. We attribute the relative broadening of their measured neutron distribution with respect to ours to their quoted poorer than 12% energy resolution for neutron detection, which based on the numbers quoted in their manuscript, we gather was calculated at 2 MeV. At 2 MeV, based upon our gamma-flash FWHM of 1.8 ns, time-of-flight path length of 0.675 m, and detector half-depth of 3.1 cm, our energy resolution was 11%. At 4 MeV, our energy resolution was 19%. The three independent theoretical calculations of the tagged-neutron yield shown in the bottom panel come from Vijaya and Kumar (1973), Van der Zwan (1968), and De Guarrini and Malaroda (1971). The details of these calculations are beyond the scope of this paper, but clearly all three are in reasonable agreement both with each other as well as our results. We conclude we are tagging neutrons.

### 4. Summary

We have employed shielding, coincidence, and time-of-flight measurement techniques to tag fast neutrons emitted from an Am/

<sup>6</sup> In the liquid scintillator NE-213, gamma-ray scintillations are fast while neutron-associated scintillations have pronounced slow components. Analysis of the time structure of the scintillation components leads to particle identification (PID) and is known as pulse-shape discrimination (PSD).

<sup>7</sup> The instant of the production in the source of the correlated pair of events which produce the time-of-flight data is known as “ $T_0$ ” and is located at a time-of-flight of 0 ns.

<sup>8</sup> A non-prompt gamma-ray can result from inelastic neutron scattering.

<sup>9</sup> While we employ the reference spectrum in our discussion of results, the interested reader may refer to Marsh et al. (1995) and Chen et al. (2014).

<sup>10</sup> Their source capsule was slightly smaller and emitted about 50% more neutrons per second.

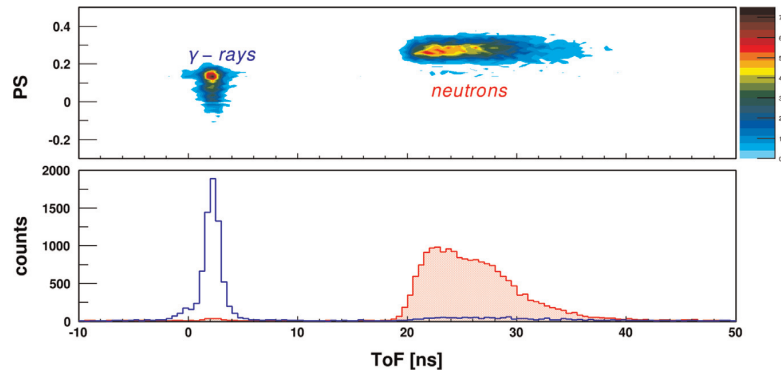


Fig. 6. Time-of-flight distributions. The top panel shows a contour plot of PS versus time-of-flight (ToF). The bottom panel shows the projection of events from the top panel onto the time-of-flight axis. Events identified as gamma-rays in Fig. 5 (the  $\gamma$ -flash) are presented in the sharp (blue) unshaded histogram, while events identified as neutrons are presented in the (red) shaded histogram. (For interpretation of the references to color in this figure caption, the reader is referred to the web version of this article.)

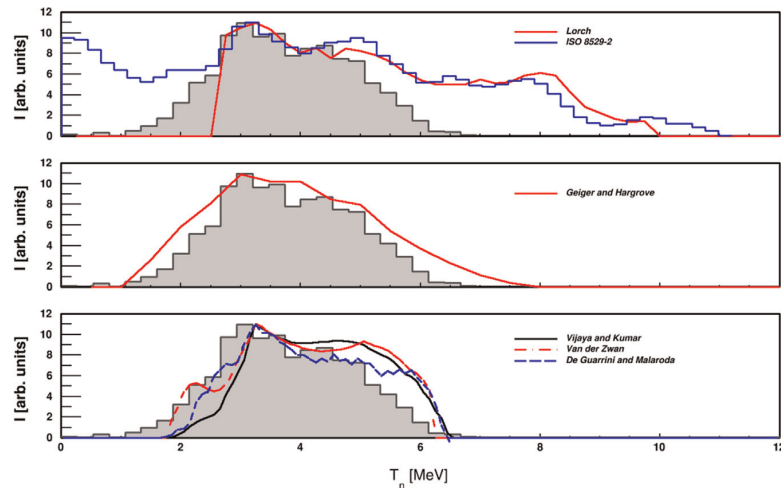


Fig. 7. Our results (the gray shaded histogram) and comparisons. Top panel: the full-energy neutron spectrum (red line) of Lorch (1973) and the ISO 8529-2 reference neutron radiation spectrum for Am/Be (blue open histogram). Middle panel: tagged-neutron results obtained by Geiger and Hargrove (1964) (red line). Bottom panel: theoretical calculations of the tagged-neutron spectrum. The solid black line represents the calculation of Vijaya and Kumar (1973), the red dashed line represents the calculation of Van der Zwan (1968), and the blue dot-dashed line represents the calculation of De Guarrini and Malaroda (1971). (For interpretation of the references to color in this figure caption, the reader is referred to the web version of this article.)

Be source as a first step towards developing a source-based fast-neutron irradiation facility. The resulting continuous polychromatic energy-tagged neutron beam has a measured energy structure that agrees qualitatively with both previous measurements and theoretical calculations. We conclude that our approach works as expected, and anticipate that it can provide a cost-effective means for detector characterization and tests of shielding. We note that this technique will work equally well for all Be-compound neutron sources.

## Acknowledgments

We thank the Photonuclear Group at the MAX IV Laboratory for providing access to their experimental hall and Am/Be source. We acknowledge the support of the UK Science and Technology Facilities Council (Grant nos. STFC 57071/1 and STFC 50727/1).

## References

Araldite is a Registered Trademark of Huntsman. (<http://www.araldite2000plus.com>).

- Brun, R., Rademakers, F., 1997. ROOT—an object oriented data analysis framework. In: Proceedings AIHENP'96 Workshop, Lausanne, September 1996; Nucl. Instrum. Methods Phys. Res. A 389, 81–86. See also (<http://root.cern.ch/>).
- Chandra, R., Davatz, G., Gendotti, U., Howard, A., 2010. IEEE NSS/MIC, 508.
- Chandra, R., Davatz, G., Friederich, H., Gendotti, U., Murer, D., 2012. J. Instrum. 7, C03035.
- Chen, Y., Chen, X., Lei, J., An, L., Zhang, X., Shao, J., Zheng, P., Wang, X., 2014. Science China Physics. Mech. Astron. 57, 1885.
- De Guarrini, F., Malaroda, R., 1971. Nucl. Instrum. Methods 92, 277.
- Geiger, K.W., Hargrove, C.K., 1964. Nucl. Phys. 53, 204.
- Hamamatsu Photonics. (<http://www.hamamatsu.com>).
- Supplied by High Tech Sources Limited, Unit 6, Moorbrook, Southmead, Industrial Estate, Didcot, Oxfordshire, UK OX11 7HP; (<https://www.hightechsource.co.uk/>) For details see ([www.hightechsource.co.uk/Legacy/Resources/Americium-Beryllium.pdf](http://www.hightechsource.co.uk/Legacy/Resources/Americium-Beryllium.pdf)).
- (<http://www.eljentechnology.com/index.php/products/paints/86-ej-510>).
- (<http://www.eljentechnology.com/index.php/products/paints/87-ej-520>).
- ([www.et-enterprises.com/files/file/Pmtbrochure11.pdf](http://www.et-enterprises.com/files/file/Pmtbrochure11.pdf)) for details.
- Proceedings from the Workshop on Neutron, Neutrino, Nuclear, Muon and Medical Physics at ESS, Lund, Sweden, 2009. (<http://www.hep.lu.se/staff/christiansen/proceeding.pdf>).
- Second International Workshop on Fast Neutron Detectors and Applications (FNDA2011), Kibbutz Ein Gedi, Israel, 2011. J. Instrum. 7C (2012). (<http://iopscience.iop.org/1748-0221/focus/extra/proc19>).
- Workshop on Fast Neutron Applications at Spallation Sources, Abingdon, UK, 2013. (<http://plone.esss.lu.se/>).
- International Workshop on Fast Neutron Detectors and Applications (FNDA2006), University of Capetown, South Africa (2006). Proceedings of Science

- (FNDA2006). (<http://pos.sissa.it/cgi-bin/reader/conf.cgi?confid=25>). (<http://www.us.schott.com/borofloat/english/index.html>) for details. Supplied by Glasteknik i Emmaboda AB, Utvägen 6 SE-361 31 Emmaboda, Sweden.
- Islam, M.R., Khan, M.I., 2013. Current practice in well logging, reservoir engineering and secondary recovery. In: *The Petroleum Engineering Handbook: Sustainable Operations*. Gulf Publishing Company, Houston, Texas (an imprint of Elsevier).
- Jhingan, A., Singh, H., Singh, R.P., Gola, K.S., Sugathan, P., Mandal, S., Bhowmik, R.K., 2008. *Nucl. Instrum. Methods Phys. Res. A* 585, 165.
- Knox, H.H., Miller, T.G., 1972. *Nucl. Instrum. Methods* 101, 519.
- Lavagno, A., Gervino, G., Marino, C., 2010. *Nucl. Instrum. Methods Phys. Res. A* 617, 492.
- Lewis, J.M., Raetz, D., Murer, D., Jordan, K.A., 2013. Third International Conference on Advancements in Nuclear Instrumentation Measurement Methods and their Applications, Marseille, France. (<http://ieeexplore.ieee.org/stamp/stamp.jsp?tp=&arnumber=6728031>).
- Lewis, J.M., Kelley, R.P., Murer, D., Jordan, K.A., 2014. *Appl. Phys. Lett.* 105, 014102.
- Liu, Zhenzhou, Chen, Jinxiang, Zhu, Pei, Li, Yongming, Zhang, Guohui, 2007. *Appl. Radiat. Isot.* 65, 1318.
- Lorch, E.A., 1973. *Int. J. Appl. Radiat. Isot.* 24, 585.
- Lyons, W.C., Plisga, G.J., 2011. *Drilling and well completions, reservoir engineering*. In: *Standard Handbook of Petroleum and Natural Gas Engineering*, 2nd ed., Gulf Publishing Company, Houston, Texas (an imprint of Elsevier).
- Marsh, J.W., Thomas, D.J., Burke, M., 1995. *Nucl. Instrum. Methods Phys. Res. A* 366, 340.
- Moszyński, M., Kapustab, M., Wolski, D., Klamra, W., Cederwall, B., 1998. *Nucl. Instrum. Methods Phys. Res. A* 404, 157.
- Mowlavi, A.A., Koohi-Fayegh, R., 2004. *Appl. Radiat. Isot.* 60, 959.
- Testing performed at National Physical Laboratory, Teddington, Middlesex, UK TW11 0LW on 24 January 2012.
- NE-213 is no longer produced. Eljen Technologies offers EJ-301 (<http://www.eljentechnology.com/index.php/products/liquid-scintillators/71-ej-301>) while Saint Gobain offers BC-501 ([http://www.detectors.saint-gobain.com/uploadedFiles/SGdetectors/Documents/Product\\_Data\\_Sheets/BC501-501A-519-Data-Sheet.pdf](http://www.detectors.saint-gobain.com/uploadedFiles/SGdetectors/Documents/Product_Data_Sheets/BC501-501A-519-Data-Sheet.pdf)).
- Paweczak, I.A., Ouedraogo, S.A., Glenn, A.M., Wurtz, R.E., Nakae, L.F., 2013. *Nucl. Instrum. Methods Phys. Res. A* 711, 21.
- Peerani, P., Tomanin, A., Pozzi, S., Dolan, J., Miller, E., Flaska, M., Battaglieri, M., De Vita, R., Ficini, L., Ottonello, G., Ricco, G., Dermody, G., Giles, C., 2012. *Nucl. Instrum. Methods Phys. Res. A* 696, 110.
- Poly(methyl-methacrylate), also known as acrylic, plexiglass, and lucite. Supplied by Nordic Plastics Group AB, Bronsyxegatan 6, SE-213 75 Malmö, Sweden.
- Scionix Holland BV. (<http://www.scionix.nl>).
- Tomanin, A., Paepen, J., Schillebeeckx, P., Wynants, R., Nolte, R., Laviertes, A., 2014. *Nucl. Instrum. Methods Phys. Res. A* 756, 45.
- United States Committee on Army Science and Technology for Homeland Defense, 2003. Board on Army Science and Technology, Division on Engineering and Physical Sciences, National Research Council, Indications and Warning Technologies, in Science and Technology for Army Homeland Security: Report 1. National Academies Press, Washington, DC.
- Van der Zwan, L., 1968. *Can. J. Phys.* 46, 1527.
- Vijaya, A.D., Kumar, A., 1973. *Nucl. Instrum. Methods* 111, 435.
- Viton is a Registered Trademark of DuPont Performance Elastomers LLC.
- Walker, J., 1982. *Phys. Technol.* 13, 239.

Paper II







Contents lists available at ScienceDirect

# Nuclear Instruments and Methods in Physics Research A

journal homepage: [www.elsevier.com/locate/nima](http://www.elsevier.com/locate/nima)

## A first comparison of the responses of a $^4\text{He}$ -based fast-neutron detector and a NE-213 liquid-scintillator reference detector



R. Jebali<sup>a,1</sup>, J. Scherzinger<sup>b,c</sup>, J.R.M. Annand<sup>d</sup>, R. Chandra<sup>a</sup>, G. Davatz<sup>a</sup>, K.G. Fissum<sup>b,c,\*</sup>, H. Friederich<sup>a</sup>, U. Gendotti<sup>a</sup>, R. Hall-Wilton<sup>c,f</sup>, E. Håkansson<sup>b</sup>, K. Kanaki<sup>c</sup>, M. Lundin<sup>e</sup>, D. Murer<sup>a</sup>, B. Nilsson<sup>c,e</sup>, A. Rosborg<sup>e</sup>, H. Svensson<sup>e,g</sup>

<sup>a</sup> Arktis Radiation Detectors Limited, 8045 Zürich, Switzerland

<sup>b</sup> Division of Nuclear Physics, Lund University, SE-221 00 Lund, Sweden

<sup>c</sup> Detector Group, European Spallation Source ESS AB, SE-221 00 Lund, Sweden

<sup>d</sup> University of Glasgow, Glasgow G12 8QQ, Scotland, UK

<sup>e</sup> MAX IV Laboratory, Lund University, SE-221 00 Lund, Sweden

<sup>f</sup> Mid-Sweden University, SE-851 70 Sundsvall, Sweden

<sup>g</sup> Sweflo Engineering, SE-275 63 Blentarp, Sweden

### ARTICLE INFO

#### Article history:

Received 26 February 2015

Received in revised form

27 April 2015

Accepted 27 April 2015

Available online 5 May 2015

#### Keywords:

$^4\text{He}$

NE-213

Scintillation

Gamma-rays

Fast neutrons

Pulse-shape discrimination

### ABSTRACT

A first comparison has been made between the pulse-shape discrimination characteristics of a novel  $^4\text{He}$ -based pressurized scintillation detector and a NE-213 liquid-scintillator reference detector using an Am/Be mixed-field neutron and gamma-ray source and a high-resolution scintillation-pulse digitizer. In particular, the capabilities of the two fast neutron detectors to discriminate between neutrons and gamma-rays were investigated. The NE-213 liquid-scintillator reference cell produced a wide range of scintillation-light yields in response to the gamma-ray field of the source. In stark contrast, due to the size and pressure of the  $^4\text{He}$  gas volume, the  $^4\text{He}$ -based detector registered a maximum scintillation-light yield of 750 keV<sub>ee</sub> to the same gamma-ray field. Pulse-shape discrimination for particles with scintillation-light yields of more than 750 keV<sub>ee</sub> was excellent in the case of the  $^4\text{He}$ -based detector. Above 750 keV<sub>ee</sub> its signal was unambiguously neutron, enabling particle identification based entirely upon the amount of scintillation light produced.

© 2015 The Authors. Published by Elsevier B.V. This is an open access article under the CC BY license (<http://creativecommons.org/licenses/by/4.0/>).

### 1. Introduction

Fast neutrons are important both as probes of matter and as diagnostic tools [1–14]. In the case that information about the energy and emission time of a neutron is available, conclusions about its origin can be drawn. The timing precision required to obtain this information may only be provided by neutron detectors that are fast, providing signals with short risetimes. Today, organic liquid scintillators are the detectors-of-choice for fast neutrons. Drawbacks associated with these scintillators are their toxicity, reactive nature, and sensitivity to a broad range of gamma-ray energies.

Scintillators are substances which emit light when subjected to ionizing radiation. The characteristic time constant associated with the light emitted is a function of the properties of the scintillator in question. Certain scintillators respond to different types of ionizing

radiation differently; that is, the time constant of the emitted light is different depending upon the density of ionization produced by the incident radiation. Normally, there are several components with different time constants. The relative intensity of these components affects the effective integrated time constant. By carefully analyzing the behavior of the scintillation light as a function of time, one can determine the incident particle type. This procedure is called pulse-shape discrimination (PSD). PSD is often used to distinguish between different types of uncharged particles, namely gamma-rays and neutrons. In scintillators with good PSD properties, incident gamma-rays interact primarily with the atomic electrons of the scintillator, producing close to minimum-ionizing electrons which give a fast (decay times of some 10 s of ns) flash of light. On the other hand, incident neutrons interact primarily with the hydrogen in liquid scintillators and  $^4\text{He}$  nuclei in noble-gas scintillators via scattering, transferring some of their energy. For hydrogen, this energy transfer can be 100%, while for  $^4\text{He}$ , the energy transfer is at best 64%. The resulting flashes of light arising from the much denser ionization produced by the relatively large energy loss of the recoiling protons and alpha particles have longer decay times (100–1000 s of ns). PSD

\* Corresponding author at: Division of Nuclear Physics, Lund University, SE-221 00 Lund, Sweden. Tel.: +46 46 222 9677; fax: +46 46 222 4709.

E-mail address: [kevin.fissum@nuclear.lu.se](mailto:kevin.fissum@nuclear.lu.se) (K.G. Fissum).

<sup>1</sup> Present address: University of Glasgow, Glasgow G12 8QQ, Scotland, UK.

and thus incident particle identification may be performed by recording the time dependence of the scintillation pulse form and comparing the fast and slow components.

## 2. $^4\text{He}$ as a scintillation medium for fast neutron detection

The development of both liquid and gaseous  $^4\text{He}$  based scintillators for fast-neutron detection has been reported [6,8,12,14,15].  $^4\text{He}$ , like most noble gases, is a good scintillator. It has an ultra-violet light yield comparable to the intrinsic non-Tl doped light yield of NaI crystals [16–19]. Neutron interactions lead to  $^4\text{He}$  recoils, where energy is deposited very locally within the gas. Gamma-ray interactions lead to recoiling electrons, which deposit only tens of keV per centimeter of trajectory. This difference in deposition density and therefore ionization density is believed to ultimately enable the PSD capability. PSD properties may be degraded significantly if the geometry and size of the detector results in a smearing of the transit times of scintillation photons comparable to the scintillation decay times. Good PSD also requires good scintillation efficiency; that is, a sufficient number of scintillation photons to define the time dependence of the pulse accurately, and low noise in the pulse-processing electronics.

With only two electrons per atom,  $^4\text{He}$  has a very low charge density, thereby significantly limiting its sensitivity to gamma-rays. This is useful for fast-neutron detection, where insufficient gamma-ray rejection is often the factor which constrains the desired performance. The following physical effects contribute positively to the gamma-ray rejection performance of pressurized  $^4\text{He}$  gas:

1. *Low gamma-ray interaction probability.* Due to the low electron density of  $^4\text{He}$ , gamma-ray interaction probabilities are two orders of magnitude lower than neutron interaction probabilities.
2. *Low energy deposition.* Depending on the chosen geometry (i.e. a tube with radius of a few cm), the amount of energy the gamma-rays can deposit in the detector volume is limited. This is because the corresponding Compton or pair electrons cannot transfer much energy to the gas before striking a detector wall.
3. *Similar scintillation-light yield for gamma-rays and neutrons.* The scintillation light production in organic liquid scintillators is highly velocity dependent. Thus, for the same amount of deposited energy, gamma-ray interactions produce more scintillation light than neutron interactions. In contrast, the

scintillation-light yield for gamma-rays and neutrons is similar in noble-gas scintillators [17] such as  $^4\text{He}$ .  $^4\text{He}$  is commonly called a linear scintillator.

4. *PSD.* 1–3 above together with the fast and slow components of the  $^4\text{He}$  scintillation signals lead to excellent PSD and thus excellent separation of neutrons and gamma-rays.

The purpose of this project was to compare the neutron/gamma discrimination obtained using the Arktis  $^4\text{He}$ -based neutron-diagnostic tool (NDT) to that obtained using a reference liquid-scintillator cell filled with the organic liquid scintillator NE-213 [20].

## 3. Apparatus

### 3.1. Am/Be source

The detector characterizations reported on in this paper were carried out using a nominal 18.5 GBq  $^{241}\text{Am}/^9\text{Be}$  (Am/Be) source [21] which emitted  $(1.106 \pm 0.015) \times 10^6$  neutrons per second nearly isotropically [22]. The source is a mixture of americium oxide and beryllium metal contained in an X.3 capsule, which is a stainless-steel cylinder 31 mm (height)  $\times$  22.4 mm (diameter) [23].  $^{241}\text{Am}$  has a half-life of 432.2 years and decays via alpha emission (5 discrete energies with an average value of about 5.5 MeV) to  $^{237}\text{Np}$ . The dominant energy of the gamma-rays associated with the decay of the intermediate excited states in  $^{237}\text{Np}$  is  $\sim 60$  keV. A 3 mm thick Pb sheet was used to complement the stainless steel X.3 capsule to attenuate these 60 keV gamma-rays. The half-value layer for Pb for 60 keV gamma-rays is 0.12 mm, while for 1 MeV gamma-rays, it is 8 mm. Neutrons are produced when the emitted alpha particles undergo a nuclear reaction with  $^9\text{Be}$  resulting in  $^{12}\text{C}$  and a free neutron. The resulting neutron distribution has a maximum energy of about 11 MeV [24], while approximately 25% of the neutrons have an energy of less than 1 MeV [25]. The de-excitation of the  $^{12}\text{C}$  results in a 4.44 MeV gamma-ray about 55% of the time [25–27]. This gamma-ray is too energetic to be absorbed by the stainless steel of the X.3 capsule. Thus the radiation field from the Am/Be is a combination of high-energy gamma-rays and fast neutrons. Both the gamma-ray and fast-neutron dose rates at a distance of 1 m from the source in the unshielded X.3 capsule were measured using a Thermo Scientific Corporation FHT 752 dosimetric neutron detector [28]. They were both determined to be 11  $\mu\text{Sv/h}$  for a total unshielded dose rate of 22  $\mu\text{Sv/h}$ , in exact agreement with the data sheet from the supplier.

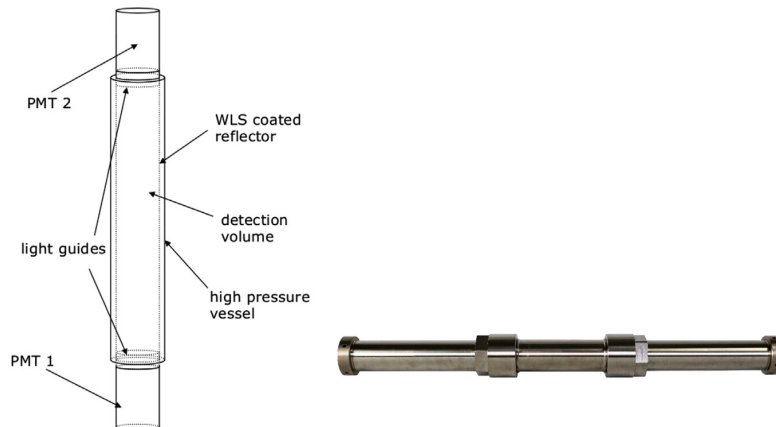


Fig. 1. Schematic (left) and photograph (right) of the pressurized  $^4\text{He}$  gas fast-neutron detector. The outer diameter was 5.08 cm (2 in.) and the active length was 19.5 cm.

### 3.2. Arktis pressurized $^4\text{He}$ gas neutron diagnostic tool (NDT)

The version of the Arktis pressurized gas  $^4\text{He}$  fast NDT used for these measurements is shown in Fig. 1. It was of cylindrical geometry with an outer diameter of 5.08 cm (2 in.) and a 19.5 cm active length. The detector walls were made of stainless steel. The interior surface of the stainless-steel cylinder was coated with a PTFE-based diffuse reflector [29] which was itself coated with an organic phosphor that converted the wavelength of the scintillation light from 80 nm to 430 nm. As  $^4\text{He}$  is transparent to its own light, almost no signal loss due to reabsorption occurs [30]. The predominant mechanism for signal loss was due to multiple reflections inside the detector. Optical windows capable of withstanding the 120 bar operating pressure were employed. The scintillation signals were read out at both ends of the active volume by Hamamatsu R580 [31] photomultiplier tubes (PMTs).

### 3.3. NE-213 reference detector

The NE-213 reference detector is shown in Fig. 2. The core of the NE-213 reference detector was a 3 mm thick cylindrical aluminum cell with an inner depth of 62 mm and an inner diameter of 94 mm. The inside of the cell was painted with EJ-520 [32] titanium dioxide reflective paint, which can withstand the xylene solvent of the liquid scintillator. The aluminum cell was sealed using a 5 mm thick borosilicate glass window [33] glued to the aluminum cell using the highly temperature and chemical resistant Araldite 2000+ [34]. The 2 penetrations into the cell which allowed for filling were sealed with M-8 threaded aluminum plugs with 20 mm diameter heads and 14 mm diameter Viton O-rings [35]. Nitrogen gas was bubbled through the NE-213 liquid scintillator for 24 h prior to filling the cell. The assembled cell was then filled with the nitrogen-flushed NE-213 using a nitrogen gas transfer system.

After filling, the borosilicate glass window of the cell was coupled to a cylindrical PMMA [36] lightguide with a depth of 57 mm and a diameter of 72.5 mm. PMMA is an acrylic which transmits light down to 300 nm in wavelength [37]. The cylindrical surface of this lightguide was painted with water-soluble EJ-510 [38] reflective paint. The lightguide was then pressure-coupled via springs to a magnetically shielded 3 in. ET Enterprises 9821KB PMT assembly [39]. As our goal was to produce a stable detector which provided reproducible results, no optical-coupling grease was used.

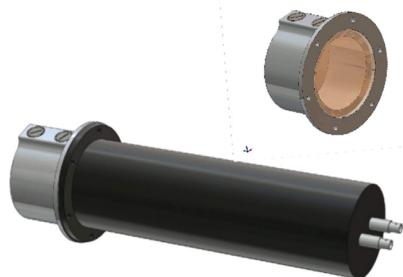


**Fig. 2.** The NE-213 reference detector. Top: a detail of the cylinder “cup”. The screws on top allow for the filling or draining of the liquid cylinder. A borosilicate-glass window (light brown) serves as the optical boundary. See text for details. Bottom: The black cylinder to the right is the magnetically shielded 3 in. ET Enterprises 9821 KB photomultiplier-tube assembly. The gray cylinder to the left is the “cup”. (For interpretation of the references to color in this figure caption, the reader is referred to the web version of this paper.)

### 3.4. Arktis waveDREAM-B16 digitizer

The analog signals from the NDT and NE-213 reference cell were fed directly to a WaveDREAM-B16 high-precision digitizer developed by Arktis Radiation Detectors [40] (see Fig. 3). After being converted to a digital signal, the data of interest were stored for analysis. The decision for storage was based on a 120 mega-sample per second (MSPS) signal that was continuously read out and fed into a field programmable gate array (FPGA). If the user-defined trigger condition was met (see below for the trigger conditions employed in this measurement), the FPGA read out the DRS4 switched capacitor array [41] containing the stored waveform at 1 gigasample per second (GSPS). Complete details are presented in Ref. [42]. In this manner, excellent time resolution (provided by the 1 GSPS sampling and nanosecond time stamping also between different detectors) was achieved at 10-bit resolution over the 3.5  $\mu\text{s}$  duration of the stored event. The trigger conditions were user-configurable. In the case of the NDT, a trigger occurred only if the signals from both PMTs mounted on each end of the detector were above threshold. This threshold was 35 scintillation photons detected above the ambient baseline, and suppressed the dark-current count rate. An event was considered to be valid if the second PMT signal came less than 32 ns after the first, a criterion related to the speed of light, dimensions of the  $^4\text{He}$  gas volume, and response of the PMTs. This broad timing window in the digitizer was inherited from studies of a different system and was considered to be “safe” for the investigations of the much smaller NDT studied here. In the case of the NE-213 reference cell which had only one PMT, a trigger occurred if the analog signal coming from the PMT was above threshold. This threshold was 30 scintillation photons detected above the ambient baseline. The digitizer greatly facilitated the offline analysis of the data as it allowed for the Arktis NDT PMTs to be synchronized to better than 1 ns. It also allowed for offline variation in the detector thresholds

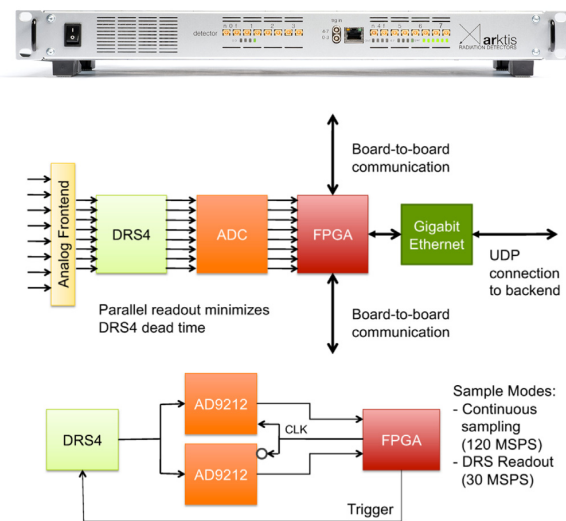


**Fig. 3.** The top figure shows the WaveDREAM-B16. There are 16 input channels grouped in 2 clusters of 8. Once the selected signals are digitized, they are read out via Gigabit ethernet. Triggers can be applied externally or generated internally by the software. The middle figure is a schematic overview of the readout electronics. Signals are stored in the DRS4 switched-capacitor array and read out if user-defined trigger conditions are met. The bottom figure presents an overview of the software trigger. If the signal sampled at 120 MSPS meets the trigger condition, the FPGA reads out the DRS4 at 1 GSPS. See Ref. [42] for further details.

and integration gates (see below), a clear advantage over standard discriminators and analog-to-digital converters.

## 4. Measurement

### 4.1. Setup

The experiment setup is shown in Fig. 5. The Am/Be source in its transport/storage container was placed at the center of a 4-sided enclosure constructed from borated-wax boxes. In the so-called “park” position with the source locked in its transport container at the bottom of the borated-wax box enclosure, the total dose rate in the room was less than  $0.4 \mu\text{Sv/h}$ . When the source was lifted from its container and positioned within the 3 mm Pb thick sleeve, the gamma-ray dose rate on the outside of the 4-sided borated-wax enclosure was  $1 \mu\text{Sv/h}$ .

Square penetrations through 2 of the opposite walls of the enclosure allowed direct line-of-sight between the detectors being irradiated and the source. A HPGe gamma-ray detector was positioned in one of the apertures. The distance to the screened source was  $\sim 1$  m and line-of-sight was direct. It was used to measure the distribution of gamma-rays at the approximate location of the NDT and NE-213 reference cell. Fig. 4 presents this distribution, where the 4.44 MeV gamma-ray peak together with its Compton edge, first- and second-escape peaks, and their Compton edges are clearly seen between (from the right) 5 and 3 MeV. Between 1.0 MeV and the  $\sim 400$  keV detector threshold, the gamma-ray intensity increased by an order-of-magnitude.

At a distance of 0.54 m from the source, the square aperture for the NE-213 reference detector was  $17 \times 17 \text{ cm}^2$ . The cell was placed at source height so that the face of the active volume (recall Fig. 2) was 70 cm from the center of the Am/Be source. The cylindrical symmetry axis of the detector pointed directly at the center of the source. It was operated at  $-1700$  V. The analog signals from the single PMT were fed into the digitizer. The digitized waveforms of the signals which triggered the acquisition were recorded on an event-by-event basis for offline processing. At the same distance from the source, the square aperture for the NDT was  $25 \times 25 \text{ cm}^2$ . The NDT was also placed at source height. However, its cylindrical symmetry axis was perpendicular to the ray pointing to the center of the source. Both of the PMTs (one at each end of the detector volume) were operated at  $+1730$  V. The analog signals from these PMTs were fed into the digitizer. Again, the digitized waveforms of the signals which triggered the acquisition were recorded on an event-by-event basis for offline processing.

A pulse-shape (PS) analysis of the analog signals coming from both detectors was performed using the “tail-to-total” method. Two integration gates were defined, a long gate (LG) and a short

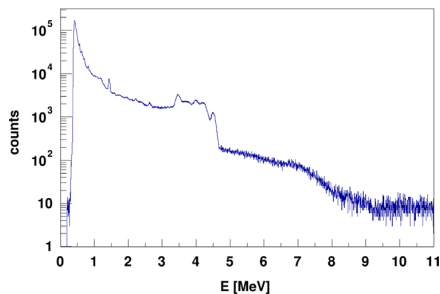


Fig. 4. Energy distribution of gamma-rays at the approximate location of the NDT and NE-213 reference cell. The prominent structure between 3 and 5 MeV results from the 4.44 MeV gamma-ray.

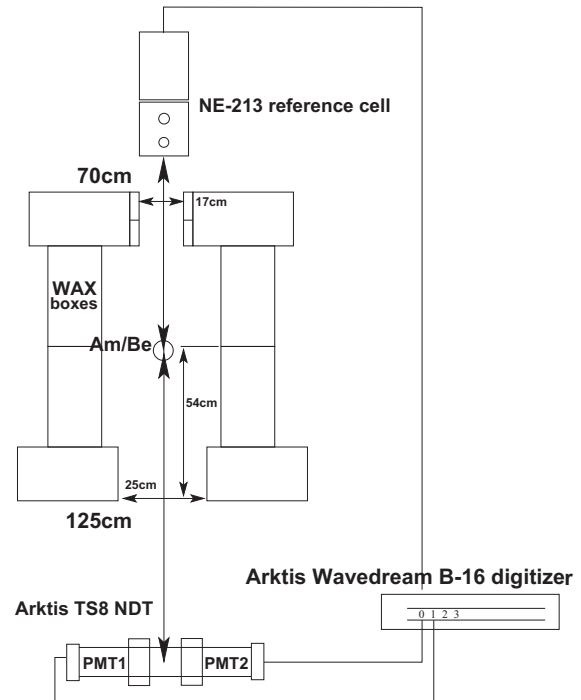


Fig. 5. The experiment setup (not to scale). The Am/Be source was placed at the center of a borated-wax enclosure. Penetrations through two of the enclosure walls allowed for a direct line-of-sight between the source and the detectors. For measurements of the gamma-ray distribution at the apertures, the NE-213 reference cell was replaced with a stand-alone HPGe detector.

gate (SG). Both of the gates opened at the same time, 10 ns before the analog signal. The SG was used to integrate only the fast components of the analog signal, while the LG was used to integrate the entire (both fast and slow components) analog signal. The PS was determined from the difference between the scintillation-light yield in the LG and SG normalized to the scintillation-light yield in the LG:  $PS = (LG - SG) / LG$ . For the NDT PMT data, the SG was 100 ns (related to the decay constant of the fast-scintillation components of  $^4\text{He}$ ) and the LG was 3500 ns (the maximum gate length the digitizer provided). For the NE-213 reference cell data, the SG was 25 ns and the LG was 150 ns. The Arktis NDT gate widths were optimized offline. This procedure was greatly facilitated by the digitizer.

### 4.2. Absolute energy calibration

Energy-calibration measurements for the NE-213 reference cell were performed using  $^{60}\text{Co}$ ,  $^{137}\text{Cs}$ , and the Pb-shielded Am/Be sources.  $^{60}\text{Co}$  emits gamma-rays with energies 1.17 MeV and 1.33 MeV.  $^{137}\text{Cs}$  emits a gamma-ray with an energy 0.66 MeV. The de-excitation gamma-ray from the first excited state of  $^{12}\text{C}$  has an energy of 4.44 MeV. The locations of the Compton edges from these gamma-rays were determined using the prescription of Knox and Miller [43].

For the NDT, Geant4 simulations [44,45] reproduce the shape of the observed pulse-height distributions for neutrons and gamma-rays well. The  $\alpha$  decay of trace amounts of  $^{222}\text{Rn}$  in the  $^4\text{He}$  gas of the NDT provides an energy signature similar to the neutron/ $^4\text{He}$  scattering process, and was used to calibrate the detector. Neutrons, which produce a recoiling  $\alpha$  particle, were correlated directly to the 5.5, 6.0, and 7.7 MeV  $\alpha$  lines in  $^{222}\text{Rn}$  [8]. Gamma-rays produce an electron via Compton scattering or an electron

and positron via pair production. These interactions occur dominantly in the relatively high-Z walls of the NDT. Apart from very low energies, most electrons or positrons entering the  $^4\text{He}$  gas volume do not stop in the gas. On traversing the gas, they lose a fairly well-defined energy of around 150 keV. This produces a peak in the pulse-height distribution which can be used for cross-calibration. The energy-loss distribution extends out to around 750 keV, which is more or less independent of the incident gamma-ray energies above 750 keV. These energy losses are of course dependent upon the size and pressure of the  $^4\text{He}$  gas volume. From this, we have established that the scintillation-light yield is the same for electrons and alpha particles, consistent with  $^4\text{He}$  being a linear scintillator. This contrasts with NE-213, where the scintillation-light yield depends strongly on the velocity and ionization density of the interacting particle.

## 5. Results

We stress that the data presented in this section came directly from the digitizer and were not optimized via offline software corrections in any way. Fig. 6 shows a two-dimensional scatterplot comparison of the PSD achieved using the NE-213 reference cell and the  $^4\text{He}$ -based NDT obtained using the Pb-screened Am/Be source. Recall that the Pb-screened Am/Be source provided a continuous energy spectrum of neutrons up to 11 MeV and gamma-rays up to 4.44 MeV. The gamma-ray pulse-height response of the NE-213 reference cell extends to 4 MeV<sub>ee</sub> as shown in the upper panel. Below 500 keV<sub>ee</sub>, significant overlap between the neutron and gamma-ray pulse-height responses occurred. As shown in the lower panel and in stark contrast, the gamma-ray pulse-height response of the Arktis NDT extends only to 750 keV<sub>ee</sub>, and clear separation between the neutron and gamma-ray pulse-height responses is evident down to 100 keV<sub>ee</sub>.

The amount of scintillation light produced in the gaseous  $^4\text{He}$  is less than that produced in the liquid scintillator for both particle types. In absolute terms, the detection efficiency of the NE-213 reference cell will qualitatively be higher than the Arktis NDT, both for neutrons and gamma-rays. Quantitative evaluation of these detection efficiencies and comparisons with Monte Carlo calculations will be addressed in a future publication. We note that the lower absolute detection efficiency of the Arktis NDT could be advantageous in very high intensity radiation fields. The complete lack of a gamma-ray band to higher energies in the bottom scatterplot is striking. Relative to the numbers of neutrons detected, the gamma-ray discrimination properties of the Arktis NDT are clearly superior. The digitizer clearly proved to be a very effective tool for optimizing the PSD.

One-dimensional projections of PS have been obtained from the two-dimensional distributions shown in Fig. 6 for five different pulse-height thresholds. The resulting PS distributions for the NE-213 detector (left column) and Arktis NDT (right column) integrated from these thresholds are shown in Fig. 7. In each of the panels, wherever possible, two separate Gaussian functions have been fitted to the data – one corresponding to gamma-rays (red) and one corresponding to neutrons (blue). A standard figure-of-merit (FOM) has been used to quantify the quality of the PSD as a function of deposited-energy cut. This FOM is given by the separation between the gamma-ray and neutron peaks divided by the sum of the FWHM of these peaks.

As can be seen in the NE-213 data (left column), the FOM improves from 0.75 to 1.5 as the requirement on the light yield increases from 0.25 to 3.0 MeV<sub>ee</sub>. In comparison, the Arktis NDT FOM (right column) improves from 1.35 to 1.70 as the requirement on the light yield increases from 0.25 to 0.50 MeV<sub>ee</sub>. Once the requirement on the amount of deposited energy exceeds 0.75 MeV<sub>ee</sub>,

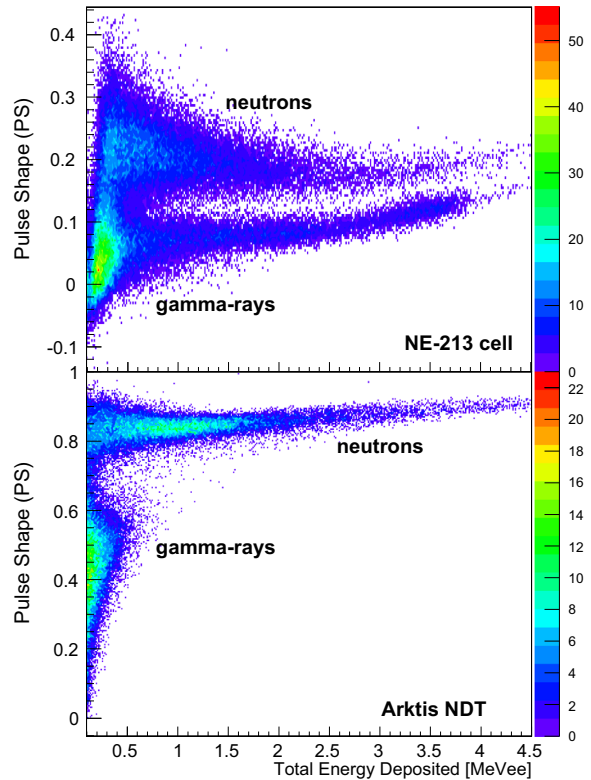
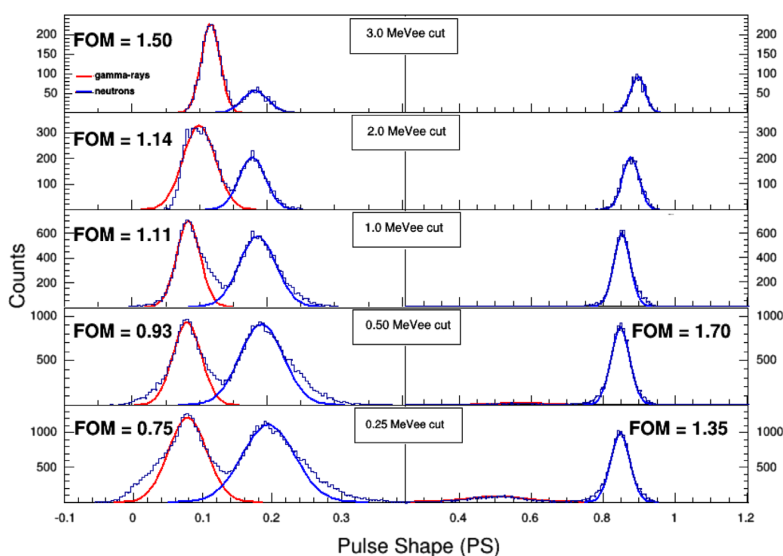


Fig. 6. A comparison of the PSD achieved using the NE-213 reference cell (top panel) and the  $^4\text{He}$ -based NDT (bottom panel) with the Pb-screened Am/Be source. For each event, the signal pulse shape  $PS=(LG-SG)/LG$  has been plotted against the scintillation-light yield produced in the detector for the LG in MeV<sub>ee</sub>. The distributions corresponding to neutrons and gamma-rays are labeled.

the gamma-ray peak is no longer visible in the Arktis NDT, and the signal is unambiguously neutron. Again, the fact that gamma-rays with energies up to 4.44 MeV deposit no more than 750 keV<sub>ee</sub> in the Arktis NDT is striking. This property of the detector greatly facilitates the identification of fast neutrons depositing more energy than this value.

## 6. Summary

A first comparison between the PSD characteristics of a novel  $^4\text{He}$ -based high-pressure gas scintillation detector and a standard NE-213 liquid-scintillator reference detector has been performed. A Pb-screened Am/Be mixed-field neutron and gamma-ray source was used to irradiate the detectors and a high-resolution scintillation-pulse digitizer was used to optimize the PSD using the tail-to-total method. The NE-213 liquid-scintillator reference cell was differentially very sensitive to the incident gamma-rays and registered a wide range of scintillation-light yields up to 4.4 MeV<sub>ee</sub>. In contrast, the  $^4\text{He}$ -based NDT was designed to have a low gamma-ray sensitivity. It registered a maximum scintillation-light yield of 750 keV<sub>ee</sub> for the same distribution of incoming gamma-rays. The PSD obtained with the NE-213 liquid-scintillator reference cell, facilitated by using the digitizer, was good. Clear separation between neutrons and gamma-rays was obtained down to about 0.5 MeV<sub>ee</sub>. The PSD obtained with the  $^4\text{He}$ -based NDT was excellent. Clear separation between neutrons and gamma-rays was obtained down to 0.1 MeV<sub>ee</sub>. Most striking was the fact that gamma-rays of energies up to 4.44 MeV resulted



**Fig. 7.** A first comparison of the PSD achieved using the NE-213 reference cell (left column) and the 4He-based NDT (right column) via a FOM using the Pb-screened Am/Be source and varying the requirements on the amount of energy deposited in the detectors. In each column, the left-most distribution (red fitted function) corresponds to gamma-rays while the right-most distribution (blue fitted function) corresponds to neutrons. Gamma-rays with energies up to 4.44MeV deposit no more than 750 keVee in the Arktis NDT which greatly facilitates fast-neutron particle identification. (For interpretation of the references to color in this figure caption, the reader is referred to the web version of this paper.)

in scintillation-light yields of no more than 750 keV<sub>ee</sub> in the NDT. As a result, a simple threshold cut above 750 keV<sub>ee</sub> was sufficient to distinguish fast neutrons from gamma-rays in this region. For fast-neutron detection, <sup>4</sup>He-based high-pressure gas scintillation detectors such as the NDT thus have a clear advantage over liquid-scintillator detectors such as the NE-213 reference cell when the scintillation-light yield is greater than 750 keV<sub>ee</sub>.

The next step in our investigations shall involve an expanded systematic comparison of the PSD obtained with these two scintillators using a FOM as a function of scintillation-light yield. The scintillation-light yield as a function of neutron energy must also be established if the potential for spectroscopy is to be investigated. In order to perform these investigations, knowledge of the incident neutron energies is required. We have recently successfully tested a technique for performing such irradiations with Be-compound neutron sources [46] which relies on well-understood shielding, coincidence, and time-of-flight measurement techniques to produce a polychromatic energy-tagged neutron beam.

## Acknowledgments

We thank the Photonuclear Group at the MAX IV Laboratory for providing access to their experimental hall and Am/Be source. We acknowledge the support of the UK Science and Technology Facilities Council (Grant nos. STFC 57071/1 and STFC 50727/1).

## References

- [1] J. Walker, *Physics in Technology* 13 (1982) 239. <http://dx.doi.org/10.1088/0305-4624/13/6/101>.
- [2] United States Committee on Army Science and Technology for Homeland Defense, Board on Army Science and Technology, Division on Engineering and Physical Sciences, National Research Council, Indications and Warning Technologies, in *Science and Technology for Army Homeland Security: Report 1*, National Academies Press, Washington, DC, 2003, ISBN: 9780309087018 ([http://www.nap.edu/openbook.php?record\\_id=10655](http://www.nap.edu/openbook.php?record_id=10655)).
- [3] International Workshop on Fast Neutron Detectors and Applications (FNDA2006), University of Capetown, South Africa, 2006, *Proceedings of Science (FNDA2006)* (<http://pos.sissa.it/cgi-bin/reader/conf.cgi?confid=25>).
- [4] 2nd International Workshop on Fast Neutron Detectors and Applications (FNDA2011), Kibbutz Ein Gedi, Israel, 2011, *Journal of Instrumentation* 7C (2012) (<http://iopscience.iop.org/1748-0221/focus/extra.proc19>).
- [5] *Proceedings from the Workshop on Neutron, Neutrino, Nuclear, Muon and Medical Physics at ESS, Lund, Sweden* ([http://www.hep.lu.se/staff/christian\\_sen/proceeding.pdf](http://www.hep.lu.se/staff/christian_sen/proceeding.pdf)), 2009.
- [6] R. Chandra, G. Davatz, U. Gendotti, A. Howard, *IEEE Nuclear Science Symposium and Medical Imaging Conference* (2010) 508. <http://dx.doi.org/10.1109/NSSMIC.2010.5873813>.
- [7] W.C. Lyons, G.J. Plisga, *Drilling and Well Completions, Reservoir Engineering*, in: *Standard Handbook of Petroleum and Natural Gas Engineering*, 2nd ed., Elsevier Science, Houston, TX, 2011, ISBN: 978-0-7506-7785-1.
- [8] R. Chandra, G. Davatz, H. Friederich, U. Gendotti, D. Murer, *Journal of Instrumentation* 7 (03) (2012) C03035. <http://dx.doi.org/10.1088/1748-0221/7/03/C03035>.
- [9] P. Peerani, A. Tomanin, S. Pozzi, J. Dolan, E. Miller, M. Flaska, M. Battaglieri, R. de Vita, L. Ficini, G. Ottonello, G. Ricco, G. Dermody, C. Giles, *Nuclear Instruments and Methods in Physics Research Section A* 696 (2012) 110. <http://dx.doi.org/10.1016/j.nima.2012.07.025>.
- [10] *Workshop on Fast Neutron Applications at Spallation Sources*, Abingdon, UK (<http://plone.esss.lu.se/>), 2013.
- [11] M.R. Islam, M.I. Khan, *Reservoir engineering and secondary recovery*, in: *The Petroleum Engineering Handbook: Sustainable Operations*, Elsevier Science, Houston, TX, 2013, ISBN: 9780127999838, (<http://books.google.com/books?id=xxijAQAQAQBA>).
- [12] J.L. Lewis, D. Raetz, D. Murer, K.A. Jordan, *Analysis for in-situ fission rate measurements using 4He gas scintillation detectors*, in: *3rd International Conference on Advancements in Nuclear Instrumentation Measurement Methods and their Applications*, Marseille, France, 2013, For mmc interref, use as under: <http://dx.doi.org/10.1109/ANIMMA.2013.6728031>.
- [13] A. Tomanin, J. Paepen, P. Schillebeeckx, R. Wynants, R. Nolte, A. Lavietes, *Nuclear Instruments and Methods in Physics Research Section A* 756 (2014) 45. <http://dx.doi.org/10.1016/j.nima.2014.03.028>.
- [14] J.M. Lewis, R.P. Kelley, D. Murer, K.A. Jordan, *Applied Physics Letters* 105 (2014) 014102. <http://dx.doi.org/10.1063/1.4887366>.
- [15] D.N. McKinsey, C.R. Brome, S.N. Dzhosyuk, R. Golub, K. Habicht, P.R. Huffman, E. Korobkina, S.K. Lamoreaux, C.E.H. Mattoni, A.K. Thompson, L. Yang, J.M. Doyle, *Physical Review A* 67 (2003) 062716. <http://dx.doi.org/10.1103/PhysRevA.67.062716>.
- [16] E. Aprile, A.E. Bolotinikov, A.I. Bolozdynya, T. Doko, *Scintillation detectors*, in: *Noble Gas Detectors*, Wiley-VCH Verlag GmbH, KGaA, Weinheim Germany, 2006, ISBN: 978-3-527-40597-8.
- [17] J.B. Birks, D.W. Fry, L. Costrell, K. Kandish, *The Theory and Practice of Scintillation Counting*, Pergamon Press, New York, U.S.A., 1964, ISBN: 978-0-08-010472-0.

- [18] G.F. Knoll, Radiation Detection and Measurement, Wiley, New York, U.S.A, 1989, ISBN: 9780471815044, (<http://books.google.com/books?id=dyBRAAAAMAAJ>).
- [19] B.A. Dolgosheim, B.U. Rodionov, The mechanism of noble gas scintillation, in: Elementary Particles and Cosmic Rays, vol. 2, Atomizdat, Moscow, Russia, 1969.
- [20] NE213 is no longer produced, Eljen Technologies offers EJ-301 (<http://www.eljentechnology.com/index.php/products/liquid-scintillators/71-ej-301>), while Saint Gobain offers BC-501 ([http://www.detectors.saint-gobain.com/uploadedFiles/SGdetectors/Documents/Product\\_Data\\_Sheets/BC501-501A-519-Data-Sheet.pdf](http://www.detectors.saint-gobain.com/uploadedFiles/SGdetectors/Documents/Product_Data_Sheets/BC501-501A-519-Data-Sheet.pdf)).
- [21] Supplied by High Tech Sources Limited, Unit 6, Moorbrook, Southmead, Industrial Estate, Didcot, Oxfordshire OX11 7HP, UK (<https://www.hightechsource.co.uk>).
- [22] Testing performed at National Physical Laboratory, Teddington, Middlesex TW11 0LW, UK, 24 January 2012.
- [23] (<http://www.hightechsource.co.uk/Legacy/Resources/Americium-Beryllium.pdf>) for details.
- [24] E.A. Lorch, International Journal of Applied Radiation and Isotopes 24 (1973) 585. [http://dx.doi.org/10.1016/0020-708X\(73\)90127-0](http://dx.doi.org/10.1016/0020-708X(73)90127-0).
- [25] A.D. Vijaya, A. Kumar, Nuclear Instruments and Methods in Physics Research 111 (1973) 435. [http://dx.doi.org/10.1016/0029-554X\(73\)90199-7](http://dx.doi.org/10.1016/0029-554X(73)90199-7).
- [26] A.A. Mowlavi, R. Koohi-Fayegh, Applied Radiation and Isotopes 60 (2004) 959. <http://dx.doi.org/10.1016/j.apradiso.2004.02.008>.
- [27] Zhenzhou Liu, Jinxiang Chen, Pei Zhu, Yongming Li, Guohui Zhang, Applied Radiation and Isotopes 65 (2007) 1318. <http://dx.doi.org/10.1016/j.apradiso.2007.04.007>.
- [28] ([http://www.laurussystems.com/products/products\\_pdf/LS\\_thermo\\_FH-40.pdf](http://www.laurussystems.com/products/products_pdf/LS_thermo_FH-40.pdf)).
- [29] Polytetrafluoroethylene, also known as Teflon ([http://www2.dupont.com/Teflon\\_Industrial/en\\_US/products/selection\\_guides/coatings.html](http://www2.dupont.com/Teflon_Industrial/en_US/products/selection_guides/coatings.html)).
- [30] D.N. McKinsey, C.R. Brome, J.S. Butterworth, S.N. Dzhosyuk, R. Golub, K. Habicht, P.R. Huffman, C.E.H. Mattoni, L. Yang, J.M. Doyle, Nuclear Instruments and Methods in Physics Research 516(2–3) (2004), 475.
- [31] (<http://www.hamamatsu.com/us/en/R580.html>).
- [32] (<http://www.eljentechnology.com/index.php/products/paints/87-ej-520>).
- [33] (<http://www.us.schott.com/borofloat/english/index.html>) for details. Supplied by Glasteknik i Emmaboda AB, Utvägen 6 SE-361 31 Emmaboda, Sweden.
- [34] Araldite is a registered trademark of Huntsman. See (<http://www.araldite2000plus.com>).
- [35] Viton is a registered trademark of DuPont Performance Elastomers LLC.
- [36] Poly(methyl-methacrylate), also known as acrylic, plexiglass, and Lucite. Supplied by Nordic Plastics Group AB, Bronsaxegatan 6, SE-213 75 Malmö, Sweden.
- [37] (<http://www.eljentechnology.com/index.php/products/pmma-a-uvt-material/102-light-guides>).
- [38] (<http://www.eljentechnology.com/index.php/products/paints/86-ej-510>).
- [39] (<http://www.et-enterprises.com/files/file/Pmtbrochure11.pdf>), for details.
- [40] Arktis Radiation Detectors Limited, 8045 Zürich, Switzerland; (<http://www.arktis-detectors.com>).
- [41] S. Ritt, Design and performance of the 6 GHz waveform digitizing chip DRS4, in: IEEE Nuclear Science Symposium Conference, NSS'08, October 2008, pp. 1512–1515.
- [42] H. Friederich, G. Davatz, U. Hartmann, A. Howard, H. Meyer, D. Murer, S. Ritt, N. Schlumpf, IEEE Transactions on Nuclear Science NS-58 (2011) 1652. <http://dx.doi.org/10.1109/TNS.2011.2159623>.
- [43] H.H. Knox, T.G. Miller, Nuclear Instruments and Methods in Physics Research 101 (1972) 519. [http://dx.doi.org/10.1016/0029-554X\(72\)90040-7](http://dx.doi.org/10.1016/0029-554X(72)90040-7).
- [44] S. Agostinelli, et al., Nuclear Instruments and Methods in Physics Research Section A 506 (2003) 250. [http://dx.doi.org/10.1016/S0168-9002\(03\)01368-8](http://dx.doi.org/10.1016/S0168-9002(03)01368-8).
- [45] J. Allison, et al., IEEE Transactions on Nuclear Science NS-53 (2006) 270. <http://dx.doi.org/10.1109/TNS.2006.869826>.
- [46] J. Scherzinger, J.R.M. Annand, G. Davatz, K.G. Fissum, U. Gendotti, R. Hall-Wilton, E. Håkansson, R. Jebali, K. Kanaki, M. Lundin, B. Nilsson, A. Rosborg, H. Svensson, Applied Radiation and Isotopes 98 (2015) 74. <http://dx.doi.org/10.1016/j.apradiso.2015.01.003>.



Paper III







Contents lists available at ScienceDirect

## Nuclear Instruments and Methods in Physics Research A

journal homepage: [www.elsevier.com/locate/nima](http://www.elsevier.com/locate/nima)

## The light-yield response of a NE-213 liquid-scintillator detector measured using 2–6 MeV tagged neutrons



J. Scherzinger<sup>a,b</sup>, R. Al Jebali<sup>c</sup>, J.R.M. Annand<sup>c</sup>, K.G. Fissum<sup>a,b,\*</sup>, R. Hall-Wilton<sup>b,d</sup>, K. Kanaki<sup>b</sup>, M. Lundin<sup>e</sup>, B. Nilsson<sup>b,e</sup>, H. Perrey<sup>a,b</sup>, A. Rosborg<sup>e</sup>, H. Svensson<sup>e,f</sup>

<sup>a</sup> Division of Nuclear Physics, Lund University, SE-221 00 Lund, Sweden

<sup>b</sup> Detector Group, European Spallation Source ERIC, SE-221 00 Lund, Sweden

<sup>c</sup> SUPA School of Physics and Astronomy, University of Glasgow, Glasgow G12 8QQ, Scotland, UK

<sup>d</sup> Mid-Sweden University, SE-851 70 Sundsvall, Sweden

<sup>e</sup> MAX IV Laboratory, Lund University, SE-221 00 Lund, Sweden

<sup>f</sup> Sweflo Engineering, SE-275 63 Blentarp, Sweden

### ARTICLE INFO

#### Keywords:

NE-213  
Gamma-rays  
Fast-neutrons  
Scintillations  
Pulse-shape discrimination

### ABSTRACT

The response of a NE-213 liquid-scintillator detector has been measured using tagged neutrons from 2 to 6 MeV originating from an Am/Be neutron source. The neutron energies were determined using the time-of-flight technique. Pulse-shape discrimination was employed to discern between gamma-rays and neutrons. The behavior of both the fast (35 ns) and the combined fast and slow (475 ns) components of the neutron scintillation-light pulses were studied. Three different prescriptions were used to relate the neutron maximum energy-transfer edges to the corresponding recoil-proton scintillation-light yields, and the results were compared to simulations. The overall normalizations of parametrizations which predict the fast or total light yield of the scintillation pulses were also tested. Our results agree with both existing data and existing parametrizations. We observe a clear sensitivity to the portion and length of the neutron scintillation-light pulse considered.

### 1. Introduction

Organic liquid scintillators are typically employed to detect fast neutrons in mixed neutron and gamma-ray fields. When exposed to these two different types of radiation, such scintillators emit light with dramatically different decay-time constants. Gamma-rays interact dominantly with the atomic electrons of the scintillator atoms. The freed electrons are almost minimum ionizing and produce very fast flashes of light (10 s of ns decay times). In contrast, neutrons interact dominantly with the hydrogen nuclei (and to a lesser extent, carbon nuclei) of the scintillator molecules via scattering. Only the hydrogen nuclei are given sufficient energy to produce a significant signal, and in the neutron energy range from 2 to 6 MeV, the recoiling protons are far from minimum ionizing and produce much slower flashes of light (100 s of ns decay times). By examining the time dependence of the scintillation-light intensity, differences in pulse shapes may be identified. Such pulse-shape discrimination (PSD) may be used to determine whether or not the incident radiation was a neutron or gamma-ray.

The organic liquid scintillator NE-213 [1] has been a popular

detector medium since its introduction in the early 1960 s [2]. It is a solution of aromatic molecules suspended in a xylene solvent.<sup>1</sup> The result is a flammable, corrosive, sharp-smelling liquid with a flash point of ~26 °C that poses a considerable health risk. Nevertheless, due to its strong gamma-ray rejection properties, which are facilitated by excellent PSD characteristics and high detection efficiency for fast neutrons, NE-213 (first three scintillation-light decay constants: 3.16, 32.3, and 270 ns) has long set the standard for organic liquid scintillators (and beyond). As a result, newly developed fast-neutron detectors are often compared to it [3–6].

We have recently reported on a technique for tagging neutrons emitted by actinide/Be-based radioactive sources [7]. In that paper, we also discuss in detail the experimental apparatus and technique employed here. In this paper, we present the results of our inaugural investigation performed using this neutron-tagging technique – a precision mapping of the response of a NE-213 liquid-scintillator detector using neutrons tagged from 2 to 6 MeV.

\* Corresponding author.

E-mail address: [kevin.fissum@nuclear.lu.se](mailto:kevin.fissum@nuclear.lu.se) (K.G. Fissum).

<sup>1</sup> More recent variants are based on a pseudo-cumene solvent. These variants are less flammable than the xylene-based original.

## 2. Apparatus

### 2.1. Actinide/Be-based source

An 18.5 GBq  $^{241}\text{Am}/^9\text{Be}$  (Am/Be) source was employed for the irradiations performed in this work. We note that the neutron-tagging technique described below will work equally well for any actinide/Be-based neutron source. Unwanted 60 keV gamma-rays associated with the  $\alpha$ -decay of  $^{241}\text{Am}$  were attenuated using a 3 mm thick Pb sheet. The source radiated  $(1.106 \pm 0.015) \times 10^6$  neutrons per second nearly isotropically [8]. Fast neutrons were produced when the  $\alpha$ -particles from the decay of  $^{241}\text{Am}$  interacted with the  $^9\text{Be}$ . These neutrons had a maximum energy of about 11 MeV [9]. Roughly 25% of the neutrons had energy less than 1 MeV [10]. If the recoiling  $^{12}\text{C}$  was left in its first excited state (about 55% of the time [10–12]), the freed neutron was accompanied by an isotropically radiated prompt 4.44 MeV de-excitation gamma-ray. The half-value layer (HVL) for 3.5 MeV gamma-rays in lead is 1.51 cm, and above this energy, the HVL does not increase with increasing gamma-ray energy. As a result, fewer than 20% of these 4.44 MeV gamma-rays were attenuated in the 3 mm Pb sleeve. Thus, the radiation field associated with the lead-shielded Am/Be source was to a large extent a combination of 4.44 MeV gamma-rays and their associated fast-neutrons.

### 2.2. NE-213 liquid-scintillator detector

Fig. 1 presents the NE-213 liquid-scintillator detector employed in this measurement. A 3 mm thick cylindrical aluminum cell 62 mm deep by 94 mm in diameter, coated internally with EJ-520  $\text{TiO}_2$ -based reflective paint [13], contained the NE-213. A 5 mm thick borosilicate glass plate [14], attached using Araldite 2000 + glue [15], served as an optical window. A pressurized nitrogen gas-transfer system was used to fill the cell with nitrogen-flushed NE-213, and Viton O-rings [16] were used to seal the filling penetrations. The filled cell was coupled to a cylindrical PMMA UVT lightguide [17] 57 mm long by 72.5 mm in diameter coated on the outside by EJ-510 [18]  $\text{TiO}_2$ -based reflector. The cell/lightguide assembly was attached to a spring-loaded,  $\mu$ -metal shielded 3 in. ET Enterprises 9821KB photomultiplier tube (PMT) and base [19]. Gain for the NE-213 detector was set using standard gamma-ray sources, resulting in an operating voltage of about  $-2000$  V. Typical signal risetime was 5 ns.

### 2.3. YAP(Ce) 4.44 MeV gamma-ray detectors

Fig. 2 presents a photograph of one of the YAP(Ce) gamma-ray detectors provided by Scionix [20] that was employed in this measurement. YAP(Ce) is an abbreviation for yttrium aluminum perovskite: cerium, or  $\text{YAlO}_3$ ,  $\text{Ce}^{3+}$  doped. YAP(Ce) is both radiation hard and relatively insensitive to fast neutrons. Each detector was composed of a cylindrical 1 in. long by 1 in. diameter crystal [21] attached to a 1 in. Hamamatsu Type R1924 PMT [22]. Gains for the YAP(Ce) detectors were set using standard gamma-ray sources with typical operating voltages of about  $-800$  V. Typical signal risetime was 5 ns. The energy resolution for the 662 keV peak of  $^{137}\text{Cs}$  measured using such a detector was about 10%. We stress that the YAP(Ce) detectors were not used for gamma-ray spectroscopy, but rather to count the 4.44 MeV gamma-rays emitted by the source and thus provide a reference in time for the corresponding emitted neutrons.

## 3. Measurement

### 3.1. Setup

Fig. 3 shows a simplified block diagram of the experimental setup. As previously mentioned, the Am/Be source was placed within a 3 mm thick Pb sleeve to attenuate the source-associated 60 keV gamma-rays.

Two YAP(Ce) detectors (for simplicity, only one is shown) were located about 5 cm from the Am/Be source at source height. The threshold for the YAP(Ce) detectors was about 350 keV<sub>ee</sub> (keV electron equivalent). The NE-213 detector was located 2.420 m from the Am/Be source and also at source height. The threshold for the NE-213 detector was about 250 keV<sub>ee</sub>. Both detectors triggered overwhelmingly on the source-associated 4.44 MeV gamma-rays corresponding to the decay of the first excited state of  $^{12}\text{C}$ , but they also registered a large number of 2.23 MeV gamma-rays associated with neutron capture on the hydrogen in the water and paraffin used as general radiation shielding (not shown in this simplified illustration). The NE-213 detector also triggered on the fast neutrons radiated from the source. By detecting both the fast neutron and the prompt correlated 4.44 MeV gamma-ray, neutron time-of-flight (TOF) and thus energy was determined. This neutron-tagging technique enabled the mapping of the response of the NE-213 cell to fast neutrons as a function of their kinetic energy. Note that due to the energy invested in the 4.44 MeV gamma-ray, the tagging technique restricted the maximum available tagged-neutron energies to about 6 MeV.

### 3.2. Electronics and data acquisition

The analog signals from the detectors were split and sent to LeCroy 2249A (DC-coupled short gate SG) and 2249W (AC-coupled long gate LG) CAMAC charge-to-digital converters (QDCs) and Phillips Scientific 715 NIM constant-fraction timing discriminators (CFDs). The discriminator logic signals were sent to LeCroy 4434 scalers and LeCroy 2228A CAMAC time-to-digital converters (TDCs). A CES 8210 branch driver was employed to connect the CAMAC electronics to a VMEbus and a SBS 616 PCI-VME bus adapter was used to connect the VMEbus to a LINUX PC-based data-acquisition (DAQ) system. The signals were recorded and processed using ROOT-based software [23]. Signals from the NE-213 detector were used to trigger the DAQ and also provided the start for the TOF TDC. As previously mentioned, the NE-213 detector QDCs included a 60 ns gated SG QDC and a 500 ns gated LG QDC, where in both cases, the gates opened 25 ns prior to the arrival of the analog pulse. The YAP(Ce) detector provided the stop signal for the TOF TDC. We were particularly interested in two source-related event types: (1) a fast neutron detected in the NE-213 detector (which started the TOF TDC) and the corresponding 4.44 MeV gamma-ray detected in the YAP(Ce) detector (which stopped the TOF TDC) and (2) a prompt, time-correlated gamma-ray pair detected one in the NE-213 detector and one in a YAP(Ce) detector (a gamma-flash event, see below). Such a pair of gamma-rays can result from, for example, the  $\alpha$  decay of  $^{241}\text{Am}$  to the higher excited states of  $^{237}\text{Np}$ .



Fig. 1. The NE-213 detector. Top: the scintillator “cup”. The optical boundary is provided by a borosilicate-glass window (light brown). Bottom: The gray cylinder to the left is the “cup”. The black cylinder to the right is the  $\mu$ -metal shielded PMT and base assembly. Figure from Ref. [6]. (For interpretation of the references to color in this figure caption, the reader is referred to the web version of this article.)



Fig. 2. Photograph of a YAP(Ce) detector. A cylindrical 1 in. long by 1 in. in diameter crystal (right) was coupled to 1 in. diameter PMT. Figure from Ref. [7].

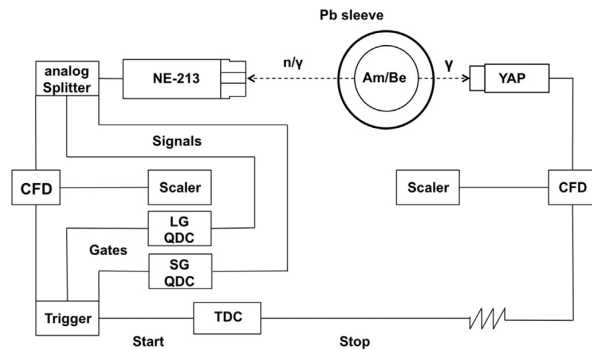


Fig. 3. A simplified schematic of the experimental setup. The Am/Be source, the Pb sleeve, a single YAP(Ce) detector, and the NE-213 detector are all shown together with a block electronics diagram. Figure from Ref. [7].

### 3.3. Energy calibration

Gamma-ray sources are typically used to calibrate organic scintillators as the light yield of the recoiling atomic electrons is linear above about 100 keV [24,25]. However, the low  $Z$  value typical of liquid scintillators means that gamma-ray interactions are dominated by Compton scattering at energies of a few MeV. Thus, resolution-broadened Compton edges must be carefully interpreted in order to calibrate the detector. Two different prescriptions to extract the Compton edge from a resolution-smear distribution have been reported by Flynn et al. [26] and Knox and Miller [24]. More recently, with the aid of Monte Carlo simulations, it has become generally accepted that the Compton edge lies somewhere between these prescriptions [27–30]. Apparently, no clear consensus exists.

We simulated the response of our detector to gamma-rays (and then neutrons, see below) using GEANT4 (version 10.00 patch2) with the standard electromagnetic-interaction package and hadronic physics list QGSP\_BERT\_HP which provided high-precision data-driven models for neutron interactions below 20 MeV [31,32]. The amplitude of the detector signal was provided by a sensitive-detector class which recorded the total energy deposited in the liquid-scintillator volume. The detector was defined to be the NE-213 filled cell together with the non-sensitive PMMA lightguide. For the purpose of the energy-calibration simulation, a point source of gamma-rays was positioned along the cylindrical symmetry axis of the cell at a distance of 1.5 cm from the face. The gamma-rays were directed onto the cell along its symmetry axis. Simulations of the deposited energy/scintillation-light yield for the detector were performed for the gamma-rays coming from  $^{22}\text{Na}$  (511 keV and 1274 keV) and  $^{137}\text{Cs}$  (662 keV), with corresponding Compton-edge-equivalent energies of 341 keV<sub>ee</sub>, 1062 keV<sub>ee</sub>, and 477 keV<sub>ee</sub>, respectively. A non-linear, energy-dependent parametrization of the detector resolution measured for gamma-ray energies between 0.5 MeV<sub>ee</sub> (18%) and 4.0 MeV<sub>ee</sub> (10%) was included in the simulation. Note that this exact same parametrization was used to

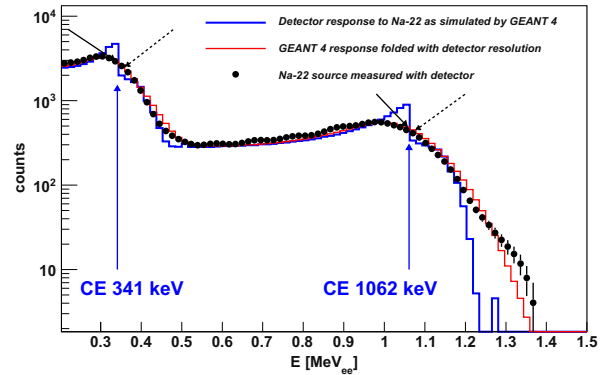


Fig. 4. Simulated Compton scattered recoil-electron distributions (blue and red histograms) together with data (black dots) for  $^{22}\text{Na}$  as a function of the deposited energy/scintillation-light yield in MeV<sub>ee</sub>. The blue histogram is the basic energy-deposition simulation which excludes energy resolution but clearly illustrates Compton edges at 341 keV<sub>ee</sub> and 1062 keV<sub>ee</sub>. The red histogram is the simulation including resolution effects. The black dots result from the subtraction of non-source-related background from the measured data. The angled solid black arrows indicate the locations of the Compton edges determined using the method of Knox and Miller [24], while the angled dashed black arrows indicate the locations of the Compton edges determined using the method of Flynn et al. [26]. (For interpretation of the references to color in this figure caption, the reader is referred to the web version of this article.)

smear the GEANT4-simulated detector response to produce resolution-corrected neutron scintillation-light yield spectra (see below).

Fig. 4 shows a representative comparison between the GEANT4 simulation of the response of the detector to the gamma-rays coming from a  $^{22}\text{Na}$  source and background-subtracted data obtained with a  $^{22}\text{Na}$  source. The blue histogram corresponds to the basic simulation of the deposited energy and does not include resolution effects but clearly illustrates the Compton edges at 341 keV<sub>ee</sub> and 1062 keV<sub>ee</sub>. The red histogram corresponds to the simulation including the non-linear parametrization of the energy-resolution effects detailed above. The black dots result from the subtraction of non-source-related background from the measured data. This included cosmic-ray background and experiment-hall background. The intensity of the cosmic-ray background was addressed with an energy-dependent exponential function, while the room background was addressed by identifying dominant gamma-rays present in data taken simultaneously with a HPGe detector. This background was then simulated as a combination of the dominant gamma-rays – specifically, from  $^{40}\text{K}$  (1460 keV),  $^{208}\text{Tl}$  (2614 keV, 583 keV, and 510 keV using the branching ratio 100:85:23) and 511 keV positron annihilation.<sup>2</sup> The overall agreement between the measured data and simulation is very good. We attribute the very small variations between 0.5 MeV<sub>ee</sub> and 1.0 MeV<sub>ee</sub> to room background which we did not address. The enhanced strength at 1.4 MeV may be due to the simultaneous detection of both the gamma-rays emitted by  $^{22}\text{Na}$ .

We compared the results of our simulations to the Compton-edge prescriptions suggested by Flynn et al. [26] (dashed black arrows in Fig. 4) and Knox and Miller [24] (solid black arrows in Fig. 4). When the Flynn et al. approach was taken, we found it to overpredict systematically the locations of the Compton edges by more than 10%. When the Knox and Miller approach was taken, we found it to underpredict systematically the locations of the Compton edges by less than 3%.

## 4. Results

As previously mentioned, gamma-ray scintillations in NE-213 are

<sup>2</sup> Unfortunately, a “source-free” data set was not available.

generally fast (10 s of ns decay times) while neutron scintillations are much slower (100 s of ns decay times). The type of radiation incident upon the NE-213 scintillator may thus be identified by examining the time structure of the scintillation pulses. We used the standard “tail-to-total” method [5,33,34]. **With this method, the difference in the integrated charge produced by the scintillation-light pulses in the LG and SG QDCs was normalized to the integrated charge produced by the scintillation-light pulse in the LG QDC according to**

$$PS = (LG - SG)/LG. \quad (1)$$

Fig. 5 presents TOF distributions acquired when the NE-213 reference detector started the TOF TDC and the YAP(Ce) detector stopped the TOF TDC. The top two panels have been presented and discussed in detail in Ref. [7] and are included here for completeness. The top panel illustrates that the separation between gamma-rays (recoiling electrons) and neutrons (recoiling protons) was excellent. In the middle panel, the data from the top panel have been projected onto the TOF axis. The  $\gamma$ -flash and fast-neutron distributions are clearly identified. The very low level of background consists of random events which included cosmic rays, room background, Am/Be neutrons not correlated with a 4.44 MeV gamma-ray, and Am/Be neutrons where the 4.44 MeV gamma-ray was missed due to YAP inefficiency or geometry. In the bottom panel, our previously detailed calibration was applied to the data and the resulting scintillation-light yield is displayed for the SG QDC. It is this scintillation-light yield which we now proceed to analyze in detail.

The neutron scintillation-light yield (due to recoiling protons) was determined by converting from TOF to neutron kinetic energy, binning in widths of 0.2 MeV, and filling the corresponding energy-calibrated SG and LG QDC spectra.  $T_0$  was determined from the location of the gamma-flash in the TOF spectra using the speed of light and measurements of the distances between the YAP(Ce) detector, the NE-213 detector, and the Am/Be source. The neutron path length employed in this measurement was 2.420 m. Based upon our 1.8 ns gamma-flash and the detector thickness of 6.2 cm, we determined our energy resolution to be 4% at 2 MeV and 5% at 4 MeV. If the TOF bin width is sufficiently small and there was no smearing due to energy-resolution effects, each of these spectra would demonstrate a sharp cutoff corresponding to the neutron transferring all of its energy to the

recoiling proton. In our detector, resolution effects smeared this maximum-transfer edge. Further, as in the case for locating the Compton edge for the energy calibration of organic scintillators with gamma-ray sources, there is no single prescription for relating the maximum proton energy to the resolution-smeared maximum-transfer edge. Thus, for each energy bin, we have investigated three edge-determination prescriptions:

1. As suggested by Naqvi et al. [35], a Gaussian function was fitted to the high-energy edge of the recoil-proton energy distribution and the maximum-transfer edge was taken to be the half-height (HH) position.
2. As suggested by Kornilov et al. [36], the location of the most energetic minimum in the first derivative (FD) of the recoil-proton energy distribution was associated with the maximum-transfer edge.
3. The maximum-transfer edge was taken as the turning point (TP) of the Gaussian function fitted to the resolution-smeared edge. Note that if the fitted Gaussian function described the resolution-smeared maximum-transfer edge perfectly, then the location of its TP is by definition identical to the minimum in the first derivative of the recoil-proton energy distribution.

In each investigation, the non-linear correspondence between recoiling electron ( $E_e$ ) and recoiling proton ( $E_p$ ) scintillation light-yield has been represented in two ways:

$$E_e = L_0 \frac{E_p^2}{E_p + L_1} \quad (2)$$

$$E_e = C \{0.83E_p - 2.82[1 - \exp(-0.25E_p^{0.93})]\} \quad (3)$$

Eq. (2) is the same as Eq. (4) given in Ref. [36], where  $L_0$  and  $L_1$  are adjustable parameters, and Eq. (3) is from Ref. [37], where  $C$  is an adjustable parameter.

Fig. 6 compares the GEANT4-simulated and measured neutron scintillation-light yield (due to recoiling protons) in the LG QDC for neutrons having  $(5.0 \pm 0.1)$  MeV kinetic energy (TOF  $\sim 22$  ns). In the GEANT4 simulation, the light-yield parametrization presented in Eq. (2) (see below for a discussion of light-yield parametrizations for NE-

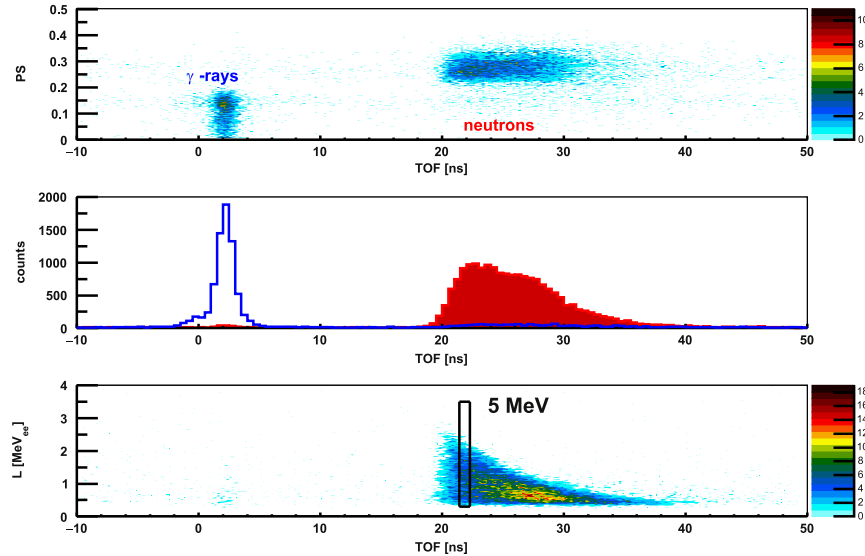


**Fig. 5.** Time-of-flight (TOF) distributions obtained for a neutron-drift distance of 0.675 m. Top panel: pulse shape (PS) plotted against TOF. Middle panel: projection of the data from the top panel onto the TOF axis. A  $PS = 0.19$  cut has been applied to separate gamma-rays and neutrons. The unshaded blue peak corresponds to  $PS < 0.19$  while the shaded red distribution corresponds to  $PS > 0.19$ . Bottom panel: scintillation-light yield ( $L$ ) plotted against TOF for  $PS > 0.19$ . The cut to select neutrons with energy  $(5.0 \pm 0.1)$  MeV (TOF  $\sim 22$  ns) is indicated with a black box. (For interpretation of the references to color in this figure caption, the reader is referred to the web version of this article.)

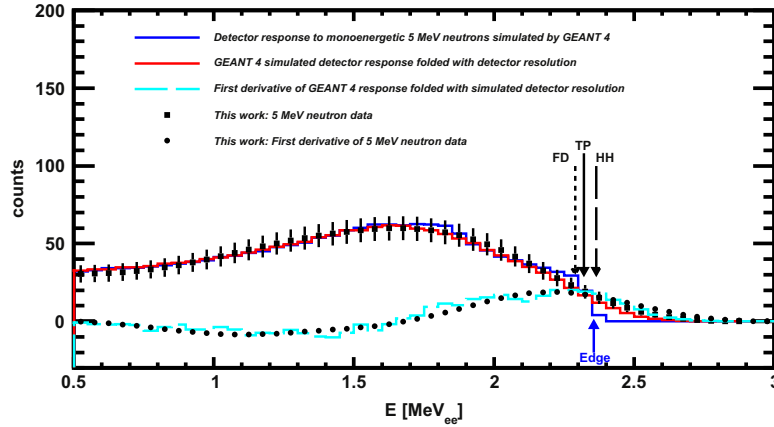


**Fig. 6.** Simulated and measured neutron scintillation-light yield for  $(5.0 \pm 0.1)$  MeV neutrons. The solid blue histogram shows the GEANT4-simulated detector response without resolution effects and the solid red histogram shows the GEANT4-simulated detector response folded with the measured detector resolution. The simulated maximum-transfer edge is clearly indicated. The dashed cyan histogram corresponds to the first derivative of the red histogram. Filled black squares correspond to measured data (statistical uncertainties are shown) and filled black circles correspond to the locations of the 5 MeV maximum-transfer edge according to the FD (short dash), TP (solid), and HH (long dash) prescriptions. (For interpretation of the references to color in this figure caption, the reader is referred to the web version of this article.)

213) has been employed, where parameter  $L_1$  was fixed at the Kornilov et al. [36] value of 2.47. The light-yield scaling (parameter  $L_0$ ) was first based on the HH method for positioning the maximum-transfer edge (see the red curve at 5 MeV in the top panel of Fig. 7). The simulated detector response is shown without resolution effects, and the location of the maximum-transfer edge may be observed at about 2.36 MeV<sub>ee</sub>.

As the degree of smearing of the simulated detector response due to energy-resolution effects affects the location of the maximum-transfer edge in the simulated detector response predicted by the various prescriptions, the non-linear energy-dependent parametrization of the detector resolution measured for gamma-ray energies between 0.5 MeV<sub>ee</sub> and 4.0 MeV<sub>ee</sub> that we employed in our calibration efforts

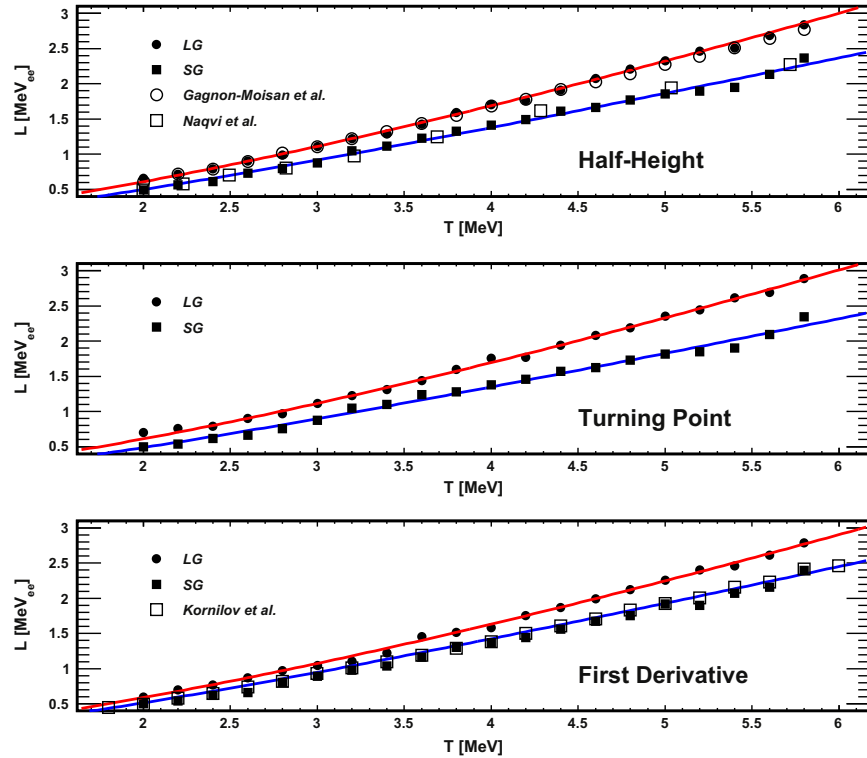


**Fig. 7.** LG (filled black circles) and SG (filled black squares) neutron scintillation-light yield (due to recoiling protons) as a function of neutron kinetic energy for different maximum-transfer edge determinations together with the data of Gagnon-Moisan et al. [38] (top panel, open circles), Naqvi et al. [35] (top panel, open squares), and Kornilov et al. [36] (bottom panel, open squares). The red curves are Eq. (2) fitted to the LG distributions while the blue curves are Eq. (3) fitted to the SG distributions. (For interpretation of the references to color in this figure caption, the reader is referred to the web version of this article.)

**Table 1**

Scale factors  $L_0$  and  $C$  from fits of Eqs. (2) and (3) to the present LG and SG data together with ratios. “Edge” denotes the method used to determine the maximum-energy edge of the recoil-proton scintillation-light yield.

Data	Edge	$L_0$ (from Eq. (2))	$\chi^2$ /d.o.f	$C$ (from Eq. (3))	$\chi^2$ /d.o.f.
LG	HH	$0.704 \pm 0.006$	0.86	$1.056 \pm 0.009$	1.20
SG	HH	$0.555 \pm 0.005$	0.98	$0.828 \pm 0.007$	1.10
SG/LG	HH	$0.789 \pm 0.010$		$0.784 \pm 0.009$	
LG	TP	$0.702 \pm 0.006$	1.37	$1.044 \pm 0.010$	1.41
SG	TP	$0.543 \pm 0.005$	1.27	$0.810 \pm 0.007$	1.29
SG/LG	TP	$0.774 \pm 0.010$		$0.776 \pm 0.010$	
LG	FD	$0.689 \pm 0.005$	1.05	$1.037 \pm 0.005$	0.74
SG	FD	$0.539 \pm 0.005$	1.19	$0.813 \pm 0.005$	0.82
SG/LG	FD	$0.783 \pm 0.010$		$0.784 \pm 0.006$	

was again employed to accurately smear the simulated detector response. The simulated detector response with resolution effects is also shown. The arrows indicate the locations of the maximum-transfer edge in the data according to the FD (2.29 MeV<sub>ee</sub>), TP (2.32 MeV<sub>ee</sub>), and HH (2.36 MeV<sub>ee</sub>) prescriptions. As expected, when the HH evaluation of the data is compared to the simulation with HH-based scaling, the agreement is essentially exact. The average location of the 5 MeV maximum-transfer edge is 2.33 MeV<sub>ee</sub>, and all three predictions based upon the data agree to about 1%. For these same 5 MeV neutrons, with the HH method for positioning the maximum-transfer edge fixed, we then varied the light-yield scaling in the GEANT4 simulation to the values obtained using the TP and FD prescriptions (see the red curves at 5 MeV in the middle and bottom panels of Fig. 7). In all three cases, the GEANT4 simulations were very close to the data up to 2 MeV<sub>ee</sub>, with the FD and TP results lying at most 5% and 3% respectively above the HH results. Above 2 MeV<sub>ee</sub>, comparison was difficult due to a combination of lack of statistics and resolution effects. For simulated (4.0 ± 0.1) MeV neutrons, light-yield scaling factors derived from all three methods resulted in a constant 8% overestimation of the location of the maximum-transfer edges extracted from the data according to the procedure described above. At (3.0 ± 0.1) MeV the difference between the simulation-predicted and data-extracted edge location for the HH prescription remained at an 8% overestimation, while for the TP and FD prescriptions, the discrepancy increased to 12% and 18%, respectively. At lower energies, the degree of non-linearity of the recoil-proton scintillation-light yield increases and this may account for the increasing discrepancy. Note that the use of Eq. (3) gives very similar results from 3 to 5 MeV.

Fig. 7 shows neutron scintillation-light yield (due to recoiling protons) data, as a function of neutron kinetic energy, for the three different maximum-transfer edge determinations together with existing results. The statistical uncertainties in our data are smaller than the point size. Gagnon-Moisan et al. [38] used a PS digitizer and employed a gamma-ray energy calibration similar to that of Ref. [24]. The tail-to-total method was used in their analysis together with the HH prescription for determining the maximum-transfer edge. Their data agree well with our corresponding LG results and we note that the method they used to integrate the total charge produced by the scintillation light is very similar to that employed here. Naqvi et al. [35] used ADCs (which we believe were peak-sensing) and employed the gamma-ray energy calibration suggested in Ref. [24]. The HH prescription was used for determining the maximum-transfer edge. Their data agree well with our corresponding SG results, but it is not possible to determine how much of the scintillation-light pulse was integrated from Ref. [35]. Kornilov et al. [36] used a charge-sensitive preamp together with an Ortec 460 delay-line amplifier and peak-sensing ADCs. Again, it is difficult to quantify how much of the scintillation pulse was integrated when the light yield was measured. “Standard” (unspecified) gamma-ray energy calibrations were employed and the FD prescription was used to determine the max-

imum-transfer edge. Again their data agree well with our corresponding SG results.

Thus, the results from Refs. [35,36], which used similar measurement techniques, are both in good agreement with our SG results. This could indicate that in these works, the entire charge associated with the scintillation was not integrated. On the other hand, real differences in the behavior of different samples of NE-213 are entirely possible and were observed in Ref. [36].

In Fig. 7, the red curves shown in each panel display the scintillation-light yield parametrization described by Eq. (3) fitted to the present LG data, while the blue curves display the scintillation-light yield parametrization described by Eq. (2) fitted to the SG data. In each case, the overall scale of the fitted function was allowed to float (see below). Note that when the fitted functions employed were interchanged (that is, when Eq. (3) was fitted to our SG data and Eq. (2) was fitted to our LG data) the quality of fit was as good. This is not surprising as the scaled parametrizations differ by only about 3% over this energy range.

Table 1 presents the scale factors (parameter  $L_0$  of Eq. (2) and parameter  $C$  of Eq. (3)) obtained by fitting parametrizations to the recoil-proton scintillation-light yield data obtained with the LG and SG QDCs. For Eq. (2), parameter  $L_1$  was fixed at a value 2.47. In each case, the HH, TP, and FD prescriptions for determining the location of the maximum-transfer edge have been employed, and 20 data points between 2 and 6 MeV were considered.

There is little to choose between the  $\chi^2$ /d.o.f. values which are all close to 1. Further, the ratios of scale parameters for the SG and LG data do not differ significantly between any of the edge-determination prescriptions or between the use of Eq. (2) or Eq. (3) for the correspondence between the recoiling electron and recoiling proton scintillation-light yield. Comparing the present LG values of  $L_0$  with those presented in Ref. [36] where a similar value of  $L_1$  was used, our values are a factor  $\sim 1.2$  higher. Thus, compared to Ref. [36], we have collected a factor 1.2 more recoil-proton scintillation. On the other hand, from the values of  $C$  presented in Table 1 which are only a few percent above 1, it can be seen that our results are quite similar to those presented in Ref. [37] and close to those presented in Ref. [38].

## 5. Summary and discussion

We have reported a detailed mapping of the response of a NE-213 detector to neutrons from 2 to 6 MeV emitted by a lead-shielded Am/Be source and subsequently tagged by time-correlated gamma-ray emission. Neutron/gamma pulse-shape discrimination was performed using the gated tail-to-total QDC method, with charge-integration periods set to 35 ns and 475 ns. The electron-energy calibration was performed using standard gamma-ray sources and two prescriptions for locating the corresponding Compton edges were examined. The results were compared to GEANT4 simulations which considered both energy-resolution effects and backgrounds. The Compton-edge prescriptions of Knox and Miller [24] and Flynn et al. [26] differ by more than 10% when applied to our data. The present GEANT4 simulations suggest that the former underpredicts the actual edge position by  $\sim 3\%$ , while the latter overpredicts by  $\sim 10\%$ . Consequently, we used the prescription of Knox and Miller [24] scaled up by a factor 1.03.

The present neutron-tagging technique provided a continuous, polychromatic, energy-tagged neutron beam from 2 to 6 MeV. Neutron kinetic energy was determined by measuring the neutron TOF relative to the prompt 4.44 MeV gamma-ray associated with the  $\alpha + {}^9\text{Be} \rightarrow n + {}^{12}\text{C}^*$  process. Using this information, recoil-proton scintillation-light yields were determined as a function of neutron kinetic energy. Three different prescriptions were employed for identifying the maximum energy-transfer edge of the recoiling protons in accumulated neutron scintillation-light spectra. Two parametrizations (Eqs. (2), (3)) of the recoil-proton scintillation-light yield were investigated. Simple scaling factors allowed for variations in the neutron scintillation-light

yield, and after scaling, either parametrization fitted our LG and SG data equally well.

GEANT4 was also used to study the effects of the three prescriptions for the determination of the recoil-proton edge in the neutron scintillation light-yield spectra. For a fixed light-yield parametrization, we varied the prescription between HH, TP, and FD (both with and without energy-resolution effects) for 3, 4, and 5 MeV neutrons. At 5 MeV, simulation and analysis agreed for all prescriptions at the 1% level. At 4 MeV, all three GEANT4 predictions for the maximum-transfer edge overestimated the location of the maximum-transfer edge extracted from the data by 8%. At 3 MeV, the difference between the edge locations extracted from the simulation and data for the HH prescription remained at 8%, while for the TP and FD prescriptions, the difference increased to 12% and 18%, respectively. A possible cause of the discrepancy is an incomplete consideration of increasing quenching of the scintillation as  $dE/dx$  increases along the track of the recoiling proton. This will be investigated in future work. Nevertheless, the HH method produced the best results for our detector over our energy range.

The present results indicate that for recoiling protons in the present energy range,  $\sim 78\%$  (see Table 1) of the total integrated scintillation intensity (integration period 475 ns) is contained with the first 35 ns of the signal. Comparing the total light yield (LG) to previous measurements, the present results are in good agreement with those of Gagnon-Moisan et al. [38] and within a few percent of those of Cecil et al. [37], the latter of which often used to estimate recoil-proton scintillation-light output in the absence of a calibration. The present LG results are higher by a factor  $\sim 1.2$  compared to those of Kornilov et al. [36] and Naqvi et al. [35]. These previous measurements yield results which are actually close to our SG results (integration period 35 ns), but it is impossible to say if this discrepancy is due to a difference in effective integration times as the pulse-processing method was different. At least part of the discrepancy could be due to real differences in the response of the liquid scintillator. Factors such as concentration of the active scintillant/fluorescent materials in the base solvent and the presence of dissolved oxygen will affect the relative recoiling proton-to-electron scintillation-light yields. Indeed, it would seem that a dedicated measurement of the recoil-proton scintillation-light yield must be made on a case-by-case basis to obtain the best accuracy in precision neutron measurements.

The present measurements have been made at a new neutron test facility recently installed at Lund University [7]. This facility is being used to measure the characteristics of neutron detectors as part of the program to build the European Spallation Source. Development and extension of this facility is ongoing with a view to precisely determining the response of many materials to neutrons ranging in energies from fast to thermal.

## Acknowledgments

We thank the Photonuclear Group at the MAX IV Laboratory for providing access to their experimental hall and Am/Be source. We acknowledge the support of the UK Science and Technology Facilities Council (Grant nos. STFC 57071/1 and STFC 50727/1) and the European Union Horizon 2020 BrightNESS Project, Proposal ID 676548.

## References

- [1] Eljen Technologies EJ-301 (<http://www.eljentechnology.com/index.php/products/liquid-scintillators/71-ej-301>), Saint Gobain BC-501 ([http://www.detectors.saint-gobain.com/uploadedFiles/SGdetectors/Documents/Product\\_Data\\_Sheets/BC501-501A-519-Data-Sheet.pdf](http://www.detectors.saint-gobain.com/uploadedFiles/SGdetectors/Documents/Product_Data_Sheets/BC501-501A-519-Data-Sheet.pdf)).
- [2] R. Batchelor, et al., Nucl. Instrum. Methods 13 (1961) 70. [http://dx.doi.org/10.1016/0029-554X\(61\)90171-9](http://dx.doi.org/10.1016/0029-554X(61)90171-9).
- [3] E. Bayat, et al., Rad. Phys. Chem. 81 (2012) 217. <http://dx.doi.org/10.1016/j.radphyschem.2011.10.016>.
- [4] J. Iwanowska, et al., Nucl. Instrum. Methods Phys. Res. A 781 (2013) 44. <http://dx.doi.org/10.1016/j.nima.2013.01.064>.
- [5] I.A. Pawelczak, et al., Nucl. Instrum. Methods Phys. Res. A 711 (2013) 21. <http://dx.doi.org/10.1016/j.nima.2013.01.028>.
- [6] R. Al Jebali, et al., Nucl. Instrum. Methods Phys. Res. A 794 (2015) 102. <http://dx.doi.org/10.1016/j.nima.2015.04.058>.
- [7] J. Scherzinger, et al., Appl. Radiat. Isot. 98 (2015) 74. <http://dx.doi.org/10.1016/j.apradiso.2015.01.003>.
- [8] Testing performed at National Physical Laboratory, Teddington, Middlesex, UK TW11 0LW on 24 January 2012.
- [9] E.A. Lorch, J. Int. Appl. Radiat. Isot. 24 (1973) 585. [http://dx.doi.org/10.1016/0020-708X\(73\)90127-0](http://dx.doi.org/10.1016/0020-708X(73)90127-0).
- [10] A.D. Vijaya, A. Kumar, Nucl. Instrum. Methods 111 (1973) 435. [http://dx.doi.org/10.1016/0029-554X\(73\)90199-7](http://dx.doi.org/10.1016/0029-554X(73)90199-7).
- [11] A.A. Mowlavi, R. Koohi-Fayegh, Appl. Radiat. Isot. 60 (2004) 959. <http://dx.doi.org/10.1016/j.apradiso.2004.02.008>.
- [12] Zhenzhou Liu, et al., Appl. Radiat. Isot. 65 (2007) 1318. <http://dx.doi.org/10.1016/j.apradiso.2007.04.007>.
- [13] (<http://www.eljentechnology.com/index.php/products/paints/87-ej-520>).
- [14] (<http://www.us.schott.com/borofloat/english/index.html>) for details. Supplied by Glasteknik i Emmaboda AB, Utvägen 6 SE-361 31 Emmaboda, Sweden.
- [15] Araldite is a registered trademark of Huntsman. See (<http://www.araldite2000plus.com>).
- [16] Viton is a registered trademark of DuPont Performance Elastomers LLC.
- [17] Poly-methyl-methacrylate, also known as PMM, acrylic, plexiglass, and lucite. Supplied by Nordic Plastics Group AB, Bronsyxegatan 6, SE-213 75 Malmö, Sweden.
- [18] (<http://www.eljentechnology.com/index.php/products/paints/86-ej-510>).
- [19] (<http://www.et-enterprises.com/files/file/Pmtbrochure11.pdf>) for details.
- [20] Scionix Holland BV (<http://www.scionix.nl>).
- [21] M. Moszyński, et al., Nucl. Instrum. Methods Phys. Res. A 404 (1998) 157. [http://dx.doi.org/10.1016/S0168-9002\(97\)01115-7](http://dx.doi.org/10.1016/S0168-9002(97)01115-7).
- [22] Hamamatsu Photonics (<http://www.hamamatsu.com>).
- [23] R. Brun, F. Rademakers, Nucl. Instrum. Methods Phys. Res. A 389 (1997) 81–86 (See also (<http://root.cern.ch/>)).
- [24] H.H. Knox, T.G. Miller, Nucl. Instrum. Methods 101 (1972) 519. [http://dx.doi.org/10.1016/0029-554X\(72\)90040-7](http://dx.doi.org/10.1016/0029-554X(72)90040-7).
- [25] G.F. Knoll, Radiation Detection and Measurement, Wiley, New York, U.S.A., 1989 (ISBN: 9780471815044).
- [26] K.F. Flynn, et al., Nucl. Instrum. Methods 27 (1964) 13. [http://dx.doi.org/10.1016/0029-554X\(64\)90129-6](http://dx.doi.org/10.1016/0029-554X(64)90129-6).
- [27] L.E. Beghian, et al., Nucl. Instrum. Methods 35 (1965) 34. [http://dx.doi.org/10.1016/0029-554X\(65\)90004-2](http://dx.doi.org/10.1016/0029-554X(65)90004-2).
- [28] G. Dietze, H. Klein, Nucl. Instrum. Methods 193 (1982) 549. [http://dx.doi.org/10.1016/0029-554X\(82\)90249-X](http://dx.doi.org/10.1016/0029-554X(82)90249-X).
- [29] F. Arneodo, et al., Nucl. Instrum. Methods Phys. Res. A 418 (1998) 285. [http://dx.doi.org/10.1016/S0168-9002\(98\)00679-2](http://dx.doi.org/10.1016/S0168-9002(98)00679-2).
- [30] C. Matei, et al., Nucl. Instrum. Methods Phys. Res. A 676 (2012) 135. <http://dx.doi.org/10.1016/j.nima.2011.11.076>.
- [31] S. Agostinelli, et al., Nucl. Instrum. Methods Phys. Res. A 506 (2003) 250. [http://dx.doi.org/10.1016/S0168-9002\(03\)01368-8](http://dx.doi.org/10.1016/S0168-9002(03)01368-8).
- [32] J. Allison, et al., IEEE Trans. Nucl. Sci. 53 (2006) 270. <http://dx.doi.org/10.1109/TNS.2006.869826>.
- [33] A. Jhingan, et al., Nucl. Instrum. Methods Phys. Res. A 585 (2008) 165. <http://dx.doi.org/10.1016/j.nima.2007.11.013>.
- [34] A. Lavagno, et al., Nucl. Instrum. Methods Phys. Res. A 617 (2010) 492. <http://dx.doi.org/10.1016/j.nima.2009.10.111>.
- [35] A.A. Naqvi, et al., Nucl. Instrum. Methods Phys. Res. A 353 (1994) 156. [http://dx.doi.org/10.1016/0168-9002\(94\)91626-8](http://dx.doi.org/10.1016/0168-9002(94)91626-8).
- [36] N.V. Kornilov, et al., Nucl. Instrum. Methods Phys. Res. A 599 (2009) 226. <http://dx.doi.org/10.1016/j.nima.2008.10.032>.
- [37] R.A. Cecil, et al., Nucl. Instrum. Methods 161 (1979) 439. [http://dx.doi.org/10.1016/0029-554X\(79\)90417-8](http://dx.doi.org/10.1016/0029-554X(79)90417-8).
- [38] F. Gagnon-Moisan, et al., in: 2nd International Workshop on Fast Neutron Detectors and Applications (FNDA2011), Ein Gedi, Israel, 2011, <http://dx.doi.org/10.1088/1748-0221/7/03/C03023>

[1] Eljen Technologies EJ-301 (<http://www.eljentechnology.com/index.php/products/>



Paper IV





# A comparison of untagged gamma-ray and tagged-neutron yields from $^{241}\text{AmBe}$ and $^{238}\text{PuBe}$ sources

J. Scherzinger<sup>a,b</sup>, R. Al Jebali<sup>c</sup>, J.R.M. Annand<sup>c</sup>, K.G. Fissum<sup>a,b,\*</sup>,  
R. Hall-Wilton<sup>b,d</sup>, S. Koufigar<sup>a,1</sup>, N. Mauritzson<sup>a</sup>, F. Messi<sup>a</sup>, H. Perrey<sup>a,b</sup>,  
E. Rofors<sup>a</sup>

<sup>a</sup>*Division of Nuclear Physics, Lund University, SE-221 00 Lund, Sweden*

<sup>b</sup>*Detector Group, European Spallation Source ESS AB, SE-221 00 Lund, Sweden*

<sup>c</sup>*SUPA School of Physics and Astronomy, University of Glasgow, Glasgow G12 8QQ,  
Scotland, UK*

<sup>d</sup>*Mid-Sweden University, SE-851 70 Sundsvall, Sweden*

---

## Abstract

Untagged gamma-ray and tagged-neutron yields from  $^{241}\text{AmBe}$  and  $^{238}\text{PuBe}$  mixed-field sources have been measured. Gamma-ray spectroscopy measurements from 1 – 5 MeV were performed in an open environment using a  $\text{CeBr}_3$  detector and the same experimental conditions for both sources. The shapes of the distributions are very similar and agree well with previous data. Tagged-neutron measurements from 2 – 6 MeV were performed in a shielded environment using a NE-213 liquid-scintillator detector for the neutrons and a YAP(Ce) detector to tag the 4.44 MeV gamma-rays associated with the de-excitation of the first excited state of  $^{12}\text{C}$ . Again, the same experimental conditions were used for both sources. The shapes of these distributions are also very similar and agree well with previous data, each other, and the ISO recommendations. Our  $^{238}\text{PuBe}$  source provides approximately 2.4 times more tagged neutrons over the tagged-neutron energy range, in reasonable agreement with the original full-spectrum source-calibration measurements performed at the time of

---

\*Corresponding author. Telephone: +46 46 222 9677; Fax: +46 46 222 4709

Email address: [kevin.fissum@nuclear.lu.se](mailto:kevin.fissum@nuclear.lu.se) (K.G. Fissum)

<sup>1</sup>present address: Applied Physics and Applied Mathematics Department, Columbia University, New York, NY 10027, USA

their acquisition.

*Keywords:* americium-beryllium, plutonium-beryllium, gamma-rays, fast neutrons, time-of-flight, pulse-shape discrimination, NE-213, cerium-bromide

---

## 1. Introduction

Actinide/Be-based radioactive sources are typically used for cost-effective fast-neutron irradiations. Neutrons are produced when the  $\alpha$ -particle from the decay of the actinide interacts with the  ${}^9\text{Be}$  nucleus. If one is only interested in neutrons, a major drawback associated with these sources is the gamma-ray field produced by the original actinide. Higher-energy gamma-rays are also produced via the  $\alpha + {}^9\text{Be} \rightarrow \text{n} + {}^{12}\text{C}^*$  reaction. However, if detected, these 4.44 MeV gamma-rays can be used to “tag” the corresponding neutrons [1], resulting in a polychromatic energy-tagged neutron beam. In this paper, we employ the neutron-tagging technique to measure tagged, fast-neutron yields from  ${}^{241}\text{AmBe}$  and  ${}^{238}\text{PuBe}$  using a NE-213 liquid-scintillator detector. We also measure the corresponding untagged gamma-ray yields using a Cerium-bromide ( $\text{CeBr}_3$ ) detector. Our goal was to measure the tagged-neutron yields provided by the two sources and identify which of the two sources provided the higher tagged-neutron yield.

## 2. Apparatus

### 2.1. Actinide/Be-based sources

For the investigations performed in this work, both  ${}^{241}\text{Am}/{}^9\text{Be}$  (Am/Be) and  ${}^{238}\text{Pu}/{}^9\text{Be}$  (Pu/Be) sources were employed. Both actinides decay predominantly via the emission of  $\alpha$ -particles. According to NuDat [2],  ${}^{241}\text{Am}$  decays via the emission of 25 different  $\alpha$ -particles (5.4786 MeV weighted-mean energy) while  ${}^{238}\text{Pu}$  decays via the emission of 14 different  $\alpha$ -particles (5.4891 MeV weighted-mean energy). The difference in the weighted mean  $\alpha$ -particle energies is thus only about 10 keV. When these  $\alpha$ -particles interact with  ${}^9\text{Be}$ , fast neutrons are produced. Because the weighted mean of the incident  $\alpha$ -particle energies



Figure 1: The detectors employed for the measurements presented in this paper. From the left: NE-213 liquid-scintillator neutron and gamma-ray detector;  $\text{CeBr}_3$  gamma-ray spectroscopy detector; YAP(Ce) gamma-ray trigger detector.

is essentially the same for both actinides, the energy spectra of emitted neutrons are anticipated to demonstrate strong similarities. These neutrons have a maximum energy of about about 11 MeV [3]. If the recoiling  $^{12}\text{C}$  is left in its first excited state, the freed neutron is accompanied by an isotropically radiated prompt 4.44 MeV de-excitation gamma-ray. The radiation fields associated with these sources are thus a combination of the gamma-ray field associated with the original actinide together with 4.44 MeV gamma-rays and their associated fast-neutrons. Our Am/Be source radiates approximately  $1.14 \times 10^6$  neutrons per second [4], while our Pu/Be source radiates approximately  $2.99 \times 10^6$  neutrons per second [5], both nearly isotropically.

## 2.2. Detectors

The NE-213 liquid-scintillator and YAP(Ce) and  $\text{CeBr}_3$  gamma-ray detectors used in the measurements used for this work are shown in Fig. 1.

### *2.2.1. NE-213 liquid-scintillator detector*

NE-213 [6] is a standard organic liquid scintillator which has been employed for several decades for detecting neutrons in strong gamma-ray fields. Because gamma-ray induced scintillations in NE-213 are generally fast (10s of ns decay times) while neutron induced scintillations are much slower (100s of ns decay times), the type of radiation incident upon the NE-213 scintillator may be identified by examining the time structure of the scintillation pulses. The pseudocumene-based NE-213 liquid-scintillator detector employed in this measurement consisted of a 3 mm thick cylindrical aluminum cell (62 mm long  $\times$  94 mm  $\varnothing$ ) coated internally with EJ-520 TiO<sub>2</sub>-based reflective paint [7] which contained the NE-213. A 5 mm thick borosilicate glass plate [8] was used as an optical window. The filled cell was coupled to a cylindrical PMMA UVT lightguide [9] (57 mm long  $\times$  72.5 mm  $\varnothing$ ) coated on the outside by EJ-510 [10] TiO<sub>2</sub>-based reflective paint. The assembly was coupled to a  $\mu$ -metal shielded 3 in. ET Enterprises 9821KB photomultiplier tube (PMT) and base [11]. Operating voltage was set at about  $-1900$  V, and the energy calibration was determined using standard gamma-ray sources together with a slightly modified version of the method of Knox and Miller [12]. See Refs. [1, 13] for more detail.

### *2.2.2. YAP(Ce) 4.44 MeV gamma-ray detectors*

The YAP(Ce) (YAlO<sub>3</sub>, Ce<sup>+</sup> doped) gamma-ray detectors employed in this measurement were provided by Scionix [14]. Each detector was comprised of a cylindrical (2.54 cm long  $\times$  2.54 cm  $\varnothing$ ) crystal [15] attached to 2.54 cm Hamamatsu Type R1924 PMT [16]. YAP(Ce) is a useful gamma-ray trigger scintillator in a strong radiation field as it is both radiation hard and relatively insensitive to fast neutrons. Operating voltage was set at about  $-800$  V, and energy calibration was determined using standard gamma-ray sources. These YAP(Ce) detectors were used to count the 4.44 MeV gamma-rays emanating from the sources and thus tag the corresponding emitted neutrons. See Refs. [1, 13] for more detail.

### 2.2.3. *CeBr<sub>3</sub> gamma-ray detector*

The CeBr<sub>3</sub> gamma-ray detector employed in this measurement was provided by Scionix [14]. The detector was comprised of a cylindrical (3.81 cm long  $\times$  3.81 cm  $\varnothing$ ) crystal [17] attached to a 5.08 cm Hamamatsu Type R6231 PMT [16]. Due to its fast response without slow scintillation components and excellent energy resolution (3.8% FWHM for the full-energy peak produced by the 662 keV gamma-ray from <sup>137</sup>Cs), CeBr<sub>3</sub> is a useful scintillator for gamma-ray spectroscopy. Operating voltage was set at about  $-850$  V, and energy calibration was determined using standard gamma-ray sources. The CeBr<sub>3</sub> gamma-ray detector was used to measure the gamma-ray spectra associated with the Am/Be and Pu/Be sources.

## 3. Measurement

### 3.1. Setup

The measurements described below were performed sequentially for each of the actinide/Be sources. The CeBr<sub>3</sub> detector used for gamma-ray spectroscopy was located 50 cm from the source and placed at source height. Neutron shielding by organic materials or water was not employed to avoid production of 2.23 MeV gamma-rays from neutron capture on protons. The threshold for the CeBr<sub>3</sub> detector was set at about 350 keV. For the neutron-tagging measurements, water and plastic shielding were employed to define a neutron beam. Four YAP(Ce) 4.44 MeV gamma-ray trigger detectors were individually positioned around the source at a distance of about 10 cm and placed slightly above the height of the source. The threshold for the YAP(Ce) detectors was also set at about 350 keV. The NE-213 detector was located 110 cm from the source and placed also at source height. The threshold for the NE-213 detector was set at about 200 keV<sub>ee</sub> (keV electron equivalent). In the energy region above 1 MeV, all of the detectors triggered largely on the 4.44 MeV gamma-rays emanating from the source. The NE-213 detector triggered on both gamma-rays and neutrons produced by the source. Neutron time-of-flight (TOF) and thus energy

was determined by detecting both the fast neutron in the NE-213 detector and the prompt correlated 4.44 MeV gamma-ray in a YAP(Ce) detector. By tagging the neutrons in this fashion, the neutron yield as a function of kinetic energy was measured. Note that due to the energy lost to the 4.44 MeV gamma-ray, the tagging technique restricted the maximum available tagged-neutron energies to about 6 MeV.

### 3.2. Electronics and data acquisition

The analog signals from the NE-213 detector were sent to Phillips Scientific (PS) 715 NIM constant-fraction timing discriminators (CFDs) as well as LeCroy (LRS) 10-bit 2249A (DC-coupled 60 ns short gate SG) and 11-bit 2249W (AC-coupled 500 ns long gate LG) CAMAC charge-to-digital converters (QDCs). The analog signals from the CeBr<sub>3</sub> detector were sent to PS715 NIM CFDs as well as CAEN V792 12-bit (DC-coupled 60 ns gate) VME QDCs. For both the tagged-neutron and untagged gamma-ray measurements, the CFD signals were used to trigger the data-acquisition (DAQ). For the tagged-neutron measurements, the CFD signals from the NE-213 detector also provided start signals for LRS 2228A CAMAC time-to-digital converters (TDCs) used for the neutron TOF determination. The YAP(Ce) detector provided the corresponding (delayed) stop signal for this TOF TDC. A CES 8210 branch driver was employed to connect the CAMAC electronics to a VMEbus and a SIS 3100 PCI-VME bus adapter was used to connect the VMEbus to a LINUX PC-based DAQ system. The signals were recorded and processed using ROOT-based software [18]. See Refs. [1, 13] for more detail.

## 4. Results

### 4.1. Pulse-shape discrimination (PSD)

We employed the “tail-to-total” method [19–21] to analyze the time dependence of the scintillation pulses to discern between gamma-rays and neutrons. The pulse shape (PS) was defined as

$$PS = (LG - SG)/LG, \quad (1)$$

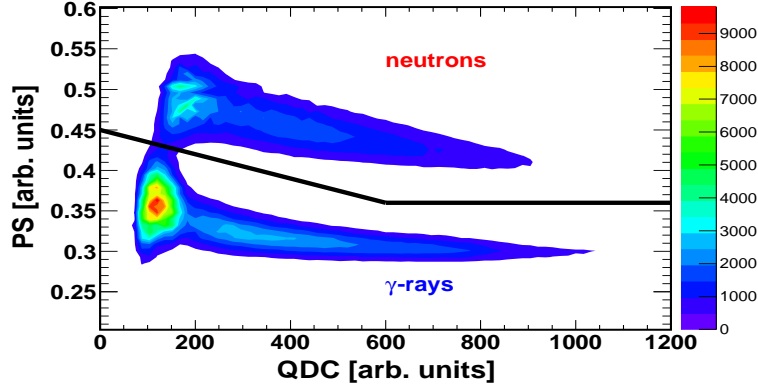


Figure 2: Typical PSD contour plot obtained using the actinide/Be sources. PS has been plotted against the total energy deposited in the LG QDC. The upper band corresponds to neutrons while the lower band corresponds to gamma-rays. The black line indicates the neutron cut applied to obtain subsequent spectra. (For interpretation of the references to color in this figure caption, the reader is referred to the web version of this article.)

where  $LG$  and  $SG$  were the integrated charges produced by the scintillation-light pulses in the LG and SG QDCs, respectively. Figure 2 shows a contour PSD distribution obtained using the Pu/Be source when the NE-213 detector started the TOF TDC and the YAP(Ce) detector stopped the TOF TDC. Separation between neutrons and gamma-rays was excellent.

#### 4.2. Time-of-flight (TOF)

Data from the TOF TDC were calibrated and used to establish the neutron time-of-flight. Correlated gamma-ray pairs originating in the sources and detected one in the NE-213 detector and one in a YAP(Ce) detector provided a “gamma-flash”<sup>2</sup>.  $T_0$ , the instant of emission of the neutron from the source, was

<sup>2</sup>For example, from the  $\alpha$  decay of  $^{241}\text{Am}$  to an excited state of  $^{237}\text{Np}$ .

determined from the location of the gamma-flash in the TOF spectra using the speed of light and measurements of the distances between the YAP(Ce) detector, the NE-213 detector, and the source. In the top panel of Fig. 3, the excellent separation between gamma-rays and neutrons is illustrated in a contour plot of PS against TOF. In the bottom panel, the contour plot has been projected onto the TOF axis. Further, the black-line cut from Fig. 2 has been applied, and a TOF distribution for events identified as neutrons is shown. The gamma-flash has a FWHM of about 1.5 ns (arising from the timing jitter in our signals) and is located at 3.5 ns. Tagged neutrons dominate the plot between 30 ns and 70 ns. Events between 8 and 30 ns and for TOF > 70 ns are mainly due to random coincidences. Random events included source-related gamma-rays and neutrons and depended on the singles rates in the YAP and NE-213 detectors.

#### *4.3. Untagged gamma-ray yields*

Figure 4 shows our untagged gamma-ray yields obtained with the CeBr<sub>3</sub> detector. Other than cycling the sources, no changes were made to the apparatus. A software cut has been placed at 1 MeV to exclude very low energy gamma-ray events, including room-associated background. Over this energy range, the gamma-ray field from the Pu/Be source is clearly stronger than that from the Am/Be source, but the structure is very similar. The structures in the Pu/Be and Am/Be gamma-ray distributions 3 and 5 MeV correspond to neutron-associated gamma-rays from the de-excitation of <sup>12</sup>C\*. The full-energy peak appears at 4.44 MeV, while the corresponding first- and second-escape peaks appear at 3.93 MeV and 3.42 MeV, respectively. The peak at 2.61 MeV corresponds to the de-excitation of <sup>208</sup>Pb\* to its ground state and is due to room background.

#### *4.4. Tagged-neutron yields*

Figure 5 shows our actinide/Be tagged-neutron results obtained by measuring the neutron TOF between the NE-213 trigger and YAP(Ce) 4.44 MeV gamma-ray detectors. Our data are livetime-corrected yields – they have not

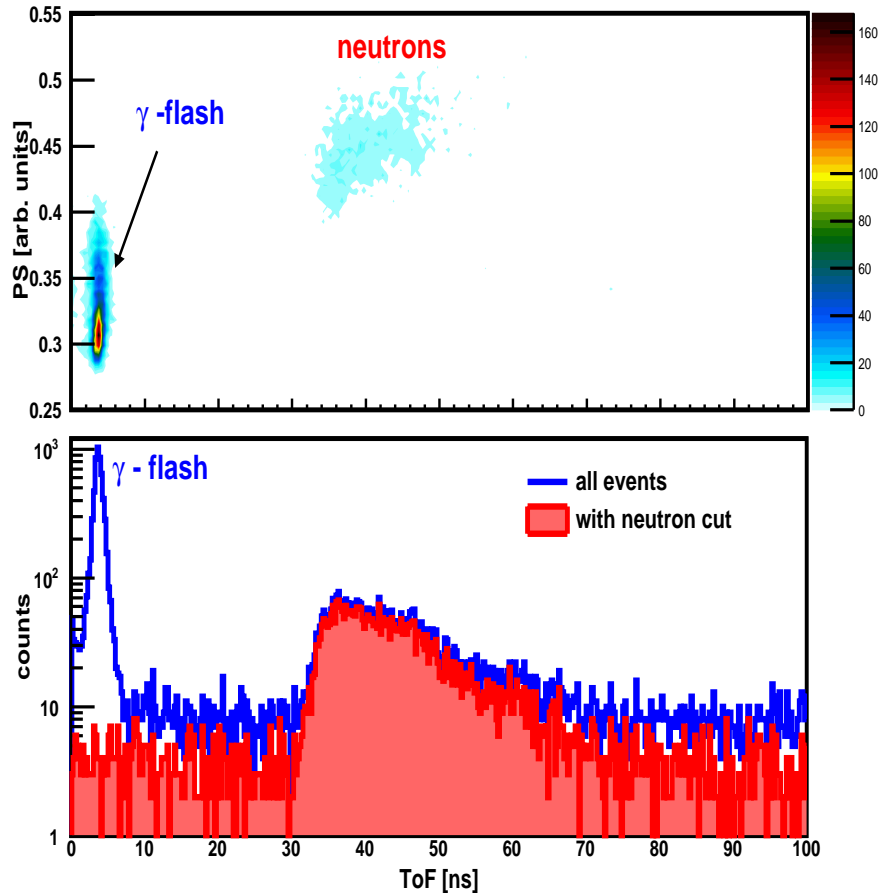


Figure 3: Typical TOF distributions obtained using the actinide/Be sources. In the top panel, PS has been plotted against TOF. Gamma-rays from the gamma-flash are shown to the left of the plot, while neutrons are shown in the center. In the bottom panel, TOF distributions have been plotted for all events (unshaded blue) as well as events identified as neutrons (shaded red). The peak in the unshaded blue distribution located at about 4 ns is the gamma-flash. (For interpretation of the references to color in this figure caption, the reader is referred to the web version of this article.)

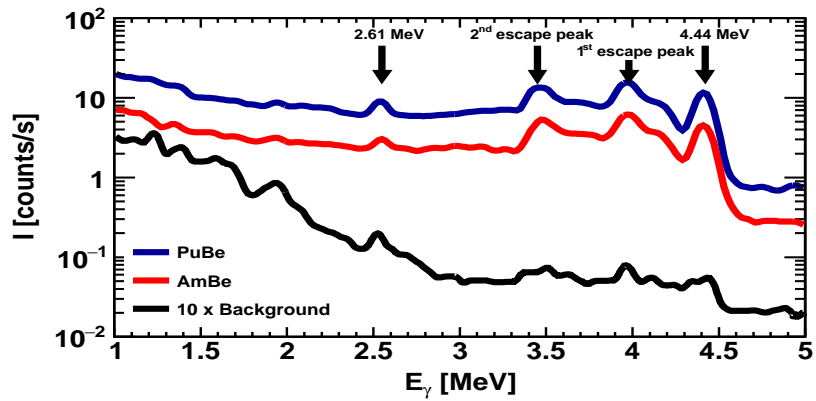


Figure 4: Untagged livetime-corrected gamma-ray yields. The dark blue distribution corresponds to the gamma-ray field measured from the Pu/Be source, the red distribution corresponds to the gamma-ray field measured from the Am/Be source, and the light-blue distribution corresponds to the gamma-ray field measured without a source. (For interpretation of the references to color in this figure caption, the reader is referred to the web version of this article.)

been corrected for neutron-detection efficiency or detector acceptance. Note that other than physically swapping the actinide/Be sources, absolutely no changes were made to our apparatus during data acquisition. In both panels, the maximum values of the Lorch spectra at  $\sim 3$  MeV have been normalized to our distributions. Due to the neutron-tagging procedure, our data show no strength above  $\sim 7$  MeV as 4.44 MeV is taken by the creation of the de-excitation gamma-ray. Our results for Am/Be presented in the top panel are shown together with the widely quoted full-energy neutron spectrum of Lorch [3]<sup>3</sup> and the ISO 8529-2 reference neutron radiation spectrum. Agreement between the Lorch data and the reference spectrum is very good between 2.5 MeV and 10 MeV. Lorch did not observe the strength above 10 MeV present in the reference spectrum. The Lorch data display a sharp cutoff at 2.5 MeV which is attributed to an analysis threshold cut. The reference spectrum shows considerable strength below 2.5 MeV. Our data also show some strength in this region. Recall that our hardware threshold was 200 keV<sub>ee</sub> corresponding to a neutron energy of  $\sim 1$  MeV, and that no analysis threshold cut was employed. The agreement between our data, those of Lorch, and the reference spectrum in the region of overlap is excellent. The interested reader is directed to Ref. [1] for a detailed discussion. Our results for Pu/Be presented in the bottom panel are shown together with those of Kozlov et al. [22]. The Kozlov et al. measurement involved detecting the neutrons emitted from a series of “homemade” Pu/Be sources in a cylindrical (30 mm long  $\times$  30 mm  $\varnothing$ ) stilbene crystal. Statistical uncertainties in these results were reported to be better than 3% below 5 MeV and better than 20% at 10 MeV. Similar to the Lorch data discussed above, the Kozlov et al. data also display a sharp cutoff at 2.5 MeV. While it is not possible to determine

---

<sup>3</sup> The results we present in this paper are for a newly acquired Am/Be source that is different from the source that we used to produce the results presented in Ref. [1]. Due to flight-path differences and the resulting resolution effects, it is difficult to exactly compare the two data sets. Nevertheless, over the energy range 2 – 6 MeV, the difference in the tagged-neutron yields (normalized at 3 MeV) obtained with the two different sources is less than 2%.

the reason for this cutoff from the information presented in Ref. [22], we again attribute it to an analysis threshold cut. Recall that our hardware threshold was 200 keV<sub>ee</sub> corresponding to a neutron energy of  $\sim 1$  MeV, and that no analysis threshold cut was employed. Agreement between the Kozlov et al. data and ours is very good between 2.5 MeV and 6 MeV. Finally, we note the qualitative agreement between our Am/Be and Pu/Be results, the Lorch and Kozlov et al. results, and the ISO ISO8529-2 reference neutron radiation spectrum.

Figure 6 presents a quantitative comparison between the livetime-corrected tagged-neutron yields for our Am/Be and Pu/Be sources. The (Pu/Be) : (Am/Be) ratio is taken from the gray-shaded regions presented in Fig. 5 and is displayed for the energy region over which we are confident that we are not simply seeing effects from applied hardware thresholds. The mean value of the ratio between 2 and 6 MeV is 2.4, which is in reasonable agreement with the original full-spectrum source-calibration measurements performed at the time of their acquisition. Explanation of the observed fluctuation in the ratio as a function of neutron energy requires a more detailed study of the possible effects of source composition, neutron-detection efficiency, and detector acceptances. This will be covered in future work.

## 5. Summary

We have measured untagged gamma-ray and tagged neutron yields from  $^{241}\text{AmBe}$  and  $^{238}\text{PuBe}$  sources. Our untagged gamma-ray distributions ranged from 1 – 5 MeV. They were performed in an open environment with the same experimental conditions for both sources. The shapes of the distributions are very similar and are clearly dominated by the 4.44 MeV gamma-ray associated with the de-excitation of the first excited state in  $^{12}\text{C}$ . Our tagged-neutron distributions ranged from 2 – 6 MeV. They were performed in a shielded environment with the same experimental conditions for both sources. The shapes of the distributions are quite similar and agree well with previous data obtained for the respective sources. Further, the shape of the Am/Be distribution agrees well

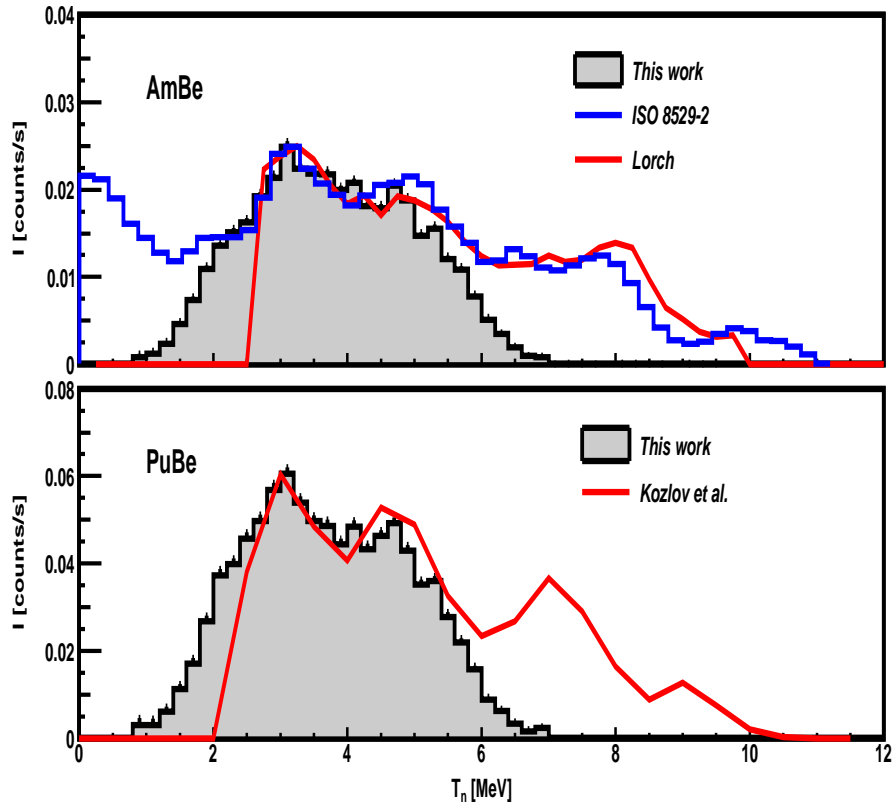


Figure 5: Tagged-neutron results. The gray-shaded histograms are our livetime-corrected tagged-neutron measurements. Note the different y-axis scales in the top and bottom panel. Top panel: Am/Be. The full-energy spectrum (red line) of Lorch [3] is also shown together with the Am/Be ISO 8529-2 reference neutron radiation spectrum. Bottom panel: Pu/Be. The full-energy spectrum (red line) of Kozlov et al. [22] is also shown. (For interpretation of the references to color in this figure caption, the reader is referred to the web version of this article.)

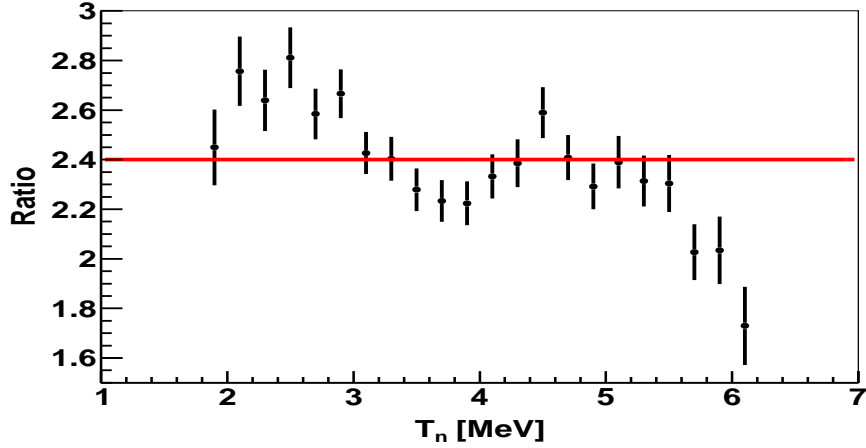


Figure 6: Lifetime-corrected (Pu/Be) : (Am/Be) ratio of tagged-neutron yields.

with the ISO 8529-2 reference neutron radiation spectrum. We determined that our Pu/Be source emits roughly 2.4 times as many taggable neutrons as our Am/Be source, in reasonable agreement with the original full-spectrum source-calibration measurements performed at the time of their acquisition. Observed differences in the details of the shape of the neutron spectra will be the subject of future investigations.

### Acknowledgements

We acknowledge the support of the UK Science and Technology Facilities Council (Grant nos. STFC 57071/1 and STFC 50727/1) and the European Union Horizon 2020 BrightnESS Project, Proposal ID 676548.

## References

- [1] J. Scherzinger et al., *Applied Radiation and Isotopes* 98 (2015) 74, doi: 10.1016/j.apradiso.2015.01.003.
- [2] <http://www.nndc.bnl.gov/nudat2/>.
- [3] E.A. Lorch, *Int. J. Appl. Radiat. Is.* 24 (1973) 585, doi: 10.1016/0020-708X(73)90127-0.
- [4] Exactly  $(1.143 \pm 0.015) \times 10^6$  neutrons per second. Testing certified at National Physical Laboratory, Teddington, Middlesex, UK TW11 0LW on 24 July 2015.
- [5] Exactly  $4.26 \times 10^6$  neutrons per second. Calibration certified at The Radiochemical Centre, Amersham, England HP7 9LL on 3 September, 1973.
- [6] Eljen Technologies EJ-301 (<http://www.eljentechnology.com/index.php/products/liquid-scintillators/71-e>) Saint Gobain BC-501 (<http://www.detectors.saint-gobain.com/uploadedFiles/SGdetectors/Documents/Pi>)
- [7] <http://www.eljentechnology.com/index.php/products/paints/87-ej-520>.
- [8] <http://www.us.schott.com/borofloat/english/index.html> for details. Supplied by Glasteknik i Emmaboda AB, Utvägen 6 SE-361 31 Emmaboda, Sweden.
- [9] Poly-methyl-methacrylate, also known as PMM, acrylic, plexiglass, and lucite. Supplied by Nordic Plastics Group AB, Bronsyxegatan 6, SE-213 75 Malmö, Sweden.
- [10] <http://www.eljentechnology.com/index.php/products/paints/86-ej-510>.
- [11] <http://www.et-enterprises.com/files/file/Pmtbrochure11.pdf> for details.
- [12] H.H. Knox and T.G. Miller, *Nucl. Instrum. and Meth.* 101 (1972) 519, doi: 10.1016/0029-554X(72)90040-7.
- [13] J. Scherzinger et al., *Nucl. Instr. and Meth. in Phys. Res. A* 840 (2016) 121, doi:10.1016/j.nima.2016.10.011.

- [14] Scionix Holland BV. <http://www.scionix.nl>.
- [15] M. Moszyński et al., Nucl. Instr. and Meth. in Phys. Res. A 404 (1998) 157, doi:10.1016/S0168-9002(97)01115-7.
- [16] Hamamatsu Photonics. <http://www.hamamatsu.com>.
- [17] R. Billnert, S. Oberstedt, E. Andreotti, M. Hult, G. Marissens, A. Oberstedt, Nucl. Instr. and Meth. in Phys. Res. A 674 (2011) 94, doi:10.1016/j.nima.2011.05.034.
- [18] R. Brun and F. Rademakers, Nucl. Instr. and Meth. in Phys. Res. A 389 (1997) 81-86. See also <http://root.cern.ch/>.
- [19] A. Jhingan et al., Nucl. Instr. and Meth. in Phys. Res. A 585 (2008) 165, doi:10.1016/j.nima.2007.11.013.
- [20] A. Lavagno et al., Nucl. Instr. and Meth. in Phys. Res. A 617 (2010) 492, doi:10.1016/j.nima.2009.10.111.
- [21] I.A. Pawelczak et al., Nucl. Instr. and Meth. in Phys. Res. A 711 (2013) 21, doi:10.1016/j.nima.2013.01.028
- [22] A.G. Kozlov, B.A. Moiseenko, V.B. Pavlovich, E.G. Ponomarev, N.D. Tyufyakov, A.S. Shtan', V.S. Yaskevich, A.G. Kovlov et al., translated from Atomnaya Énergiya 25 (1968) 534.

Paper V





# Tagging fast neutrons from a $^{252}\text{Cf}$ fission-fragment source

J. Scherzinger<sup>a,b</sup>, R. Al Jebali<sup>1</sup>, J.R.M. Annand<sup>c</sup>, K.G. Fissum<sup>a,b,\*</sup>,  
R. Hall-Wilton<sup>b,d</sup>, N. Mauritzson<sup>a</sup>, F. Messi<sup>a</sup>, H. Perrey<sup>a,b</sup>, E. Rofors<sup>a</sup>

<sup>a</sup>*Division of Nuclear Physics, Lund University, SE-221 00 Lund, Sweden*

<sup>b</sup>*Detector Group, European Spallation Source ESS AB, SE-221 00 Lund, Sweden*

<sup>c</sup>*University of Glasgow, Glasgow G12 8QQ, Scotland, UK*

<sup>d</sup>*Mid-Sweden University, SE-851 70 Sundsvall, Sweden*

---

## Abstract

Coincidence and time-of-flight measurement techniques are employed to tag fission neutrons emitted from a  $^{252}\text{Cf}$  source. Fission fragments detected in a gaseous  $^4\text{He}$  scintillator detector supply the tag. Neutrons are detected in a NE-213 liquid-scintillator detector. The resulting continuous polychromatic beam of tagged neutrons has an energy dependence that agrees qualitatively with expectations.

*Keywords:* californium-252, fission fragments, fast neutrons, time-of-flight, tagging

---

## 1. Introduction

We recently reported on our efforts to “tag” fast neutrons from an  $^{241}\text{Am}/^9\text{Be}$  source [1] as a first step towards the development of a source-based fast-neutron irradiation facility. Here, we use a  $^{252}\text{Cf}$  fission-fragment fast-neutron tagging technique very similar to that reported on by Reiter et al. [2]. We detect the fission fragments in a gaseous  $^4\text{He}$ -based scintillator detector and the corresponding neutrons in a NE-213 [3] liquid-scintillator detector. This effort represents our first step towards the development of an apparatus for the measurement of

---

\*Corresponding author. Telephone: +46 46 222 9677; Fax: +46 46 222 4709  
Email address: kevin.fissum@nuclear.lu.se (K.G. Fissum)

absolute neutron-detection efficiency at our source-based fast-neutron irradiation facility.

## 2. Apparatus

### 2.1. Californium fission-fragment source

$^{252}\text{Cf}$  is an intense source of fast neutrons. With an overall half life of 2.645 years and a specific activity of 0.536 mCi/ $\mu\text{g}$ , it decays by both  $\alpha$ -particle emission (96.908%) and spontaneous fission (SF – 3.092%) [4]. The weighted average  $\alpha$ -particle energy is  $\sim 6111.69$  keV. The prompt-neutron yield is  $\sim 3.75$  neutrons per fission event [5, 6]. The resulting fast-neutron energy distribution follows the Watt distribution [7] and is very well known, with a most-probable energy of 0.7 MeV and an average energy of 2.1 MeV. Our californium source [8] has a (nominal) activity of 3.7 MBq [9]. While trace activity comes from  $^{249}\text{Cf}$  ( $<0.2\%$ ) and  $^{251}\text{Cf}$  ( $<0.04\%$ ), the majority comes from  $^{250}\text{Cf}$  ( $\sim 7.5\%$ ) and  $^{252}\text{Cf}$  ( $\sim 92.3\%$ ). We thus estimate a neutron emission rate of  $\sim 4 \times 10^5$  neutrons per second. The californium source has an active diameter of 5 mm and is mounted on an A2301 capsule [8]. The thick back side of the source is platinum-clad nickel, and does not allow fission fragments to escape. The thin front side of the source is covered with a  $50 \mu\text{g}/\text{cm}^2$  Au sputter which allows both  $\alpha$  particles and heavy fission fragments to escape. When not in use and in order to protect the thin front side, the source-containing capsule may be loaded into a cylindrical A5505 source holder [8] 19.1 mm high  $\times$  31.8 mm  $\varnothing$ , which resembles a relatively flat pill bottle with a male-threaded lid.

### 2.2. Gaseous $^4\text{He}$ fission-fragment detector

The noble gas  $^4\text{He}$  is a good scintillator with an ultra-violet light yield of about the same magnitude as intrinsic (non Tl-doped) NaI crystals [10–13]. In this measurement, we employed a gas cell built originally as a prototype active target for recent  $^4\text{He}$  photoreaction measurements [14]. The cell was machined from a solid aluminum block and has a cylindrical interior volume measuring 72 mm long  $\times$  58 mm  $\varnothing$ , for an inner volume of  $\sim 0.35$  liters (see Fig. 1).

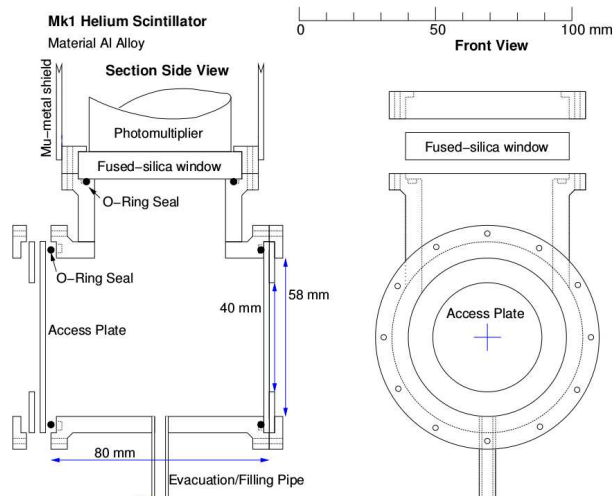


Figure 1: A drawing of the gas cell. Left panel: Section Side View. The cell is filled with 5 bar of gaseous  $^4\text{He}$  scintillator and 500 ppm gaseous  $\text{N}_2$  wavelength shifter. Right panel: Front View. The PMT attaches from the top.

The interior of the gas cell was sandblasted and then treated with two layers of water soluble EJ-510 reflective paint [15]. A fused-silica optical window 10 mm thick  $\times$  60 mm  $\varnothing$  is pressed against the body of the cell and allows the scintillation light produced by the fission fragments to escape. A rubber O-ring provides the pressure seal. The cell was filled with 5 bar 99.99999% pure  $^4\text{He}$  (scintillator) gas together with 2.5 mbar 99.99999% pure  $\text{N}_2$  (scintillation-wavelength shifter) gas. A photograph of the assembled cell is shown in the left panel of Fig. 2. A 2 in. XP2262B photomultiplier tube (PMT) [16] was attached to the optical window, and EJ-550 optical grease [17] was employed at the boundary. A photograph of the assembled detector (gas cell and PMT) is shown in the right panel of Fig. 2.

The californium source described above was positioned at the center of the gas cell so that the thin front side through which the fission fragments could escape faced away from the optical window. The distance from the californium



Figure 2: Fission-fragment detector. Left panel: photograph of the  $^4\text{He}$  gas cell. Right panel: photograph of the gas cell and PMT assembly. The PMT assembly is the black cylinder to the right. (For interpretation of the references to color in this figure caption, the reader is referred to the web version of this article.)

source to the center of the fused-silica optical window was  $\sim 65$  mm. Operating voltage for the PMT was  $-1750$  V and the discriminator threshold was set at  $-60$  mV. Typical signal risetime was 5 ns, while the falltime to  $<10\%$  of the original amplitude was  $\sim 10$  ns. Figure 3 shows some typical detector pulses obtained with the  $^4\text{He}$  gas cell. The small pulses result from  $\alpha$  particles, the medium pulses result from lower-energy, heavier fragments and the large pulses result from higher-energy, lighter fragments. See also the histogram presented in Fig. 6.

### 2.3. NE-213 fast-neutron and gamma-ray liquid-scintillator detector

NE-213 is an organic liquid scintillator that has been employed for decades as a fast-neutron detector. The NE-213 liquid-scintillator detector used here has been reported upon earlier [1, 18, 19]. It consisted of a 62 mm long  $\times$  94 mm  $\varnothing$  cylindrical aluminum cell fitted with a borosilicate glass optical window [20]. The filled cell was dry-fitted against a cylindrical PMMA UVT lightguide [21] and coupled to a  $\mu$ -metal shielded 3 in. ET Enterprises 9821KB photomultiplier tube (PMT) and base [22]. Operating voltage was set at about  $-1900$  V,

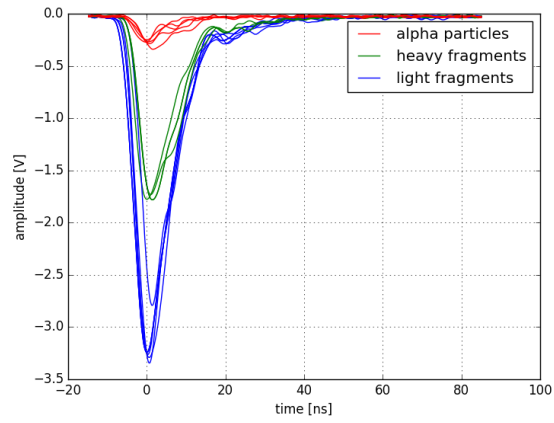


Figure 3: Typical pulses associated with the decay of  $^{252}\text{Cf}$  obtained with the  $^4\text{He}$  gas cell. Top (red) trace:  $\alpha$  particles. Middle (green) trace: heavy fission fragments. Bottom (blue) trace: light fission fragments. (For interpretation of the references to color in this figure caption, the reader is referred to the web version of this article.)



Figure 4: The NE-213 detector (CAD representation). Top: the aluminum scintillator “cup”. A borosilicate-glass window (light brown) separates the scintillator and lightguide. Bottom: The “cup” is to the left. The  $\mu$ -metal shielded PMT and base assembly is the black cylinder to the right. Figure from Ref. [18]. (For interpretation of the references to color in this figure caption, the reader is referred to the web version of this article.)

and the energy calibration was determined using standard gamma-ray sources together with a slightly modified version of the method of Knox and Miller [23] as described in Ref. [19]. The detector threshold was set at 150 keV electron equivalent ( $\text{keV}_{ee}$ ), corresponding to a neutron energy of about 1 MeV.

#### 2.4. Configuration

A block diagram of the electronics is shown in Fig. 5. Neutrons and gamma-rays were detected in the NE-213 detector and fission fragments were detected in the  $^4\text{He}$  fission-fragment detector. The analog signals from the NE-213 detector were passed to a Phillips Scientific (PS) 715 NIM constant-fraction timing discriminator (CFD). The analog signals from the  $^4\text{He}$  fission-fragment detector were fanned out and passed to a PS715 NIM CFD as well as a CAEN V792 12-bit (DC-coupled 60 ns gate) VME QDC. The CFD signals from the  $^4\text{He}$  fission-fragment detector were used to trigger the data-acquisition (DAQ) and



The  $\alpha$  particles which dominate the spectrum and correspond to the red trace in Fig. 3 are shown as the peak centered at about channel 190. Note that the entire  $\alpha$ -particle distribution is not shown as the discriminator threshold cuts into it. Separation of fragments and  $\alpha$  particles is not completely clean, as seen in the grey shaded area of Fig. 6 between channels 230 and 540. This could result from non-uniform scintillation-light collection, different energy losses of different particle types in the source as well as the thin Au source window, non-linearity of the scintillation, or even fission fragments striking the source holder. This will be examined in more detail in a future publication. Heavy fission fragments (green trace in Fig. 3 and dashed green trace here centered at channel 950) and light fission fragments (blue trace in Fig. 3 and dot-dashed blue trace here centered at channel 1310) are also shown. Recall that the average  $\alpha$ -particle energy is  $\sim 6.1$  MeV, while the average heavy fission-fragment energy is 80 MeV and the average light fission-fragment energy is 104 MeV. If we calibrate our QDC based upon the average energy deposition of the two fission fragments and apply this calibration to the  $\alpha$ -particle distribution, we reconstruct this peak at  $\sim 12$  MeV.  $^4\text{He}$  is often assumed to be a linear scintillator, while this preliminary analysis suggests an apparent non-linearity. However, as outlined above, there are several factors which will affect the apparent scintillation-pulse height. The degree of non-linearity in the scintillation (if any) requires an in-depth study. For the data presented subsequently in this paper, a software fission-fragment cut located at channel 520 was employed.

Figure 7 shows a fission-neutron TOF spectrum obtained using the signal in the  $^4\text{He}$  fission-fragment detector to start a TDC and a signal from the NE-213 detector to stop it. Note that the spectrum shown corresponds to events lying above the software fission-fragment cut at channel 520 shown in Fig. 6. After this cut, interpretation of the resulting TOF spectrum is straightforward. The sharp peak to the left of the spectrum centered at about 5 ns and labeled “gamma-flash” in Fig. 7 corresponds to the detection of a fission-event gamma-ray in the NE-213 detector associated with detection of a fission fragment in the  $^4\text{He}$  scintillator. The tail in the distribution is possibly due to time walk

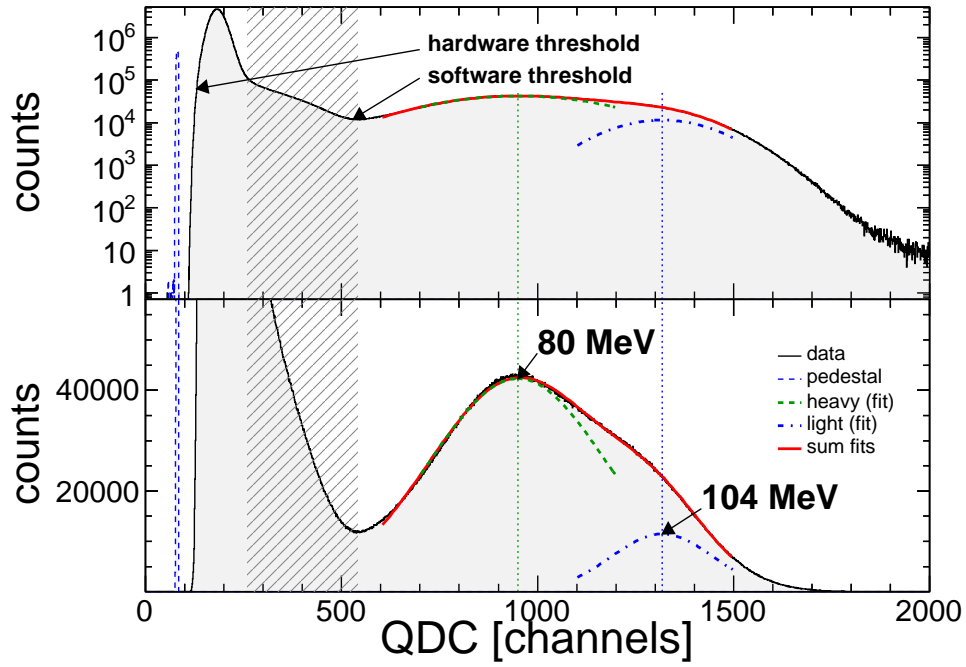


Figure 6: Deposited-energy histogram measured using the  $^4\text{He}$  fission-fragment detector. Both panels present the same data set. The pedestal (blue dashed peak), discriminator threshold, software fission-fragment cut, and distributions corresponding to  $\alpha$ -particles, heavy fission fragments (green dashed line), and light fission fragments (blue dot-dashed line) are all shown. (For interpretation of the references to color in this figure caption, the reader is referred to the web version of this article.)

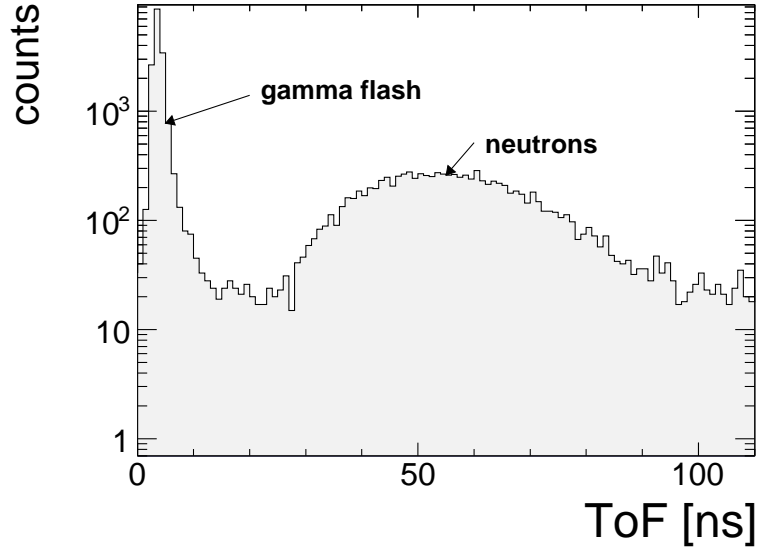


Figure 7: Fission-neutron TOF spectrum. The gamma-flash and fission-neutron distribution are shown. The flat background is due to random events.

or jitter in the electronics. The present apparatus is almost completely insensitive to multiple gamma-ray events. The  $^4\text{He}$  scintillator is highly insensitive to gamma-rays [14, 18] and any electrons produced via Compton scattering or pair production will produce only a very small scintillation signal, which will be entirely suppressed by the relatively high software cut applied on the signals from the  $^4\text{He}$  scintillator. We note that the  $\sim 1.8$  ns FWHM of the gamma-flash is consistent with the observed timing jitter on our PMT signals. The broad bump centered at about 55 ns corresponds to the fission-neutron distribution. The background corresponds to random coincidences. The background distribution was measured to be flat as expected by breaking line-of-sight between the  $^4\text{He}$  fission-fragment detector and the NE-213 detector using a stack of lead ( $\sim 15$  cm) and polyethylene ( $\sim 10$  cm).

Figure 8 shows the fission-neutron TOF spectrum from Fig. 7 converted to a neutron kinetic-energy spectrum. To convert from TOF to neutron kinetic

energy, we used the 5 ns position of the gamma-flash shown in Fig. 7 and the 106 cm distance between the  $^{252}\text{Cf}$  source and the center of the NE-213 liquid-scintillator cell. The data were then rebinned linearly. Also shown are three representations of the neutron-kinetic energy distribution constructed using the information presented by Thomas in Ref. [26]. A normalization factor has been applied to each of these representations so that they coincide with our data at 1.5 MeV, but nonetheless, there are small differences between the representations. It should be emphasized that the present data have not been corrected for neutron-detection efficiency and that, with the present applied neutron-detector threshold, energies below 1 MeV cannot be corrected for reliably. At 1 MeV, the agreement between all three is essentially exact. Between 1 MeV and 4 MeV, the Maxwellian approximation and the ISO 8529-1 representation both lie below the ENDF/B-VII suggestion by 2% and 1%, respectively. By 5 MeV, the agreement between all three is again essentially exact. Above 6 MeV, a strong divergence of the representations begins and by 8 MeV, both the Maxwellian and the ISO 8529-1 representations lie above the ENDF/B-VII suggestion by about 9% and 4%, respectively. The  $\pm 1\%$  level of agreement between all three representations of the  $^{252}\text{Cf}$  fission-neutron energy spectrum over the energy region from 1 to 6 MeV is well within any systematic uncertainty that we are likely to obtain in measurements of neutron-detection efficiency using the tagging technique. Thus, they provide an excellent benchmark from which it will be possible to evaluate the neutron-detection efficiency.

#### 4. Summary

As a first step towards the development of an apparatus for the measurement of neutron-detection efficiency at our source-based fast-neutron irradiation facility, we have employed coincidence and time-of-flight measurement techniques to “tag” neutrons emitted by a  $^{252}\text{Cf}$  source. The spontaneous-fission fragments are detected in a gaseous  $^4\text{He}$  fission-fragment detector. The neutrons are detected in a NE-213 liquid-scintillator detector. The resulting continuous

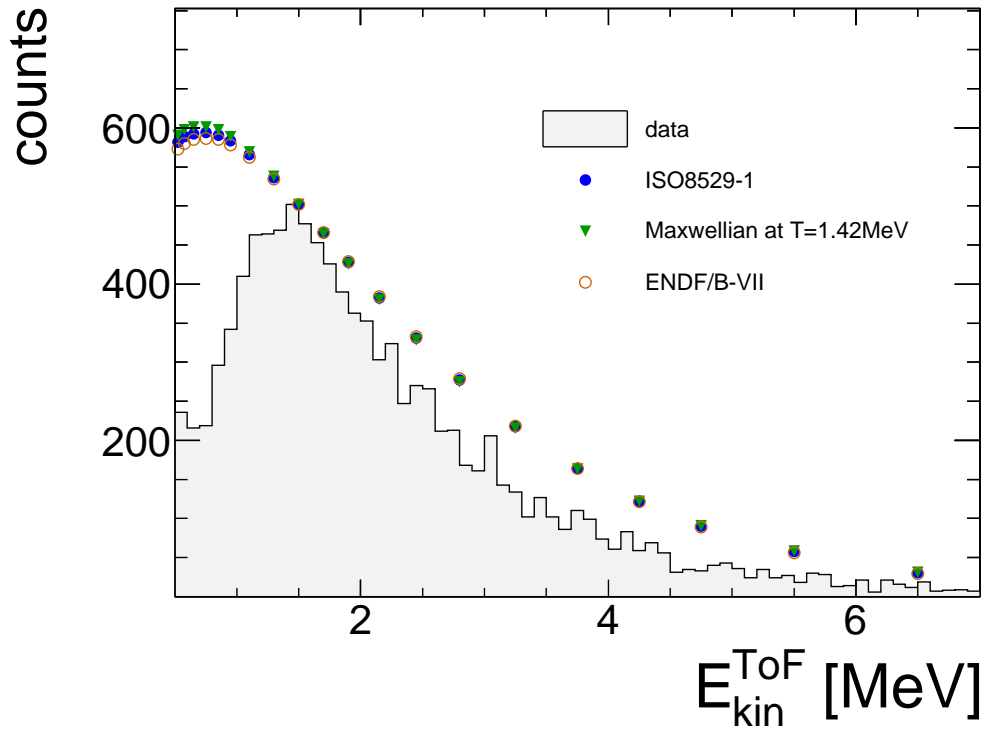


Figure 8: Fission-neutron kinetic energy spectrum for  $^{252}\text{Cf}$ . The grey histogram is measured data. Also shown are the ISO 8529-1 recommendation (filled blue circles), a Maxwellian approximation (green triangles), and the ENDF/B-VII suggestion (open red circles) for the fission-neutron spectrum. (For interpretation of the references to color in this figure caption, the reader is referred to the web version of this article.)

polychromatic beam of tagged neutrons has a measured energy dependence that agrees qualitatively with expectations. This preliminary study strongly suggests that this method of neutron energy tagging will work well and future investigations will concentrate on quantifying systematic effects in order to optimize the performance. We anticipate that the technique will provide a cost effective means for the characterization of neutron-detector efficiency. We note that this technique will work equally well for all spontaneous-fission neutron sources.

### **Acknowledgements**

We acknowledge the support of the UK Science and Technology Facilities Council (Grant nos. STFC 57071/1 and STFC 50727/1) and the European Union Horizon 2020 BrightnESS Project, Proposal ID 676548.

## References

- [1] J. Scherzinger et al., *Applied Radiation and Isotopes* 98 (2015) 74, doi: 10.1016/j.apradiso.2015.01.003.
- [2] A. Reiter et al., *Nucl. Instr. and Meth. in Phys. Res. A* 565 (2006) 753, doi: 10.1016/j.nima.2006.06.048
- [3] NE-213 is no longer produced. Eljen Technologies offers EJ-301 (<http://www.eljentechnology.com/index.php/products/liquid-scintillators/71-ej-301>) while Saint Gobain offers BC-501 (<http://www.detectors.saint-gobain.com/uploadedFiles/SGdetectors/Dc>)
- [4] <http://www.nndc.bnl.gov/nudat2/>.
- [5] J.W. Boldeman, M.G. Hines, *Nucl. Sci. Eng.* 91 (1985) 114.
- [6] E.J. Axton, A.G. Bardell *Metrologia* 21 (1985) 59.
- [7] F.H. Frner, *Nucl. Sci. Eng.* 106 (1990) 345.
- [8] Supplied by Eckert&Ziegler Isotope Products GmbH.
- [9] Testing performed 1 April 2015 at Eckert&Ziegler Isotope Products Medical Imaging Laboratory, 24937 Avenue Tibbitts, Valencia CA 91355, USA.
- [10] *The theory and practice of scintillation counting*, J.B. Birks, D.W. Fry, L. Costrell, K. Kandish, Pergamon Press, New York, U.S.A. (1964), ISBN: 978-0-08-010472-0.
- [11] *The mechanism of noble gas scintillation*, in *Elementary particles and cosmic rays*, B.A. Dolgosheim, B.U. Rodionov, Volume 2, Atomizdat, Moscow Russia (1969).
- [12] *Radiation detection and measurement*, G.F. Knoll, Wiley, New York, U.S.A. (1989), ISBN: 9780471815044, <http://books.google.com/books?id=dyBRAAAAMAAJ>.

- [13] Scintillation detectors, in Noble gas detectors, E. Aprile, A.E. Bolotnikov, A.I. Bolozdynya, T. Doke, Wiley-VCH Verlag GmbH, KGaA, Weinheim Germany (2006), ISBN: 978-3-527-40597-8
- [14] R. Al Jebali et al., Eur. Phys. J. A **51** 123 (2015). doi: 10.1140/epja/i2015-15123-y.
- [15] <http://www.eljentechnology.com/index.php/products/paints/86-ej-510>.
- [16] <https://my.et-enterprises.com/pdf/XP2262.pdf>
- [17] [http://www.eljentechnology.com/images/products/data\\_sheets/EJ-550\\_EJ-552.pdf](http://www.eljentechnology.com/images/products/data_sheets/EJ-550_EJ-552.pdf)
- [18] R. al Jebali et al., Nucl. Instr. and Meth. in Phys. Res. A **794** (2015) 102, doi:10.1016/j.nima.2015.04.058
- [19] J. Scherzinger et al., Nucl. Instr. and Meth. in Phys. Res. A **840** (2016) 121, doi:10.1016/j.nima.2016.10.011.
- [20] <http://www.us.schott.com/borofloat/english/index.html> for details. Supplied by Glasteknik i Emmaboda AB, Utvägen 6 SE-361 31 Emmaboda, Sweden.
- [21] Poly(methyl-methacrylate), also known as acrylic, plexiglass, and lucite. Supplied by Nordic Plastics Group AB, Bronsyxegatan 6, SE-213 75 Malmö, Sweden.
- [22] [www.et-enterprises.com/files/file/Pmtbrochure11.pdf](http://www.et-enterprises.com/files/file/Pmtbrochure11.pdf) for details.
- [23] H.H. Knox, T.G. Miller, Nucl. Instrum. and Meth. **101** (1972) 519.
- [24] R. Brun and Fons Rademakers, Proceedings AIHENP'96 Workshop, Lausanne, Sep. 1996; Nucl. Instr. and Meth. in Phys. Res. A **389** (1997) 81-86. See also <http://root.cern.ch/>.
- [25] J. van Aarle et al., Nucl. Phys. A **578** (1994) 77, doi:10.1016/0375-9474(94)90970-9.
- [26] D. Thomas, ESARDA Bulletin **51** (2014) 45.



# Chapter B

## Posters

### Poster I

#### **Novel Scintillator Materials for Neutron Detection**

The content was presented in 2012 at IKON 3. The poster presents novel and well-known scintillator materials for neutron detection from meV to MeV.

### Poster II

#### **Characterization of a Liquid Scintillator Detector**

The poster was presented in 2012 at IKON 3. A liquid scintillator detector, the prototype of a neutron detector array, was irradiated under experimental conditions with photo-nuclear reaction products from the interaction of hard gamma-rays on  $^{12}\text{C}$ .

## **Poster III**

### **Characterization of a Liquid Scintillator Detector with an Americium-Beryllium source**

The poster was presented in 2013 at IKON 4. An early experimental setup is presented and the tagging technique is explained. The PSD of the NE-213 detector was investigated.

## **Poster IV**

### **A broad-band neutron source facility for detector characterization**

The poster was presented at the 2014 NSS/MIC IEEE in Seattle. The standard neutron tagging technique with an Am/Be source is explained. The idea of extending this technique to thermalized neutrons was investigated with a GEANT 4 simulation.

Poster I





# Novel Scintillator Materials for Neutron Detection

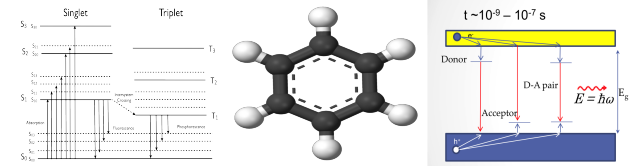
J. Scherzinger<sup>a,b</sup>, K. Fissum<sup>b,c</sup>, R. Hall-Wilton<sup>a</sup>, E. Håkansson<sup>b</sup>, K. Kanaki<sup>a</sup>, M. Lunding<sup>c</sup>, M. Meshkian<sup>b</sup> and B. Nilsson<sup>a,c</sup>

- a) Detector Group, European Spallation Source ESS AB, Lund, Sweden
- b) Division of Nuclear Physics, Lund University, Lund, Sweden
- c) MAX IV Laboratory, Lund, Sweden

## Introduction

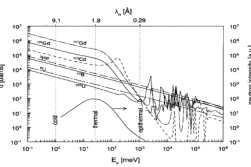
LiF/ZnS(Ag), the "standard" scintillator in neutron scattering of today, and <sup>6</sup>Li-glass (GS20), luminescence inorganic materials are used as detectors in existing neutron sources, such as ISIS, SNS, and J-PARC. However, both scintillators have known limitations. LiF/ZnS(Ag) is opaque and has a long decay time, putting restriction on count rates. On the other hand, GS20 a fast scintillator and transparent has a high  $\gamma$  efficiency and limited  $\alpha/\beta$  discrimination. Therefore, research is conducted to find novel scintillators and to push existing materials to their practical limits. In difference to several other efforts, our interdisciplinary approach will use well established techniques from nuclear physics for neutrons of energies of several MeV and will put less emphasis on engineering solutions in the framework of the currently used scintillator material.

## Scintillator



Scintillators are liquids or solids which are radio luminescence. They can be divided into organic scintillators and inorganic scintillators. Organic scintillators have been used traditionally to detect high energetic fast neutrons, and inorganic scintillators are applied to the detection of thermal neutrons. [1, 2, 3]

## Detection Channels



Fast neutrons are detected in hydrogen rich organic scintillators by recoiling protons from elastic neutron proton scattering. Thermal neutrons are detected by the nuclear reactions:  ${}^6\text{Li} + n \rightarrow {}^3\text{H} + {}^4\text{He} + 4.78 \text{ MeV}$ ,  ${}^{10}\text{B} + n \rightarrow {}^7\text{Li} + {}^4\text{He} + (\gamma) + 2.793 \text{ MeV}$  (2.314 MeV) and  ${}^{155/157}\text{Gd} + n \rightarrow {}^{156/158}\text{Gd} + \gamma$ . [4]

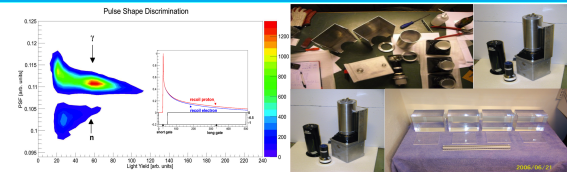
## What is a good scintillator for neutron experiments

Host	Dopant	Density (g/cm <sup>3</sup> )	$\rho_{\text{eff}}^{\text{Li}}$ (x 10 <sup>-3</sup> )	Abs. length (cm)	Light yield photons per 10 <sup>3</sup> e.u. (A units)	$\alpha/\beta$ ratio	$\tau_{\text{dec}}$ (ns)	$t$ (ns)	
Neutron: MeV gamma									
Gamma: MeV gamma									
<sup>6</sup> Li-glass	Ce	2.5	0.52	~6000	~4000	0.3	395	75	
<sup>6</sup> Li	Eu	4.1	31	0.54	200000	120000	0.87	470	1400
LiF/ZnS	Ag	2.6	1.2	0.8	160000	75000	0.44	450	> 1000
LiRbF <sub>4</sub>	Ce	3	35	3500	9000	0.14	190-330	134-2100	
LiRbF <sub>4</sub>	Ce	5.3	35	3600	4300	0.17	190-330	134-2400	
<sup>6</sup> LiGd(B <sub>2</sub> O <sub>7</sub> ) <sub>2</sub>	Ce	3.5	25	0.35	400000	140000	0.59	385-415	200-500
<sup>6</sup> LiGd(B <sub>2</sub> O <sub>7</sub> ) <sub>2</sub> + Y <sub>2</sub> SiO <sub>5</sub>	Ce	3.9	25	0.35	400000	20000	0.59	380	70
Cs <sub>2</sub> Li <sub>2</sub> VCl <sub>6</sub>	Ce	3.3	3.2	70,000	22,000	0.66	380	1000	
					700		255-470	2.7	

\* As an indication of gamma-ray detection efficiency by photoelectric effect  $\rho_{\text{eff}}^{\text{Li}}$  values are presented.

Scintillators for thermal neutron detection are specified by light yield,  $\gamma$  efficiency,  $n/\gamma$  discrimination, resolution, light transmission, intrinsic detection efficiency and decay constant. Further, the application of a scintillator can be limited by economical factors and material properties like flammability and hygroscopicity. [4]

## Liquid Scintillator



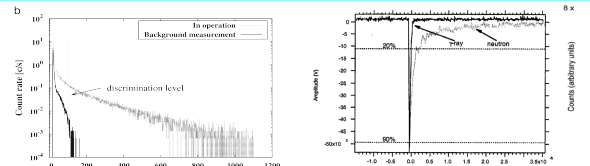
Liquid scintillator, an established technique for the detection of neutrons  $\mathcal{O}$ (MeV) in nuclear physics, allows for high count rates ( $\tau < 5\text{ns}$ ) and a good suppression of the  $\gamma$  background by Pulse Shape Discrimination (PSD). However, the high  $\gamma$  sensitivity of organic scintillators may be problematic for some applications.

## Conclusion

Several different scintillators are alternatives to the scarce <sup>3</sup>He, to detect neutrons in the thermal energy region. At the ISIS facility in Oxfordshire, England, LiF/ZnS(Ag) has been proven to be a suitable replacement of <sup>3</sup>He for many instruments. However, different scintillators may service the need of the neutron scattering community for more efficient and faster detectors. Future research will help close the gap, imposed by cost and performance of available materials, by looking at the problem from a different angle and apply techniques from nuclear physics and beyond. Further, this work will help to keep track of developments of novel scintillators and monitor the cost development of at the moment economically unaffordable rare earth doped, single crystal scintillators.

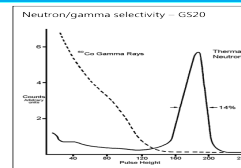
[1] C. Knoll. *Radiation Detection and Measurement*. John Wiley Sons, 4. edition edition, 2010.  
 [2] Wikipedia. [http://en.wikipedia.org/wiki/Neutron\\_scattering](http://en.wikipedia.org/wiki/Neutron_scattering).  
 [3] J. Sikora. [http://info.ssd.gov.uk/isis/inf/fact\\_sheets](http://info.ssd.gov.uk/isis/inf/fact_sheets), 2012.  
 [4] Carl W E van Eijk. Inorganic scintillators for thermal neutron detection. *Radiation Measurements*, 38:337 – 342, 2004.  
 [5] T. Yagi et al. Development of a small scintillation detector with an optical fiber for fast neutrons. *Applied Radiation and Isotopes*, 69(2):539 – 544, 2011.  
 [6] *Applied Scintillation Technology: Lithium glass*. In physical properties.  
 [7] C. D. Bae et al. Characterization of a 6-Li loaded liquid organic scintillator for fast neutron spectrometry and thermal neutron detection. *arXiv:1206.4036*, 2012.  
 [8] R. J. Hu et al. Characteristics of boron-loaded plastic scintillators for neutron measurements. *Journal of the Korean Physical Society*, 50(1):1482 – 1488, 2007.  
 [9] K. Watanabe et al. Neutron-gamma discrimination in a <sup>6</sup>Li-GdAlF<sub>6</sub> scintillator based on pulse shape discrimination using digital signal processing. *NSS/MC, 2011 IEEE*, pages 436 – 439, 2011.  
 [10] Noriko Kawaguchi et al. Thermal neutron imaging with rare-earth-doped GdAlF<sub>6</sub> scintillators and a solid 252Cf source. *NIM A*, 65(1):351 – 354, 2011.  
 [11] H. Yang et al. Evaluation of a <sup>6</sup>Li(n,α) reaction detector with coincident double photodiode readout. *NIM A*, 65(1):344 – 369, 2011.

## LiF/ZnS(Ag)



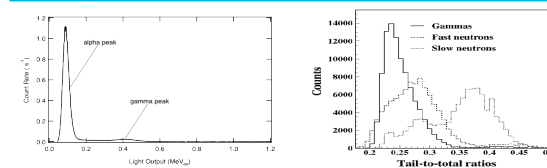
This established technique does fulfil requirements for a good  $\gamma$  discrimination by both PSD and Pulse Height Discrimination. On the other side, the opaqueness of the material and its count rate, restricted by a long decay constant ( $\tau \sim 1500 \text{ ns}$ ), are known shortcomings of the scintillator. [5, 3]

## Li Glass



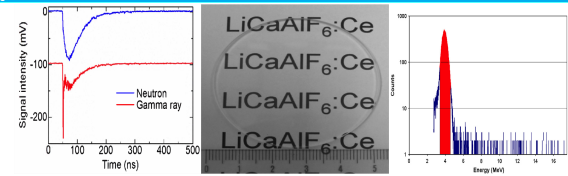
GS20 is used at the moment e.g. by the Spallation Neutrons and Pressure Diffractometer (SNPS) at SNS. The scintillator features a high count rate ( $\tau \sim 75 \text{ ns}$ ) and is transparent. However, the high  $\gamma$  sensitivity of the scintillator is limiting the scintillator thickness to a few mm. [6]

## Doped Organic Scintillators



Thermal neutrons are below the energy threshold to be detected in organic scintillators. However, nuclear reactions on B, Gd or Li are producing high energetic secondary particles, above the detection threshold. Nonetheless, it has to be shown that doped organic liquids or plastics can overcome their high  $\gamma$  sensitivity and large quenching for  $\alpha$  particles. [7, 8]

## Rejected Scintillators



We decided that we will not research some interesting scintillators for different reasons. Rare earth loaded scintillators like LiCaAlF<sub>6</sub>(Ce) are still too expensive to replace large scale detectors. Borated liquid scintillators were rejected due to safety concerns. Further, we decided against the use of hygroscopic crystals like LiI in the first test phase. [9, 10, 11]



Poster II





## Characterisation of a Liquid Scintillator Detector

J. Scherzinger<sup>a,b</sup>, K. Fissum<sup>b,c</sup>, R. Hall-Wilton<sup>a</sup>, E. Håkansson<sup>b</sup>, K. Kanaki<sup>a</sup>, M. Lundin<sup>c</sup>, M. Meshkian<sup>b</sup> and B. Nilsson<sup>a,c</sup>

a) Detector Group, European Spallation Source ESS AB, Lund, Sweden

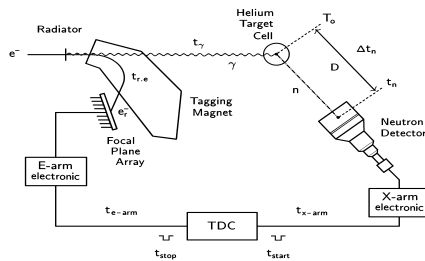
b) Division of Nuclear Physics, Lund University, Lund, Sweden

c) MAX IV Laboratory, Lund, Sweden

### Introduction

Liquid scintillator is considered by many to be the "gold standard" for the detection of neutrons in the tens of MeV range. With an eye on benchmarking the behaviour of liquid scintillator in an energy range less than a few MeV, we initiated a program of systematic calibrations by testing the time-resolution and pulse-shape discrimination capabilities of NE-213A in its normal energy regime.

### Photon Tagging



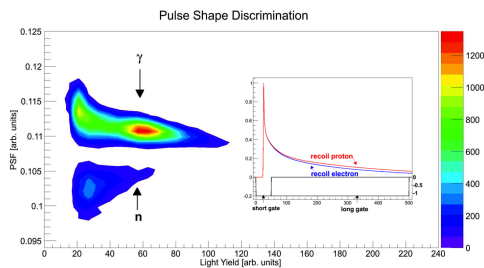
A 200 MeV electron beam was used to create 145-165 MeV bremsstrahlung photons which were then tagged with an energy resolution of 300 keV.

### Detector

A liquid scintillator cell coupled to an ET 9821KB tube via a borosilicate glass window and a lightguide detected particles at 90° to the photon beam.



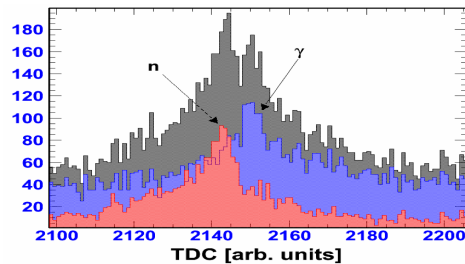
### Pulse-Shape Discrimination



Pulse-shape discrimination was used to distinguish between photons and neutrons. Excellent separation between the two particle species was obtained.

### Focal Plane TDC

The  $\gamma$  flash and the tagged photon neutrons were clearly separated by examining the coincidences between the focal plane and the detector cell.



### Conclusion

Clear signals from neutrons and photons originating from the target were easily observed. Future tests will include investigations at energies of a few MeV using Am/Be and Cf-252 sources and an extension of our efforts to lower and lower neutron energies with the goal of characterising sensitivity in the thermal energy range.



Poster III





# Characterization of a Liquid Scintillator Detector with an Americium-Beryllium Source

J. Scherzinger<sup>a,b</sup>, K. Fissum<sup>a,c</sup>, R. Hall-Wilton<sup>b</sup>, E. Håkansson<sup>a</sup>, K. Kanaki<sup>b</sup>, M. Lundin<sup>c</sup> and B. Nilsson<sup>b,c</sup>

a) Division of Nuclear Physics, Lund University, Lund, Sweden  
 b) Detector Group, European Spallation Source ESS AB, Lund, Sweden  
 c) MAX IV Laboratory, Lund, Sweden

## Introduction

The new Source Facility at the DNPLU - MAX IV - ESS Three-Party Detector Lab was recently inaugurated with a series of test measurements using an AmBe source to benchmark NE-213A scintillator.

## Americium Beryllium Source

**Neutron spectra**

**Gamma spectra**

Source  
YAP  
Bubble Dosimeter

$$^{241}\text{Am} \rightarrow \alpha + ^{237}\text{Np} + 5.63 \text{ MeV}$$

$$\begin{cases} \rightarrow ^9\text{Be}(\alpha, n)^{12}\text{C} \\ \rightarrow ^9\text{Be}(\alpha, n)^{12}\text{C}^* \end{cases}$$

$$\downarrow$$

$$\gamma (4.44 \text{ MeV})$$

## Time-of-Flight

TOF

counts

ToF [ns]

YAP

AmBe Source

Liquid Scintillator Cell

Stop

Start

TDC

$\gamma n$  coincidence  $\rightarrow$  TOF  
 $n\gamma$  coincidence  $\rightarrow$   $\gamma$  flash

## Pulse-Shape Discrimination

$$PS = \frac{QDC_{\text{long}} - QDC_{\text{short}}}{QDC_{\text{long}}}$$

PS [arb. units]

ToF [ns]

neutrons

$\gamma$

recoil proton

recoil electron

$$FOM = \frac{\Delta m}{\delta_1 + \delta_2}$$

Integrated PS

Threshold 0.58 MeV<sub>ee</sub>

counts

PS [arb. units]

FOM = 1.03

$\Delta m$

FWHM  $\delta_1$

FWHM  $\delta_2$

## Conclusion

Clear discrimination between neutrons and photons originating from the source was easily obtained. Future tests of new scintillator materials await.



Poster IV





